DESIGN OF FLUORIDE-ION BATTERIES BASED ON ELECTRON-ANION EXCHANGE

Connor Clarke Slamowitz

A dissertation submitted to the faculty at the University of North Carolina at Chapel Hill in partial fulfillment of the requirements for the degree of Doctor of Philosophy in the Department of Applied Physical Sciences.

Chapel Hill
2025

Approved by:

Jinsong Huang

James F. Cahoon

Shubin Liu

Wei You

Scott C. Warren

© 2025
Connor Clarke Slamowitz
ALL RIGHTS RESERVED

ABSTRACT

Connor C. Slamowitz: Design of fluoride-ion batteries based on electron-anion exchange
(Under the direction of Scott C. Warren)

The large-scale adoption of wind and solar power calls for battery technologies that achieve higher storage capacities at lower cost. Although lithium-ion batteries have been widely adopted, other ions, including Na^+, Zn^{2+}, Mg^{2+}, Al^{3+}, and Cl^- continue to provoke scientific interest because of competitive theoretical capacities, lower costs, and resource abundance. Among these alternatives is F^-, which has favorable characteristics because of its small charge density and light weight. Fluoride-ion batteries (FIBs) have been relatively unexplored, however, because electrolytes that are highly conductive at room temperature were only recently discovered. With this discovery, there is now an increased motivation for systematically exploring electrodes for the FIB. These advances in electrolytes and electrodes have led to our development of a new class of electrodes that reversibly intercalate fluoride ions: electrides.

Electrides are ionic crystals that have lattice sites occupied by a bare electron, often called an "anionic electron" because the site has a negative charge. Some electrides crystallize in a layered structure and in these materials, the electrons lie in planes, sandwiched between layers of cations. Employing layered electrides in fluoride-ion batteries capitalizes on the transport characteristics of layered materials and the high electrochemical potential of the anionic electrons. In addition, layered electrides allow us to probe a fundamentally new mechanism for electron transfer: one in which an anionic electron is exchanged directly for a fluoride without reduction or oxidation of the host atoms. The realization of this exciting mechanism leads to electrodes with large capacities and little volume change upon intercalation. We have introduced the name "electrochemical electron-anion exchange" (EAX) to describe this new mechanism.

In this dissertation, we describe how the electride, Y_2C, led to the prediction of the EAX mechanism in the Y_2C–Y_2CF_2 material system. We highlight our calculations and experiments that provide the first evidence for electron transfer without reduction or oxidation during the electrochemical fluorination of Y_2C at room temperature. To further improve cycling performance, we design 1) aliovalently doped Y_2CF_2 to improve the ionic conductivity of our electrode, 2) artificial solid-electrolyte interphases to improve the

chemical stability of Y_2C at its surface, and 3) high surface area amorphous electrodes that enhance electrode composite interactions while driving fast fluoride diffusion. These design principles lead to large capacity electrodes that cycle repeatedly without reduction or oxidation.

The discovery of EAX and high-capacity electrodes is the beginning of a fascinating era in the development of the fluoride-ion battery. These advances, combined with the development of new fluoride electrolytes, are leading to exciting scientific and technological progress.

per aspera, ad astra

ACKNOWLEDGEMENTS

To my advisor, Professor Scott Warren, thank you for pushing me to the edges of my ability. You taught me the virtue of science – not only in its practice but in its effect on others. Your guidance will stay with me forever.

To Tyler, I wouldn't be at UNC without you. Your mentorship at Luna made me realize that I wanted to be a scientist; that I wanted to solve problems in materials science for real and lasting impacts. You've continued to guide me throughout graduate school. I am happy to have your mentorship and to have you as a friend.

To my colleagues and friends, especially Don, Hye Sol, and Sam, thank you for making this journey fun and exciting. I want to especially thank my lab mates for the thoughtful conversations, the coffee and lunch breaks, and all the laughs along the way.

To Jacob, Matt, Madeline and Lauren – your personal, academic, and professional mentorship acted as a beacon that I could strive for. I can always rely on instantly getting texts back from you when I have questions or concerns. Your support pushed me through my first years at UNC.

To Becca, Duncan, and Karen – thank you for being the best cohort I could ask for. I'm proud to grow as a scientist alongside you all.

To Miguel and Jackson – thank you for being excellent mentees. Your passion for science gave me a passion for mentorship. I am so happy to see the two of you move onto profound futures. Never stop being inquisitive!

For my friends in the graduate student volleyball club – you made the evenings and weekends something to truly look forward to. You put the "life" in work-life balance.

To everyone in APS – the department is a special place. There is no department on campus with such warm faculty, staff, and students. I have grown to think of us as a family and I will do all that I can to give back when I am gone.

To my Mother and Father, you both worked so hard so that I can be where I am today. You've supported me in everything that I do, and I cannot be more thankful for that. You both pushed me to go

outside of my comfort zone, to push beyond my limits. Without your advice, love and guidance, I would surely not be where I am today. I appreciate having a warm blanket and a hot meal whenever I come home.

To my sister, Tristen, you are my north star. You have always been my role model and my best friend. You have been someone I can talk to at the drop of a hat, who has my back and somehow has the sagest advice. You truly make me proud to be a Slamowitz and I'm so excited to climb the next mountain – both physically and metaphorically – with you.

To Jessica, my future wife… you have been by my side for this entire journey. You have challenged my preconceptions of what it means to be a good human and scientist. Through hours of practice presentations, manuscript drafts, and everything in between, you've been there for me when I needed you most. I truly do not believe I could have done this without you (and Grady, Sadie and Kitty, of course). I am so excited to share my life with you in the future. In some ways it's the end of a special time for us, but there is going to be nothing like our future.

TABLE OF CONTENTS

ABSTRACT ii

ACKNOWLEDGEMENTS v

LIST OF FIGURES xii

LIST OF TABLES xix

LIST OF ABBREVIATIONS AND SYMBOLS xx

CHAPTER 1: INTRODUCTION 1

1.1 Motivation 1

1.2 Electrides: From 2D Material to Intercalation Electrode 3

1.3 Electrides as Fluoride-Ion Battery Electrodes 5

1.4 Fluoride Shuttle Electrolytes 7

1.4.1 Solid Fluoride Shuttle Electrolytes 7

1.4.2 Liquid Fluoride Shuttle Electrolytes 8

1.5 Overcoming Challenges in Battery Devices 10

1.5.1 Electrolyte Degradation 10

1.5.2 SEI Formation 13

1.6 Overview of the research described in this thesis 15

REFERENCES 17

CHAPTER 2: METHODS 21

2.1 Introduction 21

2.2 Computational Methods 21

2.2.1 High Throughput DFT Modeling 21

2.2.2 Processing and Modeling XANES Data 23

2.2.3 Extended X-ray Absorption Fine Structure 25

2.3 Synthesis Methods 29

2.3.1 Synthesis of Y_2C 30

2.3.2 Synthesis and Y_2CF_2 30

2.3.3 Synthesis of Np1F Electrolyte Salt 31

2.3.4 Fabrication of Liquid State Electrochemical Cells 32
2.3.5 Fabrication of Solid-State Electrochemical Cells 35
2.3.6 Synthesis of Amorphous Y_2CF_2 35
2.3.7 Synthesis of metal doped Y_2CF_2 36
2.3.8 Synthesis of Sulfur Coating on Electrides 38
2.4.1 X-ray Diffraction 40
2.4.2 X-ray Absorption Spectroscopy 42
REFERENCES 45
CHAPTER 3: ELECTRON-ANION EXCHANGE: EXPERIMENTAL DEMONSTRATION OF A NOVEL INTERCALATION MECHANISM 49
3.1 Introduction 49
3.2 Methods 51
3.2.1 XAS 51
3.2.2 Modeling XANES Spectra using the Bethe-Salpeter Equation 51
3.2.3 Charge Partitioning of the Electron Localization Function 52
3.3. Results and Discussion 53
3.4 Conclusion 57
REFERENCES 58
CHAPTER 4: HIGH-THROUGHPUT DISCOVERY OF ELECTRIDE DOPANTS 62
4.1 Introduction 62
4.2 Methods 63
4.2.1 High Throughput DFT Studies 63
4.2.2 DFT of Doped Electrides 64
4.2.3 Synthesis of Calcium Doped Y_2CF_2 64
4.3 Results and Discussion 65
4.3.1 High Throughput Discovery of Stable Dopants 65
4.3.2 Doping Effects on Electride Characteristics 68
4.3.3 Synthesis of Doped Y_2CF_2 71
4.4 Conclusion 72

REFERENCES 73

CHAPTER 5: EXPLORATION OF ELECTROCHEMICAL (DE)INSERTION OF FLUORIDE IN THE Y_2C ELECTRIDE 75

5.1 Introduction 75

5.2 Methods 76

5.2.1 Density Functional Theory 76

5.2.2 Cluster Expansion Modeling 76

5.2.3 Monte Carlo Simulations 77

5.2.4 Electrochemical Set-up 77

5.2.5 Structure Analysis 78

5.3 Results and discussion 79

5.3.1 Computational Exploration of Fluorinated Phases 79

5.3.2 Electrochemical fluorination of Y_2C Electrodes 83

5.4 Conclusions 85

REFERENCES 86

CHAPTER 6: STRUCTURAL CHARACTERISTIZATION OF SURFACE ENGINEERED AIR STABLE Y_2C ELECTRIDE 89

6.1 Introduction 89

6.2 Methods 90

6.2.1 Synthesis of Y_2C 90

6.2.2 Synthesis of Sulfur Coated Y_2C 90

6.2.3 X-ray diffraction 90

6.2.4 Transmission Electron Microscopy 91

6.2.5 Chemical Fluorination 91

6.3 Results and Discussion 91

6.3.1 Structural Characterization of Surface Coating 91

6.3.2 Stability in Air 94

6.3.3 Fluorination Dynamics 95

6.4 Conclusion 97

REFERENCES 98

CHAPTER 7: AMORPHOUS METAL SUBCARBIDE FLUORIDE FOR HIGH-PERFORMANCE FLUORIDE-ION BATTERIES 100

7.1 Introduction 100

7.2 Methods 101

7.2.1 Synthesis of Y_2C 101

7.2.2 Fabrication of Electrodes 101

7.2.3 Electrochemical (de)fluorination 102

7.2.4 Chemical Fluorination Reactions 102

7.2.5 Transmission Electron Microscopy and X-ray Diffraction 103

7.2.6 Computational Analysis 103

7.3 Results and Discussion 104

7.3.1 Stable Cycling of Amorphous Electrodes 104

7.3.2 Identification of the Amorphous Phase in a Y_2C/Y_2CF_2 Electrochemical Cell 105

7.3.3 Structural characterization of the amorphous fluorinated phase 107

7.3.4 Electronic Structure Characterization of Amorphous Fluorinated Phase 111

7.3.5 Analysis of the Expanded/Amorphous Y_2C 114

7.4 Conclusions 115

REFERENCES 116

APPENDIX: SUPPORTING INFORMATION FOR CHAPTER 4 119

APPENDIX: SUPPORTING INFORMATION FOR CHAPTER 5 120

APPENDIX: SUPPORTING INFORMATION FOR CHAPTER 6 122

A6.1 TMA Coating vs Sulfur Coating Solution based deposition 122

A6.2 Cubic vs Layered Sulfur Coating Dynamics 122

A6.3 Exposure to Oxygen for 1 week 123

APPENDIX: SUPPORTING INFORMATION FOR CHAPTER 7 125

A7.1 Electrochemical and Physical Characterization 125

A7.2 Atom Quantification with TEM-EDS 125

A7.3 XPS Standards 125

A7.4 Amorphization Mechanism 127
A7.1.1Thermodynamic Model of Amorphous Transition 129
A7.5 Coordination Environment of structure optimized aY_2CF_2 131

LIST OF FIGURES

Figure 1 - 1: Comparative energy density of varying ion-intercalation type batteries based on theoretical gravimetric and volumetric capacities. 2

Figure 1 - 2: Theoretical fluoride-ion battery based on a metal-fluoride cathode and Y_2C electride anode. 2

Figure 1 - 3 [35]: Visualization of complex stability window of electrolytes in the oxidizing (at the cathode) and reducing (at the anode) regimes. Solvation and concentration play into the overall stability of the electrolyte, while evolving electrochemical environments contribute to charge transfer mechanics. 11

Figure 1 - 4 [36]: Energy schema for the sacrificial reduction of electrolyte additive ethylene carbonate to form surface stabilizing products. These products form an interphase on the surface of lithium-ion battery electrodes to reduce electrode expansion, cracking, defects, and dissolution. 12

Figure 1 - 5 [6]: (Left)Solvation structure of the fluoride anion in Np_1F/BTFE solution. Fluoride is stabilized, reducing its ability to form HF/HF_2^-. (Right) Electrochemical stability window of high-performance fluoride containing electrolyte blend. 13

Figure 1 - 6 [6]: LaF_3 artificially engineered SEI reduces the dissolution of metal into the electrolyte, stabilizing the cycle lifetime of battery electrodes in the presence of Np_1F/BTFE electrolyte. 15

Figure 2 - 1: (Top) script used to generate the primitive from the CONTCAR structure file output from a VASP geometry optimization. (Bottom) Script used to generate the cubic supercell using functions in PyMatGen. 22

Figure 2 - 2: (Left) Input variables to determine pre-edge and post-edge features for (right) background subtraction in Larch XAS Viewer. Example processing is from Ti_2C EXAFS Data. 27

Figure 2 - 3: (Left) Input variables to determine normalization and background subtraction to convert to an accurate modeling of the (right, top) EXAFS spectrum as a function of photoelectron momentum and the (right, bottom) Fourier transform of the function to get the real-space representation of coordination in Larch XAS Viewer. Example processing is from Ti_2C EXAFS Data. 28

Figure 2 - 4: Final output from FEFF8 fit of the Ti_2C Fd3m structure model, fit to the experimental EXAFS data collected at CHESS..... 29
Figure 2 - 5: Custom electrochemical cell milled from a block of Teflon. In this case, the counter electrode is made from a 15mm Pt disk, and the working electrode is made from Y_2C/C/PVDF cast on a Ta foil disk. 34
Figure 2 - 6: Stainless steel reaction vessel used to deposit vaporous sulfur on the surface of Y_2C. The glass container is a centrifuge tube cut to fit into the stainless steel Swagelok reactor. 40

Figure 3 - 1: (a) Concept of electron−anion exchange. The battery configuration incorporates $[Y_2C]^{2+}(2e^-)$ as an anode, an F^- electrolyte, and a cathode (e.g., a metal fluoride).The reversible conversion of (b) Y_2CF_2 to (c) $[Y_2C]^{2+}(2e^-)$ under an applied bias where yellow, orange, and red show isosurfaces of the anionic electrons at the Fermi level. 50
Figure 3 - 2: Electron density isosurfaces near the Fermi level. (A) The ground state of Y_2CF_2 with one F vacancy showing a F^- (purple) and an anionic electron(orange) at tetrahedral sites prior to exchange. (B) Transition state during electron−anion exchange. (C) Ground state after the exchange. The corresponding oxidation states of four involved yttrium atoms during each transition step are shown..... 54
Figure 3 - 3: (A) X-ray photoemission spectra from Y_2CF_2 stored in a glovebox for the yttrium 3d core electron binding energies (B) XANES of Kα fluorescence for Y_2C, Y_2CF_2 and chemically defluorinated Y_2CF_2. 55
Figure 3 - 4: Electronic structure characterization of using A) K-Edge Synchrotron X-Ray Absorption Spectroscopy, subsequently modeled by the Bethe-Salpeter Equation as part of the EXCITING Density Functional Theory Package. B) Using Bader partitioning of the electron-localization function (BadELF), the charge density was integrated around both nuclear and non-nuclear electron attractors to find C) oxidation states of atomic species in Y_2C and Y_2CF_2 57

Figure 4 - 1: Schematic of dopant structure and metals used in high throughput doping calculations. Supercells were created such that coulombic interactions were negligible between vacancy sites, with 90

atoms in M-Y_2CF_2, 89 in M-Y_2CF_2 - 1x, and 88 in M-Y_2CF_2 - 2x. 54 atoms were used in the M-Y_2C structures..... 65
Figure 4 - 2: Measurement of the displacement in the z-direction of inserted ions during the geometry optimization of doped structures. The atoms drifted either towards the fluoride/electride layer, resulting in a positive drift, while a negative drift corresponds to drift towards the carbide layer. We set arbitrary drift magnitude limits of 0.3 Å by qualitatively analyzing relaxed structures..... 66
Figure 4 - 3: DFT calculations resulting in the enthalpy of formation (eV/vac) for structures with fluoride near the dopant site and a vacancy near the dopant site. A negative ΔE is ideal as it represents favorable formation energy for materials with vacancies that localize at the dopant site. However, the near-vacancy structure should not be too stable, as it would significantly increase the activation energy for vacancy hopping..... 67
Figure 4 - 4: Enthalpy of formation for metal doped Y_2C (yellow), metal doped Y_2CF_2 (blue), metal doped Y_2CF_2 with 1 vacancy site (orange), and metal doped Y_2CF_2 with 2 vacancy sites (grey)..... 68
Figure 4 - 5: Charge density difference plots through an electride layer. Lower values (blue) correspond to regions where charge density is lower relative to the undoped Y_2C..... 69
Figure 4 - 6: Charge density and ELF difference plots through a fluoride layer with a single vacancy. Lower values (blue) correspond to regions where the charge density or ELF is lower relative to the undoped Y_2C..... 70
Figure 4 - 7: XRD of $Y_{2-x}Ca_xCF_{2-x}$, where x represents the moles of Calcium stoichiometrically added to the synthesis. The % doped represents the % of yttrium sites occupied by calcium. As the percentage of calcium increases past 9%, the formation of parasitic phases begin to grow, represented by blue asterisks..... 71

Figure 5 - 1: Preparation of the Y_2C intercalation electrochemical testing cell. a) Calculated vs synthesized spectra showing phase-pure Layered Y_2C, b) ball milled Y_2C particles, c) fabricated 15mm diameter electrode consisting of 80%wt Y_2C, 10%wt Super P, and 10% PVDF binder, and d) Full cube cell assembly..... 78

Figure 5 - 2: a) The convex hull for fluorine intercalation in Y_2C considering the O3, T1, and H1-3 phases with the formation energies given in meV/formula unit. The energies are calculated by canonical Monte Carlo simulations at 0K using ECIs from cluster expansion fitting. b) The predicted voltage profile for fluorine intercalation in Y_2C. The voltage is derived from chemical potential calculated with semi-grand canonical Monte Carlo simulations at 298K. 79

Figure 5 - 3: a) Potential diagram a F- battery with a Y_2CF_2 anode, a Np1F/BTFE liquid electrolyte, and intercalation-type cathodes (e.g. $La_2CoO_4F_2$ and $Mg_{0.5}F_{0.5}Sb_2O_4F$). The potentials for the cathodes are taken from reported DFT calculations[21]. b) Comparison of the gravimetric and volumetric capacities of the electrodes in this work and previously studied intercalation-type electrodes. 82

Figure 5 - 4: Experimental and computational demonstration of layered-Y_2C charging. A) Cluster expansion calculation showing the phase change from layered-Y_2C (AB stacked) to Y_2CF_2 (AA Stacked) at 25% charge. B) Experimental charging curve during a chronopotentiometry experiment, showing 3 distinct regions highlighted with a red star, blue star, and green star. C) XRD patterns at the associated stars, highlighting a single phase change from Y_2C to Y_2CF_2. 84

Figure 6 - 1: XRD of the synthesized S@Y_2C material. As evidence from comparing as made Y_2C and S@Y_2C synthesized at 350^{o}C, no new phases appear. However, as the temperature increases to 550^{o}C for 24hr, we see the growth of peaks associated with Y_2S_3. 92

Figure 6 - 2: Energy Dispersive Spectroscopy mapping of Transmission Electron Microscopy images for sulfur coated Y_2C reacted at 150^{o}C for 24hrs (a) and 350^{o}C for 24hrs (b). Yellow indicates spectroscopic identification of sulfur, blue indicates spectroscopic identification of yttrium. We performed a depth analysis of the EDS signal (c) to show the exceptional core shell morphology of the sulfur-coated Y_2C particles. The stoichiometry of the sulfur to yttrium is ~2 parts yttrium to ~3 parts sulfur at the shell, decreasing in the particle, and increasing again. 93

Figure 6 - 3: Time-resolved XRD of Pure Y_2C (top) and sulfur coated Y_2C (S@Y_2C, bottom). For Y_2C (top), we observed the growth of graphite peaks at 27 2θ as the 00l planes (29.7 2θ & 49.7 2θ) begin to disorder as oxygen diffuses into the interlayer spacing of Y_2C. We also observe polycrystalline/amorphous Y_2O_3 phase begin to grow after 20 minutes at ~32.0 2θ. 95

Figure 6 - 4: a) Structural characterization of as-made Y_2C, S@Y_2C and S@Y_2C fluorinated with gaseous XeF_2 using XRD result in no structural modification of the material. However, b) EDS mapping of samples collected in TEM reveals significant fluorine. Using c) depth profiling, we show that the fluoride is trapped in the amorphous sulfur-yttrium shell, creating a new amorphous Y-S-F passivating shell. 96

Figure 7 - 1: A) Cycling behavior of ball milled Y_2C electrodes reveals good cyclability at a theoretical capacity of 282 mAh/g for at least 10 cycles before overpotentials begin to build in the electrochemical cell. B) Discharge capacity and charge capacity show that the theoretical capacity was reached for both cycles for 10 cycles. After 10 cycles, an 89% charge capacity was maintained, whereas a 100% discharge capacity was maintained. After 31 cycles, the capacity quickly decreased to 27% and was maintained until cycling was ended. 104

Figure 7 - 2: Behavior of the ball milled $Y_2C/Cu/Ca_{0.5}Ba_{0.5}F_2$ composite upon the first discharge/charge cycle. The first discharge achieves a reversible gravimetric capacity of 282 mAh/g. A) The pristine composite after ball milling shows distinct peaks for Cu, whereas the phases identified as YC and $Ca_{0.5}Ba_{0.5}F_2$ show decreased intensity and peak broadening. B) XRD after the discharge cycle to Y_2CF_2 provides evidence of an amorphous phase with no long-range ordering. C) Upon recharge, the Y_2C peaks shift to lower 2-theta angles, revealing an expanded electride. 107

Figure 7 - 3: TEM–EDS mapping of the amorphous Y_2CF_2 material prepared via chemical fluorination with XeF_2, revealing A) Yttrium and B) fluorine signals at equal atomic concentrations. C) Electron diffraction image revealing diffuse rings with a noncrystalline morphology. D) The Fourier transform across the radial intensity map provides the electron pair distribution function (ePDF). The ePDF shows approximate coordination shells of 2.41 Å and 4.02 Å, corresponding to the approximate bonding of Y-F or Y-C and Y-Y, respectively. Bonding signals less than 1.91 Å are attributed to the signal of the lacey carbon grid used as the sample holder. 108

Figure 7 - 4: A) Using the experimental ePDF, we simulated the structure of amorphous Y_2CF_2 using Hybrid Reverse Monte Carlo. Using the simulated structure, a direct comparison of the coordination environment for B) crystalline Y_2CF_2 and C) amorphous Y_2CF_2 can be constructed. The fit reveals a D) general layered structure with E) expanded fluoride pathways bridged across the cationic framework. . 111

Figure 7 - 5: Background subtracted XPS measurements of a) $R3m$ Y_2C carbon 1s binding energy, b) $R3m$ Y_2C yttrium 3d binding energy, c) $P3m1$ Y_2CF_2 [5] carbon 1s binding energy, d) $P3m1$ Y_2CF_2 [5] yttrium 3d binding energy, c) aY_2CF_2 carbon 1s binding energy, and d) aY_2CF_2 yttrium 3d binding energy. 112

Figure A4 - 1: Decomposition of Sr-doped Y_2CF_2 into parisite as Sr composition increased. Asterisks reveal the decomposition product. 119

Figure A5 - 1: Crystal structures of the T1, O3, and H1-3 phases considered in our cluster expansion.. 120

Figure A5 - 2: (Top) Open circuit potential of Y_2C composite electrodes submerged in Np1F/BTFE electroltye. (Bottom) Corresponding XRD of structure decomposition observed after contact with Np1F/BTFE. 121

Figure A6 - 1: XPS of Y_2C cleaved in a TMA:Toluene solution. A) Y 3d signal revealing Y^{3+} oxidation states (159eV) after Ar+ sputtering experiments and B) C 1s signal revealing adventicious carbon states (~285eV) after Ar+ sputtering experiments 122

Figure A6 - 2: XPS of Y_2C cleaved in a Sulfur:Toluene solution. A) Y 3d signal revealing Y^{3+} (157.0 eV) and Y^{2+} oxidation states (154.6 eV) on the as-made cleaved surface and B) C 1s signal revealing adventicious carbon (284.6 eV) and carbide (279.6 eV) states after Ar+ sputtering experiments 122

Figure A6 - 3: A) TEM-EDS mapping of a sulfur coated cubic-Y_2C particle synthesized at 350 ^oC for 6 hours, revealing no formation of core-shell morphology compared to B) TEM-EDS mapping of sulfur coated layered-Y_2C particle synthesized at 350 ^oC for 6 hours, revealing formation of core-shell morphology. 123

Figure A6 - 4: A) Y_2C powder exposed to air for 6 days and B) corresponding XRD revealing amorphization. C) S@Y_2C powder exposed to air for 6 days and D) corresponding XRD revealing no degradation of the electride crystal. 124

Figure A7 - 1: First discharge (green) and discharge/charge (blue) cycle of Y_2C/Cu/CBF composite. 125

Figure A7 - 2: YF_3 measured with XPS reveals formation of YF_3 across each amorphous Y_2CF_2 sample on its surface. A) YF_3 standard directly compared to aY_2CF_2 as made sample. B) aY_2CF_2 etched with Ar+

directly compared to aY_2CF_2 reveals significant change in intensity of YF_3, revealing the impurity is confined to the sample's surface. 126
Figure A7 - 3: Amorphous Y_2CF_2 exposed to oxygen. As the peak, assigned to an oxidized carbide species at 282 eV, does not increase in intensity, the peak can be assigned to a C-F bond rather than a C-O bond. 127
Figure A7 - 4: XRDs of Y_2C composite as ball mill time increase. As time increases, peak intensity decrease and broaden as particle size decreases. 128
Figure A7 - 5: XRDs of Y_2C electrode composite chemically fluorinated with XeF_2 with Cu nanoparticle electron conducting additive (red) and without Cu nanoparticles (yellow). 129
Figure A7 - 6: Qualitative model of the effect of ion insertion on structural energy. This model shows that as ions insert into Y_2C particles with small radii, high defect concentrations could drive the phase transition into an amorphous structure. 130
Figure A7 - 7: Coordination analysis of crystalline (blue) vs amorphous (orange) Y_2CF_2 structure, fabricated using hybrid reverse Monte Carlo simulations. Significant deviation from the crystalline bonding environment indicate a structural reorganization in experimental synthesized amorphous material 131

LIST OF TABLES

Table 1 - 1: Comparisons of charge density revealing fluoride having the lowest charge density of 1.00. "q" describes the charge of the atom while r represents the ionic radius. 7

Table 1 - 2 [6]: Transition metal dissolution measured via ICP-MS in the presence of fluoride containing electrolyte solutions, specifically Np_1F/BTFE. 13

Table 2 - 1: Function for calculating the ideal ratio of atoms to produce materials with a goal doping percentage. Doping percentage is the percentage of yttrium sites occupied by a dopant. 37

Table 2 - 2: (Left) Function for determining the moles of elements per molecular formula. This is used to calculate the total moles of precursor needed to produce the goal doping percentage (right) 38

Table 2 - 3: Function for converting the moles of precursors to the mass percentage of precursor for synthesis. 38

Table A7 - 1: Average Values across amorphous Y_2CF_2 particles obtained via TEM-EDS 125

LIST OF ABBREVIATIONS AND SYMBOLS

2D	two-dimensional
2DEG	two-dimensional electron gas
3D	three-dimensional
ACET	anion-coupled electron transfer
BadELF	Bader electron localization function
BSE	Bethe-Salpeter equation
CE	counter electrode
CHEXS/CHESS	Cornell high energy synchrotron/x-ray source
CLEASE	cluster expansion in atomic simulation environment
C-rate	charging rate
DFT	density functional theory
EAX	electride-anion exchange
ECI	effective cluster interaction
EDS	energy dispersive x-ray spectroscopy
ELF	electron localization function
ePDF	electron pair distribution function
EXAFS	x-ray absorption fine structure
FFT	fast Fourier transform
FIB	fluoride-ion battery
FWHM	full width at half maximum
GGA	generalized gradient approximation
HERFD	high energy resolution fluorescence detected
HOMO	highest occupied molecular orbital
HRMC	hybric reverse Monte Carlo
HRTEM	high-resolution transmission electron microscopy

LIB	lithium-ion battery
LOOCV	leave-one-out cross validation
LUMO	lowest unoccupied molecular orbital
MC	Monte Carlo
MSE	mean square error
NEB	nudged elastic band
PAW	Projector-augmented wave
PBE	Perdew–Burke-Ernzerhof
PXRD	powder x-ray diffraction
PyMatGen	Python Package for Material Genomics
RE	reference electrode
SEI	solid-electrolyte interphase
SEM	scanning electron microscopy
Simmate	The Simulated Materials Ecosystem
STEM	scanning tunneling electron microscopy
TEM	transmission electron microscopy
TIG	tungsten inert gas
VASP	Vienna *ab initio* software package
vdW	van der Waals
WE	working electrode
XANES	x-ray absorption near edge structure
XAS	x-ray absorption spectroscopy
XC	exchange-correlation
XPS	x-ray photoelectron spectroscopy
XRD	x-ray diffraction

CHAPTER 1: INTRODUCTION

Connor C. Slamowitz, Jack D. Sundberg, Scott C. Warren

1.1 Motivation

Nearly two centuries[1] of steady improvements in secondary battery technology has led to the pervasive use of portable electronic devices, electric vehicles, and grid storage sourced from renewables. At the spearhead of this revolution lies the lithium-ion battery (LIB). The LIB improved electrochemical energy storage through the reversible intercalation of lithium cations from the electrolyte into the electrode. This opened the door for electrochemical cells with a large energy density, moderate cyclability, and, in combination with nonaqueous electrolytes, high voltage[2]. These advantages primed emerging industries for new electronic devices that rely on portable energy sources with long cycle life. Furthermore, as society transitions from fossil fuels to renewable energy, the need for rechargeable batteries is expected to increase.

Unfortunately, the exponential growth in lithium-ion batteries is unlikely to be sustainable because of material, environmental, and human costs[3]. Therefore, it is important to investigate materials that are relatively abundant but that can still meet the increasing demand for rechargeable batteries. A considerable research effort has focused on the use of alternative ions that can reversibly shuttle between electrodes. Among these alternatives is the fluoride anion. F^- (19 amu/e^-) provides similar mass-to-charge ratios as other common alternatives such as Na^+ (23 amu/e^-), Mg^{2+} (12 amu/e^-), Al^{3+} (9 amu/e^-), Cl^- (35 amu/e^-), or Zn^{2+} (33 amu/e^-) making it a promising candidate for use in high-capacity batteries.

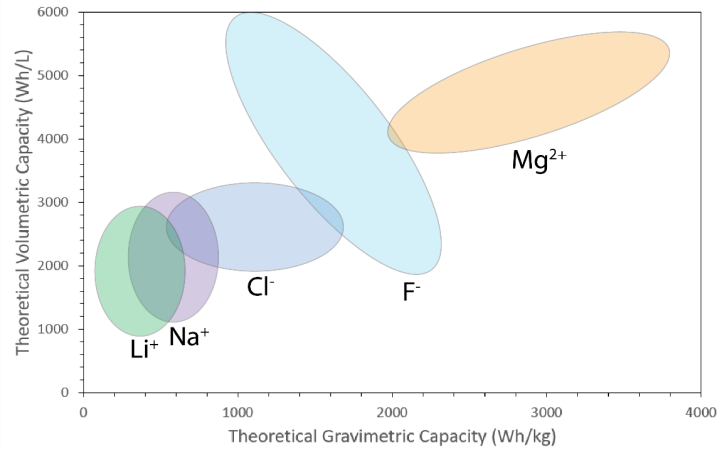


Figure 1 - 1: Comparative energy density of varying ion-intercalation type batteries based on theoretical gravimetric and volumetric capacities.

Until recently, FIBs were difficult to develop due to a lack of research into electrolytes that can conduct fluoride ions. In 2011, Reddy and Fichtner revitalized the FIB field by doping LaF_3 with barium, creating a solid-electrolyte that did not undergo phase transformations at their operating temperature of 150 °C[4]. This discovery paved the way for electrochemically reversible FIBs that utilize solid-state electrolytes[5]. Despite these advances, solid fluoride electrolytes still require expensive high-temperature pre-processing and are often limited by chemical incompatibilities and small voltage windows.

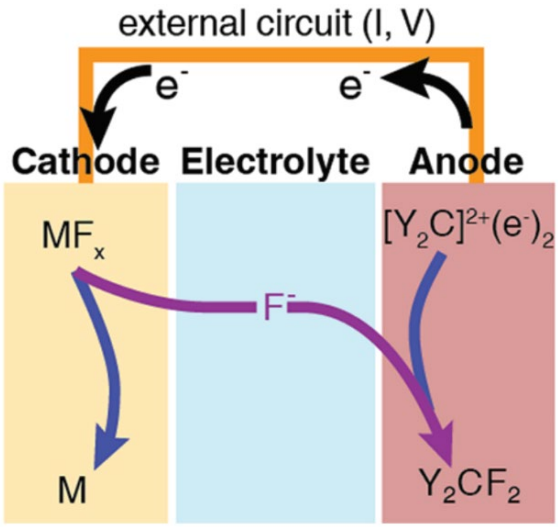


Figure 1 - 2: Theoretical fluoride-ion battery based on a metal-fluoride cathode and Y_2C electride anode.

Although the use of solid electrolytes enabled initial studies in electrochemical cells, their low fluoride-ion conductivity limited their use in room-temperature batteries. Recently, Davis et al. developed a liquid electrolyte that resolved many of the challenges with solid state electrolytes[6]. An electrolyte that operates at room-temperature can facilitate the use of FIBs in new portable electronic devices that operate in ambient conditions. Crucially, liquid electrolytes facilitate studies into many new electrode materials that would fail

to operate at elevated temperatures. Therefore, this introduction will describe prior contributions to the development of fluoride-ion battery electrodes, particularly those that leverage the new, fluoride-conductive liquid electrolyte.

The key contribution in prior works has been the discovery of layered electrides as a high-capacity electrode for FIBs. In electrides, lattice sites that would ordinarily hold an anion instead contain a bare electron; in layered electrides, these electron-containing sites lie in planes as a "2D sheet" of electrons. As an electrode in an FIB, it is described how the electride's electrons can be displaced by fluoride ions in the electrolyte through intercalation. Computational predictions show that the diffusion of fluoride is expected to occur at room-temperature under electrochemical control. Additionally, some of these layered electrides, such as Y_2C and Sc_2C, offer gravimetric and volumetric capacities that exceed those of state-of-the-art lithium-ion batteries, while at the same time undergoing almost no volume change. I discuss recent investigations into these materials, including the discovery of redox-less electron transfer, and outline my roadmap towards the realization of reversible electrochemical cells made with layered electrides that can store fluoride at a high-capacity.

1.2 Electrides: From 2D Material to Intercalation Electrode

First synthesized in the 1950s and 1960s, layered metal nitrides (M_2N; M=Ca, Sr, Ba) were proposed to have lone electrons occupying distinct lattice sites within the large interlayer gaps[7].This odd proposal leads to compositions such as $[Ca_2N]^+e^-$ which are chemically counter-intuitive relative to the competing idea that these were actually hydrides (M_2NH)[8]. But in the early 2000s, studies computationally confirmed that lone electrons are indeed thermodynamically stable[9], and later, experimentally demonstrated electron confinement in the interlayer spaces[10]. This validation of electrides extended to other systems such as metal carbides (M_2C; M=Y and other lanthanides), where these materials were collectively demonstrating novel anisotropic properties. For example, layered electrides were shown to possess particularly high electron mobilities, ultra-low work functions, and highly anisotropic optical responses in-plane of the 2D-confined, lone-electron layers[10, 11]. These intrinsic properties of layered electrides motivated the Warren Lab's investigation into areas where other layered materials have been applied. Specifically,

previous work sought to investigate whether this material could be (1) exfoliated as a 2D material, (2) assembled into heterostructures, and even (3) reversibly intercalated for battery applications.

The exfoliation of electrides raised new questions in the context of 2D materials because lone electrons in the interlayer are contrary to typical layered materials held together by van der Waals (vdW) forces. Surprisingly, Zhao et al. predicted that even a monolayer of Ca_2N is dynamically stable and still possess electride electrons on its surface[12], which motivated the Warren Lab's research towards the mechanical exfoliation of bulk Ca_2N. This work found that this material and many other layered electrides actually have low interlayer binding energies despite having ionic interactions present between electride electrons and the host lattice[13]. In fact, these binding energies are comparable to other 2D materials that had been previously exfoliated. This led to the experimental production of 2D Ca_2N while maintaining electride properties[14]. This "electrene" was stable under nitrogen and select solvents, and optical measurements further showed that the electride electrons were still present on the surface of the 2D sheet. The addition of electrenes to the large array of 2D materials represented a unique opportunity in the context of previous vdW-based 2D materials -- as now there is a material with highly reducing electrons exposed, which is hypothesized to functionalize or dope other materials.

Calculations showed that the stacking of electrenes with other 2D materials led to bond-like formation, where interlayer distances were 1 Å shorter than typical vdW heterostructures such as graphene-MoS_2 or WS_2-MoS_2[15]. This was caused by nearly full transfer of the electrene's surface electrons to the adjacent material -- specifically, Ca_2N and Sr_2N electride electron would fully transfer to graphene, phosphorene, h-BN, MoS_2, and ZrS_2. Thus, it was predicted that electride electrons can be utilized to lower work functions and even improve Li-ion working voltages when stacked with other materials. This also implies that these electrons can be transferred without any change to the oxidation states of the electride's host lattice. These conclusions laid the foundation for replacing the layer of anionic electrons within a bulk electride through the intercalation of small molecules and ions.

Previous to the Warren Lab's exploration, there had been several experimental and computational reports on lithium and sodium intercalation[16, 17] into electrides. However, the overall assessment was that intercalation of cations was not promising because this would require the implausible reduction of an electron-rich electride. Furthermore, the corresponding cation-intercalated materials were not known to be

thermodynamically stable, in contrast to their anion-intercalated analogs, such as Ca_2NCl[18]. This motivated current exploration of the exchange of the bare electron for an anion in a battery configuration.

1.3 Electrides as Fluoride-Ion Battery Electrodes

Although many layered electrides are thermodynamically stable upon halogenation, the choice of layered electride electrode remains constrained. For example, the layered electrides Ca_2N and Sr_2N are stable as chlorides and fluorides. However, reversibility is stymied because the corresponding Ca_2NX and Sr_2NX (where X is a halogen) are wide band gap insulators. This motivated the Warren Lab to focus on the Y_2C electride because the isostructural fluoride, Y_2CF_2, has a small band gap. Furthermore, DFT and NEB calculations predict that the diffusion of fluoride through Y_2C occurs with a barrier of only 196 meV, which is nearly 100meV lower than Li^+ in CoO_2[19]. These calculations imply that the reversible movement of fluoride into the Y_2C electride host can occur at room-temperature and under electrochemical control. These properties alone lay the foundation for an electrode with comparable or better performances than state of the art lithium-ion batteries.

In the computational exploration of halogenated Y_2C, it was found that the lattice expands by 5% upon fluorination[19] with little corresponding lattice reorganization[20] while increasing the number of atoms by 66%. As a comparison, graphite in LIBs can expand up to 10%[20] while only increasing atomic capacity by 17%. This is because fluoride and bare electrons have similar effective size and charge. These findings imply that the cyclability of fluoride batteries made with layered electrides would not suffer capacity fade from lattice expansion or contraction defects. Furthermore, Y_2C and Y_2CF_2 do not suffer the same lattice reorganization costs that plague most redox active electrodes.

Upon further inspection, the intercalation of F^- into Y_2C to form Y_2CF_2 appears to be fundamentally different than all other known models of ion intercalation. Because the fluoride replaces the “bare” electride electron, the overall conversion from Y_2C to Y_2CF_2 should not occur with the reduction or oxidation of host yttrium, carbon, or fluoride atoms. This is because the electrons that are lost from Y_2C in the half-reaction:

$$[Y_2C]^{2+}(2e^-) + 2F^- \rightarrow Y_2CF_2 + 2e^-_{(circuit)}$$

have not left from atomic orbitals but have instead left from the bare electron lattice site. This represents a fundamentally new type of electron transfer process: one in which electron transfer occurs without reduction or oxidation. To support this claim, DFT calculations found that the oxidation states of Y (+1.91) and C (-2.06) in Y_2CF_2 are nearly identical to those in Y_2C (+1.95 and -2.10, respectively). In addition, it was calculated that intermediate ion movement (and the associated electron transfer) also occurs without reduction or oxidation.

The exploration of Y_2C as an electrode has unlocked an interesting class of materials that warrants further exploration. There are many variations of electrides yet to be discovered that possibly have varied or better performance as FIB electrodes. For example, by replacing yttrium with a lighter transition metal like scandium, one could expand the theoretical gravimetric capacity from 282 mAh/g to 383 mAh/g[21]. While exploring this new electride, it was discovered that the degree of hybridization between the electron and transition metals changes when yttrium is replaced with scandium. Potentially, as the electropositivity of the transition metal increases, the hybridization between bare electrons and the transition metal increases. Through this phenomenon, one would be able to tune the working voltages of future electride electrodes by doping these materials with transition metals that foster favorable volumetric and electronic properties for high capacity and high voltage FIBs.

The implementation of layered electrides into fluoride shuttle batteries could shift the current paradigm from cation batteries to anion batteries. Unfortunately, anion shuttle batteries are currently hindered by many engineering barriers that prove difficult to overcome. Many electrodes that store or release fluoride ions are based on conversion reactions that occur at metal electrodes. Although these electrodes can have a high capacity due to a high molar ratio of charge carriers to electrode material, reaching gravimetric capacities as high as 865 mAh/g with MgF_2, redox on these electrodes cause extreme volume changes that limit cyclability. Electrodes that facilitate fluoride intercalation, such as the Ruddleston-Popper type fluoride conductor[22–24], can intercalate fluoride with low diffusion barriers but at the cost of reducing specific capacity. Therefore, developing layered electrides into FIBs would offer increased cyclability compared to metal fluorides and greater specific capacity compared to current intercalation based electrodes.

1.4 Fluoride Shuttle Electrolytes

The fast conduction of fluoride ions between electrodes is essential for reversible fluoride-ion batteries. Fluoride is a monovalent anion with a relatively large ionic radius, making fluoride an ideal charge carrier because it possesses a low charge density[6]. This property is advantageous for solid state diffusion as it is predicted that ions with low charge density can move through materials with a low diffusion barrier. However, due to the limited electrostatic stabilization, F^- tends to be reactive in liquid electrolytes that have complex local electrochemical and physiochemical environments. This translates into an electrolyte with a constrained potential window that, once surpassed, degrades into corrosive products such as HF_2^-. Overcoming challenges associated with liquid electrolytes are important because they facilitate a high degree of ionic conduction at room-temperature and decrease cell fabrication cost. In this section, I discuss recent developments in controlling fluoride conduction in both the solid and liquid state for use as FIB electrolytes.

Table 1 - 1: Comparisons of charge density revealing fluoride having the lowest charge density of 1.00. "q" describes the charge of the atom while r represents the ionic radius.

Element	q/r
Li	1.32
Na	1.03
Mg	2.77
Al	5.29
F	1.00
Zn	2.70

1.4.1 Solid Fluoride Shuttle Electrolytes

The slow progression of FIB research has been historically bottlenecked by solid-state electrolytes, and in fact, initial proposals in the 1970s called for excessive >400°C operating temperatures in order to

achieve sufficient fluoride-conductivity in the suggested solid-electrolyte, CaF_2[25]. The first experimental demonstration of FIBs fortunately achieved a much lower operating temperature of ~180°C by employing KF-doped PbF_2[26]. However, this still represented unreasonable conditions for typical commercial applications. Subsequent efforts in the following decade failed to identify suitable solid-state electrolytes that conduct fluoride at room temperature, leading to diminished focus on FIBs. It wasn't until 2011 that FIBs regained scientific attention when a rechargeable FIB was demonstrated at ~150°C with an improved Ba-doped LaF_3 solid-electrolyte[4]. Still, this electrolyte displayed poor ionic conductivity ($2.8x10^{-4}$ S cm^{-1} at 160°C) relative to typical Li-ion conductors at the time ($\backsim 10^{-4}$ S cm^{-1} at RT).

With plenty of room to improve, many material systems have since been explored in search of room-temperature fluoride-ion conductors that are stable and easily processed. Here, the majority of focus lies on alkaline-earth fluorides (fluorite-type crystals) and rare-earth metal fluorides (tysonsite-type crystals). Both structure-types exhibit poor conductivities as pure phases but experience orders of magnitude improvement in ionic-conductivity via empirically-optimized aliovalent doping, ball milling, and sintering[27]. While these strategies are effective in producing solid-electrolytes suitable for room-temperature batteries (e.g. fluorite-type $BaSnF_4$[28] and tysonite-type $Sm_{0.95}Ca_{0.05}F_{2.95}$[29] both achieve $1x10^{-4}$ S cm^{-1} at RT), conductivities are found to be extremely sensitive to doping amounts as well as highly dependent on the high-energy ball milling and high-temperature sintering (>800°C), which are expensive and scale poorly. As an alternative approach, easily-processed $La_{1-x}Ba_xF_{2-x}$ electrodes have been made by liquid-based precipitation of the solid electrolyte and exhibit comparable ionic conductivity relative to their ball-milled and sintered counterparts[30] ($1.26x10^{-4}$ S cm^{-1} at 60°C vs. $3.0x10^{-6}$ S cm^{-1} at RT, respectively). So, while conductivities largely limit the candidate systems for solid-state electrolytes, material processing provides another roadblock to FIB utilization that is actively being addressed. Further, even the best solid-electrolytes that have been successfully employed in FIBs (e.g. $PbSnF_4$ and $Sm_{0.95}Ca_{0.05}F_{2.95}$) possess small electrochemical windows and limited chemically compatible electrodes. There has thus been significant progress made on solid-state electrolytes with multiple room-temperature candidates being identified and demonstrated, but many challenges remain in order to realize high-voltage and highly-cyclable FIBs[31].

1.4.2 Liquid Fluoride Shuttle Electrolytes

The fast conduction of fluoride ions between electrodes is essential for reversible fluoride-ion batteries. Given fluoride's monovalency and large ionic radius, fluoride is an ideal charge carrier because it possesses a low charge density[6]. This property is advantageous for diffusion as it is predicted that ions with low charge density can move through materials with a low diffusion barrier. However, due to the limited electrostatic stabilization, F^- tends to be reactive in liquid electrolytes under complex electrochemical and physiochemical environments. This translates into an electrolyte with a constrained potential window that, once surpassed, degrades into corrosive products such as HF_2^-. Overcoming challenges associated with liquid electrolytes are important because they facilitate a high degree of ionic conduction at room-temperature and decrease cell fabrication cost.

Due to the difficulty in preparing liquid electrolytes that shuttle fluoride, little research has been conducted towards anhydrous room-temperature fluoride-ion batteries. A leading challenge is that common metal fluoride salts are insoluble in organic aprotic solvents past 0.05M[32]. Meanwhile, organic fluoride salts have improved solubility yet readily degrade to bifluoride ions. To add to this issue, commercially available anhydrous fluoride salts, such as tetramethylammonium fluoride, do not dissolve at concentrations needed for liquid electrolytes[6]. Recently, however, a collaboration with researchers at the Honda Research Institute that provided access to a then-undisclosed liquid fluoride shuttle electrolyte that was stable in nonaqueous conditions and performed within a large voltage window[33].

Developed by Davis et al., this electrolyte was able to overcome the common challenges in liquid fluoride electrolytes by addressing key issues that plague electrolyte stability. Corrosive byproducts form from β-H elimination reactions that occur at varying potentials dependent on the solvent, salt, and electrolyte impurities. To address this, Davis et al. used branched neopentyl groups in neopentyl-substituted alkylammonium salts. In addition to lacking β-hydrogens, this electrolyte salt was highly polar and able to dissolve in bis(2,2,2-trifluoroethyl) ether (BTFE) past 2.2M. BTFE is an ideal solvent because of the CH_2 groups which separate the oxygen and CF_3 moieties present in the neopentyl chains. Additionally, using molecular dynamics, Davis et al. also found the BTFE molecule to flex in 3 dimensions to chelate with the fluoride anion[34]. This chelation mechanism between the anion and the CH_2 groups in BTFE stabilizes the anion and allows for greater solubility. Additionally, the chelation effect hinders the long-term degradation

of the electrolyte into bifluoride and HF. These physiochemical properties allow a super-concentrated electrolyte to be synthesized that remains stable in ambient conditions. During operation, Davis found that this electrolyte exhibits a relatively large stability window of 4V with a high fluoride conductivity of 7.95mS/cm at room-temperature. Furthermore, by adding amide co-solvents, Davis et al. were able to improve the ionic conductivity of the electrolyte, facilitating the separation of neopentyl cations from the fluoride anion. These experiments set an important precedent for the electrolyte's tunability.

When applied to the layered electride system, this electrolyte would enable reversible operation and further allows the direct experimental study of the EAX mechanism at room-temperature. However, due to the complexity of the electrochemical environment as well as the novelty of the system, challenges must be resolved.

1.5 Overcoming Challenges in Battery Devices

To realize electrochemical EAX, one must be able to understand and subsequently control the interactions between the liquid electrolyte and electride electrodes under an applied voltage. Indeed, the complexity of changing potentials in a battery system causes unpredictable reactions that can lead to both favorable and unfavorable electrochemical environments. Therefore, understanding the electronic and morphological conditions in the electrolyte and electrode at their interface under working conditions is important for cells with long cycle life. In this section, I outline events that lead to the corrosion of layered Y_2C electrodes and degradation of the supporting electrolyte. These mechanisms are identified as the two main barriers that must be overcome to electrochemically induce EAX. Once identified, I provide solutions adopted from previous bodies of knowledge to realize the experimental cycling of electride enhanced fluoride ion batteries.

1.5.1 Electrolyte Degradation

To achieve long cycle life battery operation, the working voltage of the electrode must fall within the stability window of the electrolyte or else constant electrolyte degradation can be expected. Ultimately, understanding why electrolytes degrade at high absolute voltages can lead to designing electrolytes that extend the window into operating voltages without electrolyte degradation.

An approximate model to explain electrolyte degradation in battery chemistry states that the electrolyte stability is dictated by the solvent's highest occupied molecular orbital (HOMO) and lowest unoccupied molecular orbital (LUMO). In this model, the reduction of the electrolyte occurs at electron energy levels higher than the LUMO of the solvent and oxidation occurs at energy levels lower than the HOMO of the solvent. A more accurate model considers electrolyte concentrations, solvation shell dynamics, and evolving SEI reactions into predictions of electrolyte stability[35]. This refined model frames electrolyte instability as an engineering problem rather than an innate error in solvent choice - where one can design an electrolyte for optimized performance.

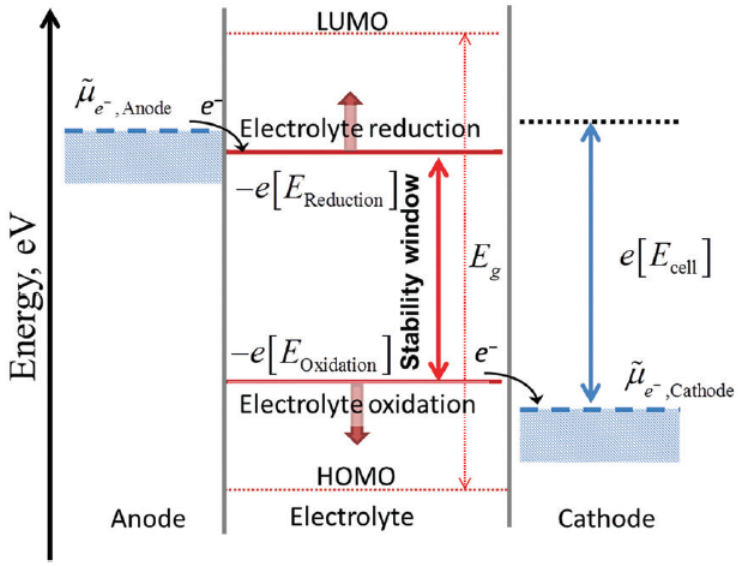


Figure 1 - 3 [35]: Visualization of complex stability window of electrolytes in the oxidizing (at the cathode) and reducing (at the anode) regimes. Solvation and concentration play into the overall stability of the electrolyte, while evolving electrochemical environments contribute to charge transfer mechanics.

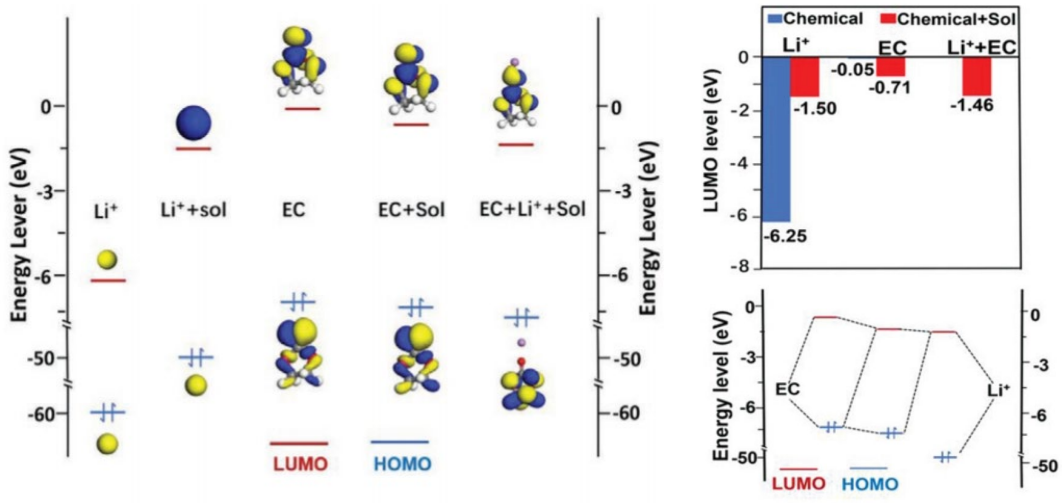


Figure 1 - 4 [36]: Energy schema for the sacrificial reduction of electrolyte additive ethylene carbonate to form surface stabilizing products. These products form an interphase on the surface of lithium-ion battery electrodes to reduce electrode expansion, cracking, defects, and dissolution.

To inform my route towards experimental EAX, I can look at the first instance of LIB electrolyte engineering. Capacities of initial secondary LIBs created in the 1970s faded over time due to the instability of polypropylene carbonate (PC) based electrolytes. To overcome this issue, Dahn et al.[36] incorporated ethylene carbonate (EC) at a 1:1 v/v ratio. This resulted in the sacrificial degradation of the ethylene carbonate/lithium solvation structure onto the surface of the electrode, creating a passivating layer through which lithium ions could diffuse. The preferential degradation of the EC allowed Dahn et al. to engineer high-capacity LIBs that could be cycled repeatedly. In the FIB case, cosolvents can be blended into the electrolyte to increase the stability window of the electrolyte. For example, by incorporating straight-chain glycol ethers, Davis et al. found that the cathodic stability could be increased by 0.4V, widening the total stability window from 4.1V to 4.5V. As the working voltage of the Y_2C/Y_2CF_2 system lies just below the cathodic stability of the base electrolyte, the incorporation of cosolvents would enable the intercalation of fluoride without significant electrolyte degradation.

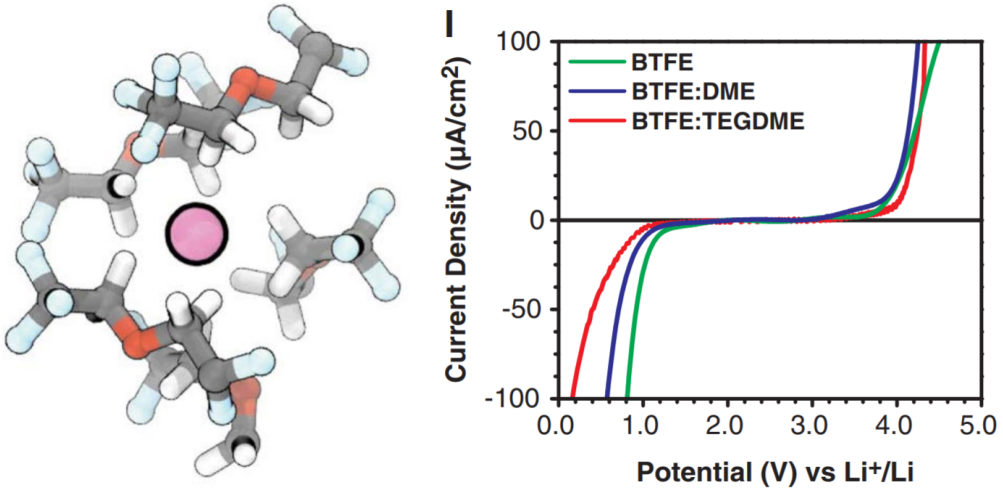


Figure 1 - 5 [6]: (Left)Solvation structure of the fluoride anion in Np_1F/BTFE solution. Fluoride is stabilized, reducing its ability to form HF/HF_2^-. (Right) Electrochemical stability window of high-performance fluoride containing electrolyte blend.

1.5.2 SEI Formation

Previous studies on transition metal electrodes show electrode corrosion to greatly affect performance[6]. The dissolution of transition metal species from the electrode is unpredictable because it is driven by trace electrolyte impurities and side reactions. In the case of the Np1F/BTFE electrolyte, Davis et al. noted the presence of Cu, Bi, and Pb transition metals in various liquid electrolytes after FIB cycling. Davis explains the dissolution of electropositive transition metals through an unintended introduction of bifluoride ions that are highly reducing. In many FIB electrolytes, the formation of HF occurs with organic solvents that are strongly basic, such as acetonitrile. In this case, fluoride reacts with the weakly-acidic protons of acetonitrile to form bifluoride. The Np_1F/BTFE electrolyte was designed by Davis et al. to be unreactive with fluoride anions under standard conditions for long periods of time. However, Davis et al. still found trace amounts of HF in F-NMR analysis of the current

Table 1 - 2 [6]: Transition metal dissolution measured via ICP-MS in the presence of fluoride containing electrolyte solutions, specifically Np_1F/BTFE.

Battery Composition	Test Parameters	ICP-MS [indicated element] (μg)
WE: Bi foil (146.4 mg; 3x5 mm) CE: Pt wire RE: 0.01 M AgOTf/MPPy-TFSI Electrolyte: 0.1 M TMAF/MPPy-TFSI	Charge to: 2.82 V vs Li^+/Li 200 μA (1 hour cut off) Discharge to: 1.72 V vs Li^+/Li 50 μA (voltage cut off)	463 [Bi]
WE: Pb foil (11.2 mg; 2x5 mm) CE: Pt wire RE: 0.01 M AgOTf/MPPy-TFSI Electrolyte: 0.1 M Np_1F/BTFE	Charge to: 2.42 V vs Li^+/Li 300 μA (1 hour cut off) Discharge to: 1.72 V vs Li^+/Li 25 μA (voltage cut off)	441 [Pb]
WE: Cu:PVDF (90:10; 4.55 mg) CE: Pt wire RE: 0.01 M AgOTf/MPPy-TFSI Electrolyte: 1 M Np_1F/BTFE	Charge to: 3.82 V vs Li^+/Li 10 μA (60 hours cut off; never reached 3.82 V) Discharge to: 1.92 V vs Li^+/Li (voltage cut off)	180 [Cu]

system. Interestingly, Davis concluded that observed HF arises from small amounts of unknown protic impurities present in solution and not from solvent degradation. When transferring the electrolyte to my system that also contains electropositive Y, one can expect to have similar dissolution reactions from analogous trace impurities in solution. Therefore, it is important to create an electrochemical cell configuration that actively decreases the degree of interactions between the impure electrolyte and electrode. This can be achieved by designing a protective barrier that exists in between the electrode and electrolyte. This is known as a solid electrolyte interphase.

Tuning the solid electrolyte interphase (SEI) relies on an understanding of the formation and properties of this interphase. When the anode comes in contact with the electrolyte, a reaction spontaneously occurs at the surface of the electrode due to instability in solution[37]. The products of these reactions are either soluble or insoluble in the electrolyte solution, and the latter can precipitate on the surface of the electrode forming a “mosaic of microphases”[38]. The film is composed of a complex inorganic and organic amalgam that extends the range of the electron tunneling distance, about 1nm-3nm[38]. In an ideal situation, the passivation layer acts as a sort of solid electrolyte, able to conduct ions while resisting electrons. SEI formation, however, is thought of as the most unpredictable and complex process during battery operation, and ideal SEIs do not form often. As a result, reactions can lead to accelerated degradation of battery components, decreased capacity, and increased overpotential. However, engineered SEI formation can lead to greater stability of both the electrolyte and electrode and safety throughout the battery lifetime.

Engineered, or artificial, SEIs are beneficial over natural SEIs because the natural SEI forms using environmental constituents, i.e. lithium in LIBs or fluorine in FIBs. Therefore, over time, the capacity fades as the concentration of charge carriers decreases. Additionally, artificial SEIs have the benefit of protecting the bare electrode from corrosive impurities in the electrolyte.

Artificial SEIs can be organic or inorganic in composition. For example, to improve the stability of the electrodes, Davis modified the surface of cerium foil using 1H,1H,2H,2H - perfluorooctyltriethoxysilane (FOTS). The silane was deposited onto the surface of the electrode through electrodeposition and monitored with impedance spectroscopy. This polymer artificial SEI facilitated the Ce-to-CeF_3 conversion and increased cyclability. An inorganic core-shell SEI was also developed for Cu nanoparticle electrodes

to protect Cu from dissolution, protect the electrolyte from decomposition, restrict volume expansion, and selectively diffuse fluoride ions over 5nm. For this, Davis chose LaF_3 as the shell because of the inert nature of the material and the high conductivity of LaF_3. Cu was chosen as an ideal electrode in this Cu-LaF_3 system due to its high capacity of 528 mAh/g. In this electrode, Cu was converted to CuF_2 over 7 cycles (Figure 1-6). Davis attributes capacity fade in this material to diffusion barriers that arise inside of the Cu nanoparticles. In layered electride electrodes, fluoride is expected to reversibly diffuse with low energetic barriers. Therefore, the Y_2C/Y_2CF_2 system can be used in an analogous system yet achieve higher capacities and better cyclability.

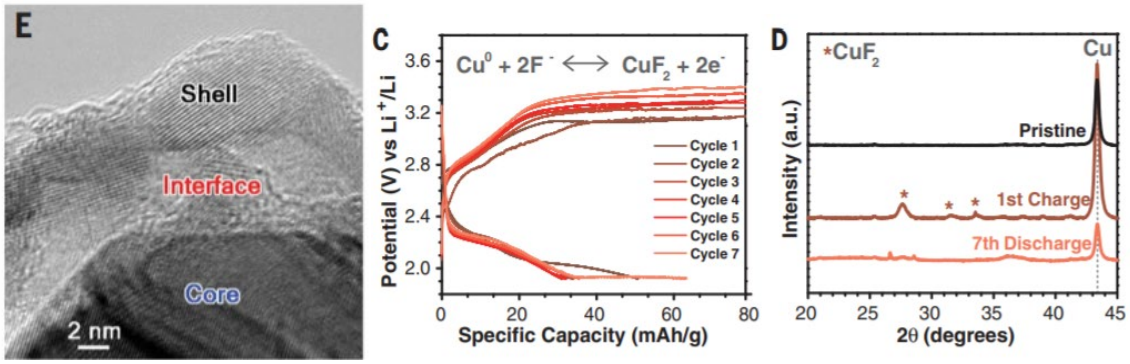


Figure 1 - 6 [6]: LaF_3 artificially engineered SEI reduces the dissolution of metal into the electrolyte, stabilizing the cycle lifetime of battery electrodes in the presence of Np_1F/BTFE electrolyte.

1.6 Overview of the research described in this thesis

The use of layered electrides in fluoride ion batteries unlock high-capacity cells with long cycle stability. Interestingly, Y_2C and Sc_2C electrides can store two fluorides in every unit cell, making batteries with twice the volumetric capacity compared to state-of-the-art lithium-based cells. In combination with a CuF_2 cathode, these cells could reach voltages of 2.8 volts. Furthermore, the realization of redox-less electron anion exchange under electrochemical manipulation has interesting implications for understanding energy transfer mechanisms. Calculations show that EAX occurs without significant lattice expansion or contraction which often leads to degradation in electrodes over time. Yet, to use these electrodes in a working cell, hurdles in surface stability, bulk stability, and ionic conductivity must be addressed. To this end, this dissertation systematically addresses the scientific and engineering gaps to produce a high cycle life, large voltage battery based on EAX in layered electrides.

I first back the theoretical basis for EAX using experimental studies of bulk electronic structure of the Y_2C/Y_2CF_2 system. Using x-ray absorption spectroscopy paired with DFT modeling, I confirmed that the yttrium host cation in the Y2C electride does not undergo significant reduction or oxidation upon exchange for fluoride. This study provides the first experimental evidence for a new mechanism that could have profound implications for the cycle lifetime of fluoride-ion batteries.

I then describe high-throughput methods for doping Y_2CF_2 to optimize fluoride transport in the material. By systematically exploring the energies of doped systems, I predict candidate dopants that could be incorporated into Y_2C or Y_2CF_2 to systematically induce vacancy sites. I then explore the effects of these dopants on the electronic characteristics of the Y_2C electride, and use these predictions to synthesize a Ca doped Y_2CF_2 for enhanced ionic conductivity.

Next, I describe my experimental efforts to incorporate Y_2C as an anode into a room temperature, fluoride-ion battery. Using these experiments, I identify key barriers that inhibit the full cycling stability of the electrode. These barriers exist at the interface of the Y_2C and the electrolyte.

To address the highly reactive surface of the electrode, I outline my studies into developing an artificial SEI. This SEI is shown to passivate the electride to oxygen and fluorine. The surface thickness and composition are tunable, establishing a foundation to explore the characteristics within a battery architecture.

Finally, I address the instability of the electrolyte by switching to a high-temperature, solid-state electrolyte. By optimizing the fabrication of this electrode, I was able to reduce reactions between Y_2C and $Ca_{0.5}Ba_{0.5}F_2$ electrolyte. These optimizations led to the long-term cycling of a battery based on Y_2C and electron-anion exchange.

Ultimately, further studies of electrochemical devices that exploit electron anion exchange will have exciting and widespread implications for energy storage.

REFERENCES

1. Moeller, K.-C. Overview of battery systems. in *Lithium-Ion Batteries: Basics and Applications* (ed. Korthauer, R.) 3–10 (Springer Berlin Heidelberg, Berlin, Heidelberg, 2018). doi:10.1007/978-3-662-53071-9_1.

2. Julien, C., Mauger, A., Vijh, A. & Zaghib, K. *Lithium Batteries Science and Technology*.

3. Consortium for Advanced Batteries, F. *NATIONAL BLUEPRINT FOR LITHIUM BATTERIES EXECUTIVE SUMMARY*. (2021).

4. Anji Reddy, M. & Fichtner, M. Batteries based on fluoride shuttle. *J Mater Chem* **21**, 17059–17062 (2011).

5. Nowroozi, M. A. *et al.* Fluoride ion batteries – past, present, and future. *J Mater Chem A Mater* **9**, 5980–6012 (2021).

6. Davis, V. K. *et al.* Room-temperature cycling of metal fluoride electrodes: Liquid electrolytes for high-energy fluoride ion cells. *Science (1979)* **362**, 1144 (2018).

7. Keve, E. T. & Skapsri, A. C. *Ca,N: A Nitride with a Layer Structure 829*. vol. 22 (1966).

8. Le Roy, J., Moreau, J., Paccard, D. & Parthd, E. *Pt-Y Ca-N 79Let*.

9. Matsuishi, S. *et al.* High-Density Electron Anions in a Nanoporous Single Crystal: [Ca24Al28O64]4+(4e-). *Science (1979)* **301**, 626–629 (2003).

10. Lee, K., Kim, S. W., Toda, Y., Matsuishi, S. & Hosono, H. Dicalcium nitride as a two-dimensional electride with an anionic electron layer. *Nature* **494**, 336–340 (2013).

11. Zhang, X. *et al.* Two-dimensional transition-metal electride Y2C. *Chemistry of Materials* **26**, 6638–6643 (2014).

12. Zhao, S., Li, Z. & Yang, J. Obtaining two-dimensional electron gas in free space without resorting to electron doping: An electride based design. *J Am Chem Soc* **136**, 13313–13318 (2014).

13. Druffel, D. L., Woomer, A. H., Kuntz, K. L., Pawlik, J. T. & Warren, S. C. Electrons on the surface of 2D materials: from layered electrides to 2D electrenes. *J Mater Chem C Mater* **5**, 11196–11213 (2017).

14. Druffel, D. L. *et al.* Experimental Demonstration of an Electride as a 2D Material. *J Am Chem Soc* **138**, 16089–16094 (2016).

15. Woomer, A. H., Druffel, D. L., Sundberg, J. D., Pawlik, J. T. & Warren, S. C. Bonding in 2D Donor-Acceptor Heterostructures. *J Am Chem Soc* **141**, 10300–10308 (2019).

16. Hu, J. *et al.* 2D Electrides as Promising Anode Materials for Na-Ion Batteries from First-Principles Study. *ACS Appl Mater Interfaces* **7**, 24016–24022 (2015).

17. Fan, S. *et al.* Theoretical Investigation of the Intercalation Chemistry of Lithium/Sodium Ions in Transition Metal Dichalcogenides. *Journal of Physical Chemistry C* **121**, 13599–13605 (2017).

18. Zobel, D. Bildung und Eigenschaften von rotem Ca2NCl. *ZAAC - Journal of Inorganic and General Chemistry* **342**, 270–276 (1966).

19. Druffel, D. L. *et al.* First-Principles Prediction of Electrochemical Electron-Anion Exchange: Ion Insertion without Redox. *Journal of Physical Chemistry Letters* **11**, 9210–9214 (2020).

20. Druffel, D. L. *et al.* Synthesis and Electronic Structure of a 3D Crystalline Stack of MXene-Like Sheets. *Chemistry of Materials* **31**, 9788–9796 (2019).

21. McRae, L. M. *et al.* Sc2C, a 2D Semiconducting Electride. *J Am Chem Soc* **144**, 10862–10869 (2022).

22. Nowroozi, M. A. *et al.* High cycle life all-solid-state fluoride ion battery with La2NiO4+d high voltage cathode. *Commun Mater* **1**, (2020).

23. Nowroozi, M. A., Ivlev, S., Rohrer, J. & Clemens, O. La2CoO4: A new intercalation based cathode material for fluoride ion batteries with improved cycling stability. *J Mater Chem A Mater* **6**, 4658–4669 (2018).

24. Nowroozi, M. A., Wissel, K., Rohrer, J., Munnangi, A. R. & Clemens, O. LaSrMnO4: Reversible Electrochemical Intercalation of Fluoride Ions in the Context of Fluoride Ion Batteries. *Chemistry of Materials* **29**, 3441–3453 (2017).

25. Delcet, J., Heus, R. J. & Egan, J. J. Electronic Conductivity in Solid CaF2 at High Temperature. *J Electrochem Soc* **125**, 755 (1978).

26. Kennedy, J. H. & Miles, R. C. Ionic Conductivity of Doped Beta-Lead Fluoride. *J Electrochem Soc* **123**, 47 (1976).

27. Chadwick, A. V. High-temperature transport in fluorites. *Solid State Ion* **8**, 209–220 (1983).

28. Liu, L. *et al.* SnF2-based fluoride ion electrolytes MSnF4 (M = Ba, Pb) for the application of room-temperature solid-state fluoride ion batteries. *J Alloys Compd* **819**, 152983 (2020).

29. Molaiyan, P. & Witter, R. Synthesis and characterization of Ca(1−)SmF(2+) (0 ≤ x ≤ 0.15) solid electrolytes for fluoride-ion batteries. *Material Design & Processing Communications* **3**, e226 (2021).

30. Bhatia, H. *et al.* Conductivity Optimization of Tysonite-type La1–xBaxF3–x Solid Electrolytes for Advanced Fluoride Ion Battery. *ACS Appl Mater Interfaces* **9**, 23707–23715 (2017).

31. Sundberg, J. D. *et al.* High-throughput discovery of fluoride-ion conductors via a decoupled, dynamic, and iterative (DDI) framework. *NPJ Comput Mater* **8**, 106 (2022).

32. Wynn, D. A., Roth, M. M. & Pollard, B. D. *THE SOLUBILITY OF ALKALI-METAL FLUORIDES IN NON-AQUEOUS SOLVENTS WITH AND WITHOUT CROWN ETHERS, AS DETERMINED BY FLAME EMISSION SPECTROMETRY*. *Talanta* vol. 31 (1984).

33. US20210151755A1 (1).

34. Davis, V. K. *et al.* Fluoride-ion solvation in non-aqueous electrolyte solutions. *Mater Chem Front* **3**, 2721–2727 (2019).

35. Peljo, P. & Girault, H. H. Electrochemical potential window of battery electrolytes: The HOMO-LUMO misconception. *Energy Environ Sci* **11**, 2306–2309 (2018).

36. Fong, R., von Sacken, U. & Dahn, J. R. Studies of Lithium Intercalation into Carbons Using Nonaqueous Electrochemical Cells. *J Electrochem Soc* **137**, 2009–2013 (1990).

37. Dey, A. N. Lithium anode film and organic and inorganic electrolyte batteries. *Thin Solid Films* **43**, 131–171 (1977).

38. Peled, E. & Menkin, S. Review—SEI: Past, Present and Future. *J Electrochem Soc* **164**, A1703–A1719 (2017).

CHAPTER 2: METHODS

2.1 Introduction

Throughout my time at the University of North Carolina at Chapel Hill, I have gained expertise as a battery materials engineer through the acquisition of technical skills. This methods section outlines processes not documented in other sections of this thesis. Here, I detail my methods for developing computational models of the physical structure of electrides and their associated electronic structure. Next, I detail methods of synthesis using high power arc welding and annealing under inert conditions. I then describe the fabrication of electrodes in both room-temperature and high temperature electrochemical cells. Finally, I describe my methods of physical and spectroscopic characterization.

2.2 Computational Methods

2.2.1 High Throughput DFT Modeling

The systematic doping of Y_2C and Y_2CF_2 proceeded using a high-throughput method developed using VASP[1] and Python. My goal was to compare the formation energies of structures according to a series of acceptance criteria for the metal dopant to act as intended – i.e. a vacancy conductor. Thus, we aimed to produce 5 unique structures; 1) a metal doped Y_2C, 2) a metal doped $Y_{2-x}M_xCF_2$, 3) a metal-doped $Y_{2-x}M_xCF_{2-x}$, where the vacancy was localized near the dopant site, 4) a metal doped $Y_{2-x}M_xCF_{2-x}$, where the vacancy localized far from the dopant, and 5) a metal doped $Y_{2-x}M_xCF_{2-(x*ox.)}$, where 2 vacancy sites were localized near the dopant.

By comparing the formation energies of these structures, we could determine 1) if the doped structure was synthesizable, 2) if the structure favored the formation of vacancies near the dopant, 3) if the structure hindered full fluorination, and 4) if the dopant was stable in the yttrium site.

First, I optimized the geometry of the Y_2C and $Y2CF_2$ cell for an accurate foundation to generate doped supercell structures. For each, I used the r^{2}SCAN[2] functional with an energy cutoff of 520eV and a k-spacing of 0.15. The CONTCAR of the Y_2C geometry optimization was used to seed structure (1) whereas the CONTCAR of the Y_2CF_2 geometry optimization was used to seed structures (2, 3, 4, 5).

A supercell was generated using the PyMatGen package[3] within Python. First, the CONTCAR was converted to the primitive cell using the structure.get_primitive_structure() method in PyMatGen. This output was then fed into a supercell generation script that created a cubic cell that had at least a 9-angstrom lattice vector. Overall, this generated a cubic Y_2CF_2 structure with 90 atoms, and a cubic Y_2C structure with 54 atoms.

```
from pymatgen.io.vasp import Poscar
from pymatgen.transformations.advanced_transformations import CubicSupercellTransformation

poscar = Poscar.from_file("CONTCAR")
#poscar = Poscar.from_file("primitive")
#structure = poscar.structure
structure = poscar.structure
modified_structure = structure.get_primitive_structure()

#t = CubicSupercellTransformation(min_length=9)
#modified_structure = t.apply_transformation(structure)

#modified_structure.to(filename="POSCAR_super", fmt="poscar")
modified_structure.to(filename="primitive", fmt='poscar')
```

```
1   from pymatgen.io.vasp import Poscar
2   from pymatgen.transformations.advanced_transformations import CubicSupercellTransformation
3
4   #poscar = Poscar.from_file("CONTCAR")
5   poscar = Poscar.from_file("primitive")
6   structure = poscar.structure
7   #structure = poscar.structure
8   #modified_structure = structure.get_primitive_structure()
9
10  t = CubicSupercellTransformation(min_length=9)
11  modified_structure = t.apply_transformation(structure)
12
13  modified_structure.to(filename="POSCAR_super", fmt="poscar")
```

Figure 2 - 1: (Top) script used to generate the primitive from the CONTCAR structure file output from a VASP geometry optimization. (Bottom) Script used to generate the cubic supercell using functions in PyMatGen.

From the supercells, I used another script to generate all geometry optimization and single point energy calculation files for each doped structure. This script first created the 5 folders that contain calculations for each previously identified doped structure (1-5). Using file writing functions, I replaced one yttrium site with

a dopant from a list of 30 metals. These metals included ['Li', 'Na', 'K', 'Rb', 'Cs', 'Be', 'Mg', 'Ca', 'Sr', 'Ba', 'Sc', 'Ti', 'V', 'Cr', 'Mn', 'Fe', 'Co', 'Ni', 'Cu', 'Zn', 'Y', 'Zr', 'Nb', 'Mo', 'Tc', 'Ru', 'Rh', 'Pd', 'Ag', 'Cd'].

From these generated doped structures, I used PyMatGen to autogenerate POTCAR pseudopotentials. I saved the potentials (POTCAR) and atomic positions file (POSCAR) to the given folder. Then I moved the INCAR file from a standardized “setup” subfolder and a submit file. Finally, I used a script to move through each subdirectory to autosubmit the calculations to the Warwulf compute cluster. Further analyses on the structures are described in *Chapter 4*.

2.2.2 Processing and Modeling XANES Data

2.2.2.1 XAS

X-ray absorption spectroscopy (XAS) is a spectroscopic technique in which high energy x-rays are used to probe the electronic structure of bulk materials. XAS is a common technique to determine the precise contributions of local geometry to electronic structure for specific atoms within a crystal lattice or metal complex[4]. XAS probes the absorption of a high-energy photon with a large enough energy to excite a core orbital. An excitation from an x-ray absorption event results in a decrease in transmission. As the energy of the incoming photon increases, one can analyze energy differences between core states and unoccupied states.

XAS contains two distinct regions: the x-ray absorption near-edge spectra (XANES) and the extended x-ray absorption fine structure (EXAFS). EXAFS signal results from the type, number, and distance of coordinated atoms, whereas XANES provides information on the oxidation state, bond covalency, coordination geometry, and coordination number of an atom[5].

2.2.2.2 HERFD-XANES

In XAS spectra, information about oxidation state is often lost because spectra are smeared by the short excited-state lifetime[5]. Oxidation states require an energy resolution of 1-2 eV, but in many elements, especially heavier elements like yttrium, this energy resolution is not typically achievable. To address this challenge, we have instead used an XAS-related technique called high-energy resolution fluorescence detected XANES (HERFD-XANES). Here, by using fluorescence to measure a long-lived excited state, a

high-resolution spectrum of yttrium is obtained. By probing the K-edge with HERFD-XANES, small changes in oxidation state between Y_2C and Y_2CF_2 can potentially be resolved.

The k-edge contains many features that correlate a material's electronic structure to its physical characteristics. As absorption energy increases, a peak may be observed known as the "pre-edge". This feature can be attributed to excitations from 1s to the d-band in transition metals. Therefore, unoccupied states in the 4d band account for both Y_2C and Y_2CF_2 pre-edge features. Past the pre-edge feature, a main edge can be observed. The intensity of this peak corresponds to the intensity of x-rays that transmit to the detector. Unfortunately, extrinsic factors such as self-absorption and attenuation can profoundly affect this intensity. Thus, to quantify the position of the energy of the edge feature, we take the derivative of the XANES spectrum and assign the k-edge as maximum point along the edge.

The energy transitions between the 1s and 5p orbitals cause the edge peak at 17051.6eV for Y_2C and 17052.7eV for Y_2CF_2. The excitation energies are shifted down about 1-2eV from Y_2C to Y_2CF_2. These shifts in energy can be caused by many factors. For instance, bonding fluorine to yttrium can shift the absorption energy due to orbital hybridization. The shift could also be caused by Coulombic interactions between the excited electron interacting with electrons in the valence band and the orbitals of surrounding atoms. This effect, known as screening, can be affected by covalency, atomic number, coordination number, and oxidation state[5].

Due to the changes in structure between the Y_2C and Y_2CF_2, the interpretation of XAS measurements can be difficult. Indeed, XAS is primarily a "fingerprinting" technique, where a standard sample is used to calibrate a spectrum, and slight additions such as surface absorbate[6], doping concentration[7], and geometry[8] can result in systematic peak shifts. To better understand the spectral dependence on structure in the Y_2C/Y_2CF_2 system, one must create a model to relate features to electronic structure effectively.

2.2.2.3 EXCITING Modeling of XAS Data

The x-ray absorption near edge spectra (XANES) was modeled using a computational pipeline designed for highly accurate simulations of excited states using core-hole attraction modeled by the Bethe-Salpeter Equation implemented by the EXCITING code[9,10]. BSE is among the most rigorous of approaches

for calculating the core-hole absorption XAS spectra, particularly in the near-edge region that gives information about oxidation states[11]. When paired with DFT, we are able to accurately model core-hole attraction and its effects on energy of the bands under coulombic attraction and dynamic screening effects.

First, we performed a structure relaxation of Y_2C and Y_2CF_2 structures using the VASP, implementing the hybrid density HSE06 functional[12]. The plane-wave energy cutoff was 520 eV and a gamma centered k-point grid with a spacing of 0.25 $Å^{-1}$ was used. The output structure was fed into the input generation module created by Lightshow[13], a Python package designed to easily generate spectroscopy input files. We used the yttrium K-edge using default EXCITING parameters.

We then modeled the XAS spectra by first modeling the ground state with the GGA PBE functional with a k-point grid of 6x6x6. The XAS was broadened to a Lorentzian broadening setting of 0.1 to match lifetime broadening effects in experiment. An energy window between 613 eV and 645 eV was used. The output of this script produced 3 spectra polarized on the X, Y, and Z axes. As the XAS measurement was performed on bulk powder, the modeled spectra were averaged together. Finally, the modeled spectra were energy corrected to match the experimental energy shift of Y_2C or Y_2CF_2.

2.2.3 Extended X-ray Absorption Fine Structure

The second feature of XAS is the oscillatory features past the main edge. The energy of the photoelectron is so large that the electron escapes the bounds of a materials bands and moves into a state of the continuum. These high energy photoelectrons are able to interact with the electrons in surrounding atoms, backscattering and interfering constructively or destructively to form oscillatory peaks in the high-energy absorption spectrum[14–20]. One can model the interference pattern to form a radial distribution of the atomic coordination based on the coordination number and atom type. This model is known as the EXAFS equation:

$$x(k) = \sum_j \frac{N_j f_j(k) \exp\left[-2k^2\sigma_j^2\right] \exp\left[-\frac{2R_j}{\lambda}\right]}{kR_j^2} \sin\left[2kR_j + \delta_j(k)\right]$$

Where energy is first converted to the momentum of the photoelectron, k. f(k) then represents the amplitude of the oscillatory region. When solving the EXAFS equation, we are left with radius (R), coordination (N),

and measure of disorder of the surrounding atoms (σ) as unknowns. By taking the Fourier transform of the EXAFS equation, we can analyze the radial distribution of the spectrum, where peaks correspond to a coordinated atom, and peak height corresponds to the number and type of the coordinated atom[21].

To perform accurate modeling of the extended x-ray absorption fine structure (EXAFS), I first collected XAS data at the Cornell High Energy Synchrotron Source. Please refer to methods section 2.4.2.1 for details regarding measurement collection. For analysis, the data was collected repeatedly (5-15 scans) to increase the signal relative to the noise at energies above the absorption edge. These data were averaged for every point collected.

2.2.3.1 Processing and Modeling of EXAFS Data

Once averaged, data were imported into the Athena Software[22] for XAS processing. This was done by assigning the x-values as the energy column of the data, and the intensity measured on detector “Pilroi1 normalized by a secondary detector I2 as the y-values. Once imported into Athena, the data was saved as a project file that could then be imported into Larch XAS Viewer software. A comprehensive guide to using Larch to model EXAFS data is available on YouTube from Matthew Newville, or via Larch Documentation.

Once imported, the data is first background subtracted and normalized (Figure 2-2) to 1. In this normalization process, μ(E) is adjusted to range from approximately zero below the edge to about one above the edge. This normalization process removes differences from how raw data was measured, such as transmission or fluorescence, and to help scale the values of the data, so samples are more easily compared.

To begin the process, raw data is read into the software. Once the data is read, the edge position (E_0) must be determined. I used the default setting, which is the maximum of the first derivative. Next, the range of μ(E) is specified, and Larch plots a “pre-edge line” and a “post-edge curve”. The pre-edge is fitted to a line using polynomial. The fit values are then subtracted from the data. Finally, the values are normalized such that the post edge will be at 1.0 μ(E).

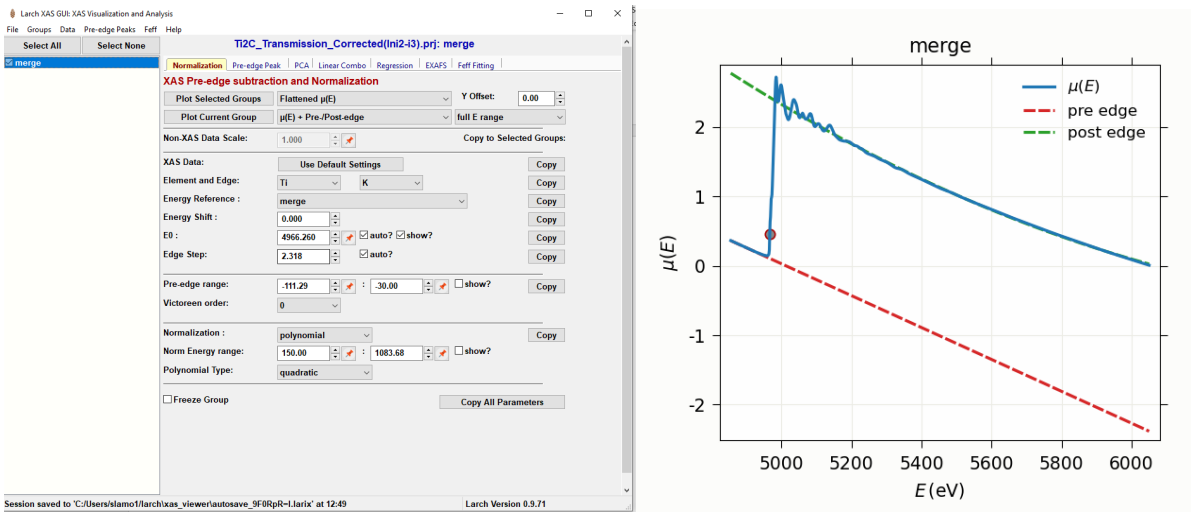


Figure 2 - 2: (Left) Input variables to determine pre-edge and post-edge features for (right) background subtraction in Larch XAS Viewer. Example processing is from Ti_2C EXAFS Data.

Next, I set parameters to subtract the background to Fourier Transform the spectra from momentum space, χ(k), into real space, χ(R). Ideally, we would want a spectrum with high quality data out to large energies (or momenta). Thus, I first amplified the signal of k by weighting the spectra by k^2 or k^3 depending on the signal to noise ratio. By tuning the variables systematically, one can qualitatively observe their effects on the background subtraction and real-space transformation in real time. As a rule of thumb, one should avoid subtracting important high-energy oscillations. This is done by tuning the “k min” variable and adjusting the R bkg value as close to 1 as possible without introducing low R value oscillatory artifacts. It is important to note that the background subtraction is approached qualitatively, and all attempts to systematically change variables across experiments should be documented. Again, please review Matthew Newville’s videos on XAFS Analysis for a comprehensive breakdown of analyses[23–26].

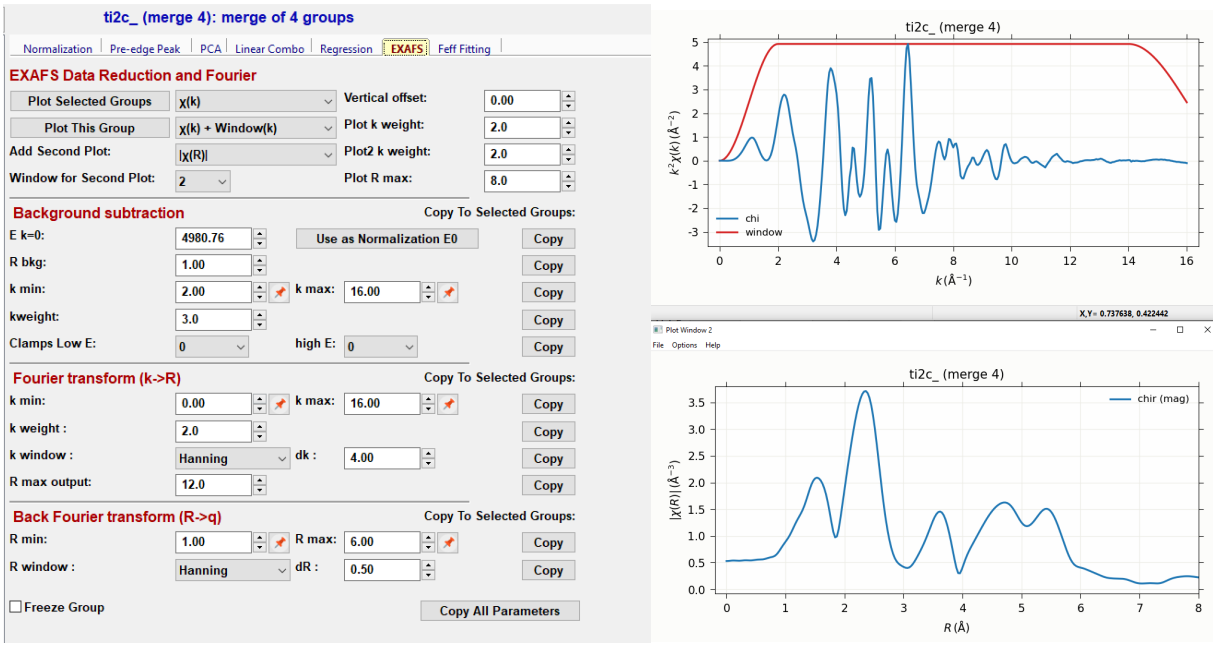


Figure 2 - 3: (Left) Input variables to determine normalization and background subtraction to convert to an accurate modeling of the (right, top) EXAFS spectrum as a function of photoelectron momentum and the (right, bottom) Fourier transform of the function to get the real-space representation of coordination in Larch XAS Viewer. Example processing is from Ti_2C EXAFS Data.

2.2.3.2 FEFF8 Simulation of EXAFS Data

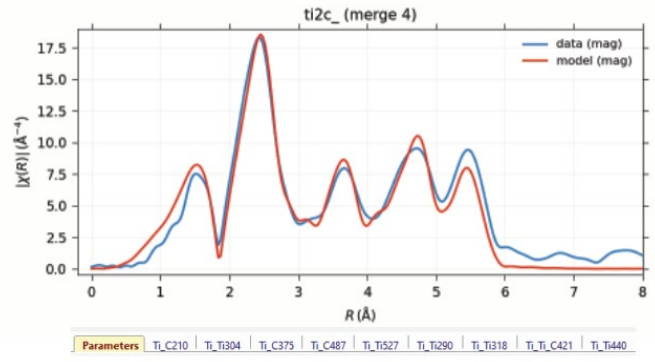
Once the data was resolved using background subtraction, normalization and Fourier Transformation, peaks measured in XAS experiments are able to be assigned to simulated from a calculated structure .CIF file. To do this, we use FEFF8[18,19,24,25] to calculate EXAFS spectra by simulating scattering pathways from a selected absorbing atom with coordinated atoms. FEFF considers spherical wave propagation, multiple scattering pathways, core-hole lifetime effects, energy shifts from self-relaxation, and polarization effects[25]. The parameters we define for the simulation are based on the scattering pathways.

The photoelectron can take many scattering pathways depending on the location and coordination of surrounding atoms. The photoelectron is emitted from a central atom, and can scatter from the closet atom, back to the absorbing atom in a single path, or can scatter off the first shell and interact with a second

shell and finally reflect back to the absorbing atom in a multi-path mechanism. In our case, we only define single or double scattering paths as these result in the highest intensity reflections.

To model the experimental EXAFS data, we use the FEFF8 module in Larch XAS Viewer. First, we use the structure file (.cif) of for a structure that is close to that of the experimental structure. In Larch, we define the absorbing edge (K in our case) and the absorbing atom. After running the calculation, FEFF8 outputs a list of single and multi-scattering paths that can be imported into Larch and fit to the experimental spectrum using the EXAFS equation. I chose single and double scattering pathways that had importance values greater than 50. These "importance values" define the intensity of the backscattered photoelectron.

We fit the model to the data by adding each path to the EXAFS model in succession and setting the fit window to the real-space range that corresponds to the fit parameters. For example, fitting the first peak in Figure 2-4, we set a fit range from 0 Å to 2 Å, and assign only paths that are within that range. After fitting to the full spectrum, we can extract the coordination number and distance when the x^2 is minimized. In the output summary, we then analyze the delr values, showing minimal changes in distances from the expected, modeled atomic positions, to the experimentally refined atomic positions.



Parameter	Best-Fit Value	Standard Error	Info
s02	4.5133994	0.5322962	(init= 5.2131662)
e0	-2.2154791	0.6297635	(init=-4.6957627)
delr_Ti_C421	0.0667781	0.0348693	(init= 1.0000e-3)
delr_Ti608	-0.1252511	0.0122692	(init=-0.1662494)
delr_Ti527	0.1007141	0.0158902	(init= 0.0435289)
delr_Ti440	-0.2899628	0.1151245	(init=-0.0106412)
delr_Ti318	0.2228534	0.0245642	(init= 1.0000e-3)
delr_Ti304	0.1056017	0.0146080	(init= 0.0016410)

Figure 2 - 4: Final output from FEFF8 fit of the Ti_2C Fd3m structure model, fit to the experimental EXAFS data collected at CHESS.

2.3 Synthesis Methods

2.3.1 Synthesis of Y_2C

Synthesis of Y_2C proceeded in a one step high-power tungsten-inert-gas (TIG) welder. High purity yttrium metal was acquired from Sigma Aldrich or STREM suppliers. In either case, oxygen content in the bulk metal was minimized to inhibit the formation of the cubic-Y_2C structure. Pure yttrium metal was arc-welded initially to ablate surface oxide and form a single metal button from sourced chunks, pieces or slivers. As mass loss was expected due to ablation, the metal was moved to an argon atmosphere glovebox where the mass was measured. Using the yttrium mass, graphitic carbon (Sigma Aldrich) was weighed to achieve a molar ratio of 2-parts yttrium to 1-part carbon. The weighed carbon powder was then moved to a 6mm die pellet press set and compressed at 2 tons for 30 seconds under a hydraulic press.

The carbon pellet and yttrium button were moved back to the arc-welder into a copper hearth under argon atmosphere. The atmosphere was purged under vacuum 3 times to remove ambient oxygen, and back-filled with fresh argon. The carbon and yttrium were welded together, flipped and welded again. This process was repeated 6 total times until the carbon was homogenously reacted with the yttrium to form Y_2C. The material was moved back into the glovebox for experimental next steps.

2.3.2 Synthesis and Y_2CF_2

The synthesis of Y_2CF_2 proceeded in a high-temperature, inert atmosphere solid-state reaction. Due to the etching of quartz tubes in contact with metal-fluorides, a tantalum reaction vessel was first created. A 2” long tantalum tube with an inner diameter of 0.30” and an outer diameter of 0.38” were machined. A tantalum cap was welded using a TIG welder onto one end of the tube. The half-sealed tube was then cleaned using an ultrasonic cleaner in isopropyl alcohol and dried in a 100 ^oC oven overnight.

In an argon atmosphere glovebox, YF_3, Y_2C, and graphitic carbon were ground together with a mortar and pestle in a ratio of 2-parts YF_3, 2-parts Y_2C, and 1-part graphitic carbon. The combined powder was then moved to a 6mm die pellet press set and compressed at 2 tons for 30 seconds under a hydraulic press. The pellet was placed into the half-sealed tantalum tube. The half-sealed tube with the reaction pellet was then moved from the glovebox into the arc-welder, purged 3 times with vacuum and argon, and fully sealed to hold the reaction pellet.

The sealed tube was moved back into the glovebox and placed in a clean and dried quartz tube. The quartz tube was sealed at the bottom and wriggled into vacuum tubing clamped with a hose clamp to a vacuum valve. With the valve closed to oxygen, the quartz tube was moved to a hydrogen-oxygen torch, and the top was sealed under slight vacuum. The fully sealed tube was allowed to cool before moving to a tube-furnace. The furnace was programmed to ramp from 25 °C to 1240 °C over 12 hours. The temperature was held at 1240 °C for 100 hours, before ramping to 1200 °C for 48 hours, and cooling down to 25 °C over another 48 hours. The quartz reaction vessel was then moved back into the glovebox, where the Ta tube was extracted. The Ta tube was then opened using a pipe cutter, and the pellet was removed for experimentation.

2.3.3 Synthesis of Np1F Electrolyte Salt

The synthesis of Np1F electrolyte salt is adapted from Davis et al.[27,28]. N,N,N-trimethyl-neopentyl-ammonium iodide (Np1I) was synthesized in a fume hood using standard personal protective equipment (lab coat, goggles, face mask, and Viton gloves rated for use with methyl iodide). First, 20 g of K_2CO_3 was incrementally added to 80 mL of absolute ethanol in a 500 mL round-bottom flask (RBF), allowing each portion of K_2CO_3 to dissolve before introducing the next. Subsequently, 5 mL of neopentylamine was stirred into this mixture for approximately 10 minutes under a tightly capped flask. Methyl iodide (20 g, ~8.77 mL) was then carefully measured and added, and the entire vessel was wrapped in aluminum foil to shield it from light. The reaction was allowed to proceed with continuous stirring for 24 hours, after which the flask was uncapped to enable excess methyl iodide to evaporate. The resulting suspension—containing Np1I, KI, and unreacted K_2CO_3—was filtered via a ceramic filtration funnel under vacuum. Ethanol washings were combined with the filtrate, and this solution was refiltered if necessary to remove residual solids. To recrystallize, the filtrate was placed in a freezer overnight to promote crystal formation. Excess ethanol was decanted, and the partially purified Np1I (co-crystallized with KI) was then dissolved in dichloromethane (DCM). The DCM solution was filtered again, concentrated via rotary evaporation at room temperature, and re-dissolved in a minimal volume of ethanol for a second overnight crystallization in the freezer. Following removal of the remaining solvent by rotary evaporation, the final Np1I product was dried thoroughly and stored in a dark vial wrapped in aluminum foil to prevent decomposition.

To convert Np1I into N,N,N-trimethyl-neopentyl-ammonium hydroxide (Np1OH), the purified iodide salt was dissolved in ~225 mL of deionized water in a foil-wrapped 500 mL RBF equipped with a stir bar. Silver(I) oxide (1.5 equiv.) was slowly introduced through a funnel while stirring was maintained at a moderate speed. The mixture turned dark brown as the reaction proceeded over 24 hours. Excess solid AgI and unreacted Ag_2O were removed by vacuum filtration, and the filtrate was passed through a 0.45 µm PVDF syringe filter to eliminate any remaining silver-containing particulates. The resulting clear, slightly viscous solution was collected as the Np1OH product.

Finally, N,N,N-trimethyl-neopentyl-ammonium fluoride (Np1F) was prepared by titrating the Np1OH solution with hydrofluoric acid (HF). Because HF is highly toxic and can etch glass, this step was conducted in a polyethylene (HDPE) reaction vessel with a Teflon-coated stir bar and under strict HF safety protocols, including the use of HF-resistant gloves (distinct from those used with methyl iodide), a specialized HF-compatible pH meter, and secondary containment with a basic calcium salt solution to neutralize spills. After determining the concentrations of both HF and Np1OH through preliminary titrations, a measured volume of water sufficient to submerge the pH electrode tip, around 150mL, was placed in the HDPE vessel, and the HF was cautiously pipetted into the water. The Np1OH solution was then added from an elevated separatory funnel at a controlled rate. Near the equivalence point, the addition was slowed to dropwise increments, as each drop caused a marked shift in pH. Upon reaching neutrality, the neutralized Np1F solution was concentrated in a large RBF using a rotary evaporator at room temperature, transferred to a custom Schlenk flask, and dried on the Schlenk line at 100 °C under full vacuum overnight. The completely dried Np1F salt was collected and stored in a suitable container, again wrapped in aluminum foil and handled under dry conditions to prevent contamination and degradation.

2.3.4 Fabrication of Liquid State Electrochemical Cells

Electrodes were fabricated following a consistent procedure. First, layered Y_2C powder was coarsely ground by hand in a mortar and pestle until visually homogeneous (black, shiny particles indicating minimal oxidation). The powder was then transferred to a stainless-steel jar and ball-milled for approximately 12–15 minutes to further reduce particle size, typically yielding 130–165 mg of Y_2C. Next, Y_2C (80 wt%), Super P (10 wt%), and PVDF (10 wt%) were combined. To facilitate dispersion of the PVDF,

the PVDF was dissolved separately in propylene carbonate, then added to the Y_2C–Super P mixture while grinding in a mortar and pestle to form a slurry at approximately 34% solids.

A 0.025 mm Ta foil served as the current collector and was affixed onto a ceramic tile with 3 mil (0.0762 mm) Scotch tape as a spacer or doctor blade guard rail. The exposed Ta surface was lightly abraded to improve adhesion, then cleaned with isopropanol. The Y_2C slurry was applied to the Ta foil using a metal blade until a uniform coating was achieved with no visible foil. The coated foil was immediately placed under vacuum in a glovebox. The drying temperature was ramped from 20 °C to 120 °C—typically at a rate of about 30 °C every 30 minutes—and held at 120 °C for 15–20 hours to ensure complete solvent removal. Finally, electrodes were punched into 15 mm diameter discs and stored in an inert environment until use, exhibiting minimal warping and consistent film uniformity.

Electrochemical measurements were conducted in a custom-built Teflon cell (1 in × 1.5 in × 1.5 in) milled from a single block. A 15 mm through-hole allows for electrolyte contact on both the working (WE) and counter electrode (CE) sides, and a 0.9 mm deep trench (15.6 mm diameter) on each side houses 15.6 mm diameter viton O-rings (1.70 mm thick) to seal each electrode compartment. A separate 9.15 mm diameter port was machined in the top of the cell to accommodate the reference electrode (RE). A 15.6 mm diameter, 0.25 mm thick platinum disc served as the CE.

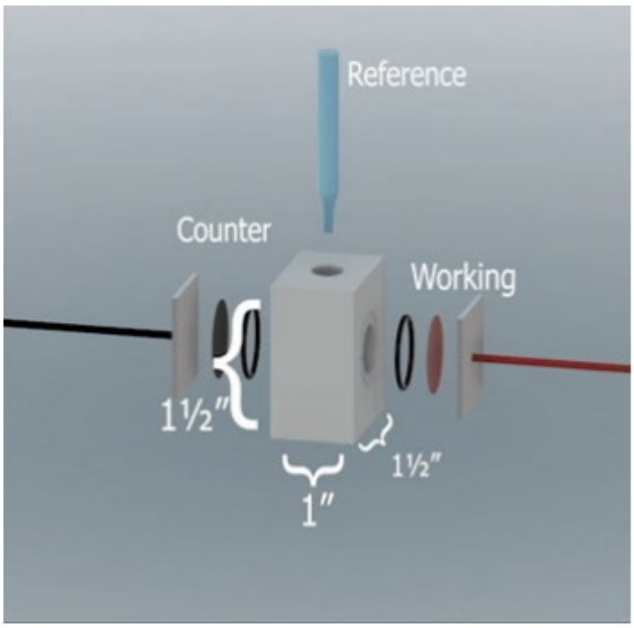


Figure 2 - 5: Custom electrochemical cell milled from a block of Teflon. In this case, the counter electrode is made from a 15mm Pt disk, and the working electrode is made from Y_2C/C/PVDF cast on a Ta foil disk.

The reference electrode was prepared by dissolving 44 mg of Ag triflate in 25 g of MPPY-TFSI to create a 0.01 M Ag/Ag^+ ionic liquid solution. This solution was kept wrapped in aluminum foil to prevent light-induced nucleation of silver nanoparticles. A porous glass frit (Gamry Porous Glass Tips) was attached to the end of a glass reference compartment using shrink-wrap Teflon tubing. Approximately 2 mL of the ionic liquid electrolyte was added to the reference compartment, ensuring no air bubbles remained near the frit. A clean, 3 in silver wire was then immersed in the solution to provide electrical contact to the potentiostat. All cell components were assembled in an inert atmosphere, and the resulting sealed cell configuration allowed for controlled electrochemical fluorination and characterization experiments.

An electrolyte solution consisting of dry, distilled, and degassed BTFE and Np1F salt was mixed on a stir plate in a clean scintillation vial. A 0.75 M solution was mixed with a stir bar. To fill the Teflon electrochemical cell, 3.5mL of BTFE was mixed with 156mg of Np1F. The solution was stirred until all salt dissolved, approximately 15 minutes. Using a micropipette, the solution was moved to the electrochemical cell before electrochemical experiments were conducted.

2.3.5 Fabrication of Solid-State Electrochemical Cells

Y_2C was hand ground into a powder using an agate mortar and pestle. The mass of the powder was weighed with an appropriate amount of electron conductive additive (Cu powder) and ion conductive additive ($Ca_{0.5}Ba_{0.5}F_2$)[29]. For the composite electrodes containing the $Ca_{0.5}Ba_{0.5}F_2$ (CBF) ion conductive additive, a weight ratio of 1.5 parts Y_2C to 1.5 parts Cu to 1 part CBF was used.

Full electrochemical cells were pressed with 200 mg of electrolyte (CBF) sandwiched between 5±0.05 mg of working composite electrode and 20 mg of $Pb/PbF_2/C$ as the counter electrode. Using a voltmeter, a standard voltage difference between $Pb/PbF_2/C$ and Y_2C of ~2.0 V--2.4 V was measured to confirm coverage of both sides of the pellet cell. A resistance of less than 1 Ohm was measured across the surface of the Y_2C composite to confirm electronic percolation across the working electrode. The pellet was then placed in a high-temperature electrochemical cell[30,31], which was helium-leak tested to ensure the quality of the inert atmosphere for testing.

The electrochemical cell was attached to a heating set-up, and a brass heating band was warmed to either 170°C or 200°C. During this time, the open-circuit potential was collected over one hour. Discharge was tested at a C-rate between 1/50 and a C-rate of 1/10 and tracked via a Biologic VMP-300 potentiostat or a Neware BTS battery tester.

2.3.6 Synthesis of Amorphous Y_2CF_2

We found that, with the previous hand grinding procedure, the interfacial resistance (impedance) increased as Y_2C was fluorinated to Y_2CF_2. We hypothesized that this was the result of two processes: a large particle size led to 1) low surface area contact with the electrolyte (CBF), resulting in poor fluoride transport between the electrode material and the electrolyte, and 2) the formation of a thick, nonconductive layer of Y_2CF_2 at the interface between Y_2C and the electrolyte, resulting in slow diffusion within the interphase between the active Y_2C and the electrolyte layer.

We therefore suspected that ball milling Y_2C in composite form could improve performance by increasing the contact area of both the electrolyte additive and Y_2C as well as decreasing the particle size

to avoid passivation with thick fluorinated layers. Previous reports have shown that ball milling Y_2C with CBF directly for 10 hours at 250 rpm caused degradation reactions[32]. Therefore, we opted to ball mill Y_2C with Cu powder (1 part Y_2C/1 part Cu by weight) to first aggressively decrease the size of the particles before ball milling CBF with the Y_2C/Cu composite for 2 h at 200 rpm. Ball milling was performed in a 50 mL ZrO_2 ball mill jar with 10 mm ZrO_2 balls. For composite electrodes containing a CBF ion conductive additive, a weight ratio of 3 parts Y_2C/Cu composite to 1 part CBF was used to achieve ion percolation.

As ball milling proceeded from 2 h at 250 rpm to 10 h at 250 rpm, the width of the XRD peaks increased. This suggests that the material's crystallite size decreases as the lattice strain increases, leading to a structure with decreased long-range ordering.

Full electrochemical cells were pressed with 200 mg of electrolyte (CBF) sandwiched between 5±0.05 mg of working composite electrode and 20 mg of Pb/PbF_2/C as the counter electrode. Using a voltmeter, a standard voltage difference between Pb/PbF_2/C and Y_2C of ~2.0 V--2.4 V was measured to confirm coverage of both sides of the pellet cell. A resistance of less than 1 Ohm was measured across the surface of the Y_2C composite to confirm electronic percolation across the working electrode. The pellet was then placed in a high-temperature electrochemical cell for testing.

Upon discharge, we find that there is no perceivable crystalline structure associated with the expected intercalated phase, Y_2CF_2, which was found to crystallize in the $P\bar{3}m1$ space group[32]. This result is fundamentally novel compared with the previously reported behavior of Y_2C/Y_2CF_2 electrode X-ray diffraction, suggesting that the expected intercalated phase is distorted to the degree to which no ordered phase is observable. Therefore, upon full discharge to 282 mAh/g, a new material with an approximate composition of Y_2CF_2 (yttrium subcarbide fluoride) has been discovered.

2.3.7 Synthesis of metal doped Y_2CF_2

The synthesis of Calcium doped Y_2CF_2 is adapted from Druffel at alias' synthesis of Y_2CF_2[33]. First, Y_2C was synthesized by first arc-welding yttrium metal (Alfa Aesar, ~40mesh powder, 99.6% (REO)) with graphitic carbon (Sigma-Aldrich). Metal doped Y_2CF_2 was then synthesized by the solid-state reaction of YF_3, Y_2C, graphite (Sigma-Aldrich), and MF_2 (M = Ca, Sr, Strem). The reagents were ground into a fine

powder in a stoichiometric ratio and pressed into a pellet under ~0.56 GPa of pressure using a hydraulic press. See Table 2-X for an example on how dopants were produced in a stoichiometric ratio. The pellet was welded inside an ampule made of tantalum (Ta)metal. To fashion an ampule, a Ta cap was hammered into Ta tubing and sealed in argon by welding the cap and tubing together with an electric arc. The Ta tubing, 99.95% Ta seamless tubing, was purchased from Eagle Alloys in a 1 cm diameter and cut to 5 cm lengths. The caps were made of the same Ta. After welding the reagents inside a Ta ampule, the Ta ampule was sealed in a fused quartz ampule under 1 mbar Ar. Then the vessel was placed in a tube furnace and heated to 1513 K at a ramp rate of 10 K/min. The temperature was held at 1513 K for 3 days, then cooled to 1273 K over 10 h, then to 1073 K over 5 h, and to room temperature over 5 h. The ampule was then brought into the glovebox and opened with a pipe cutter. The pellet remained intact through the reaction.

Table 2 - 1: Function for calculating the ideal ratio of atoms to produce materials with a goal doping percentage. Doping percentage is the percentage of yttrium sites occupied by a dopant.

Species	3% Doped Synthesis	6% Doped Synthesis
Yttrium	35	34
Calcium	1	2
Carbon	18	18
Fluorine	35	34
% yttrium sites occupied (Ca/Y)	2.8%	5.9%

Table 1 used as a base for multiplying the stoichiometric ratio of precursors in order to get the right molar ratio of atoms for systematic increases in the concentration of dopant.

Table 2 - 2: (Left) Function for determining the moles of elements per molecular formula. This is used to calculate the total moles of precursor needed to produce the goal doping percentage (right).

Species	CaF_2	Y_2C	Carbon	YF_3
Y	0	2	0	1
Ca	1	0	0	0
C	0	1	1	0
F	2	0	0	3

Molar Mutliplier	CaF_2 x2	Y_2C x12	Carbon x6	YF_3 x10	TOTAL
Y	0	24	0	10	34
Ca	2	0	0	0	2
C	0	12	6	0	18
F	4	0	0	30	34
(Ca/Y)					5.9%

Table 2 - 3: Function for converting the moles of precursors to the mass percentage of precursor for synthesis.

	CaF_2	Y_2C	Carbon	YF_3
Moles	2	12	6	10
Molecular Weight	78.07 g/mol	189.8 g/mol	12.011 g/mol	145.90 g/mol
Grams (m * mw)	156.1 g	2277.6 g	72.1 g	1459.0
% mass	4%	57%	2%	37%

2.3.8 Synthesis of Sulfur Coating on Electrides

2.3.8.1 Liquid Y_2C Reaction

The surface of the Y_2C electride is extremely reactive. The high energy electrons are so reactive, that exposing chunks of Y_2C to an inert-atmosphere glove-box with <0.1 atm of O_2 can still cause oxide signal measurable by XPS. Thus, we developed a liquid-deposition technique to surface coat Y_2C in a reactive substrate to in-situ fabricate passivating interphases.

In these experiments, we either deposited aluminum via a reduction of trimethylaluminum or sulfur via reduction of elemental sulfur. Both reactions took place in toluene, which was dried overnight using calcium hydroxide.

First, we took Y_2C post-arc welding synthesis into the glove-box where it is broken into small chunks around 200mg in mass, at around 2mm in diameter. To a mortar and pestler, we added propylene carbonate (PC) ~10mL. This was enough liquid to cover the small chunk of Y_2C. To this PC, we dropwise added a 1M solution of trimethylaluminum (TMA) in toluene. We used a hammer to very lightly tap the end of the pestle as to cleave the chunk in two. This exposed a fresh surface of Y_2C to the TMA solution, reducing the solution at the surface. We varied the time exposed to the reactive liquid to understand the effect of time on surface coating composition. Unfortunately, XPS showed hydrocarbons on the surface, but no aluminum.

For a liquid sulfur reaction, we dissolved 1M bulk sulfur in toluene overnight. Sulfur was identified as an ideal reactant to form a stable SEI because the ionic radii of sulfur is larger than oxygen, decreasing the likelihood of sulfur mediated degradation through an intercalation mechanism. Furthermore, sulfur is soluble in toluene, providing an ideal vehicle to Y_2C cleavage under liquid. Finally, bulk sulfur consists of a single element system, providing an ideal system for modeling. The reaction between Y_2C and sulfur continued as above, with a small chunk of Y_2C sitting in the 1M sulfur in toluene solution. The Y_2C was cleaved in solution by hitting the pestle lightly with the hammer. We varied exposure time to measure the rate of sulfur deposition on the surface of Y_2C using XPS. We found that at 2 minutes, a coating grew that was thick enough to passivate the surface to oxygen. We measured signals corresponding to a heavily reduced carbide peak and a Y^{2+}, consistent with reports of electrides and MXenes[34–38].

2.3.8.2 Solid Vapor Phase Reaction

Y_2C was first ground into a fine powder using a mortar and pestle. The Y_2C was moved into the bottom of a 15mL Swagelok high temperature reaction vessel constructed of 316L stainless steel parts. Pure sulfur (Sigma) was placed into the end of a borosilicate glass centrifuge tube. This tube was cut to about 2 cm in length in order to fit into the barrel of the reaction vessel. The elemental sulfur in the glass tube was placed over the Y_2C powder. Then, the end cap of the Swagelok cell was screwed into place and

tightened using a wrench. The reaction vessel was then placed in a furnace, careful not to invert or spill the sulfur, at elevated temperatures until reaction was complete.

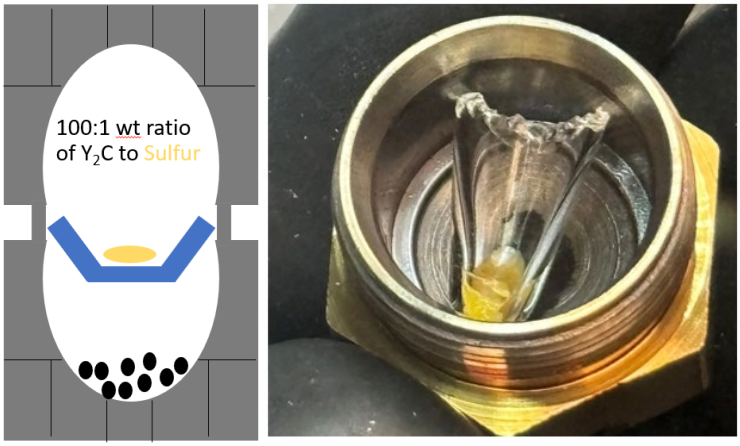


Figure 2 - 6: Stainless steel reaction vessel used to deposit vaporous sulfur on the surface of Y_2C. The glass container is a centrifuge tube cut to fit into the stainless steel Swagelok reactor.

2.4.1 X-ray Diffraction

X-ray diffraction (XRD) is an analytical method to determine the arrangement of atoms within a crystal lattice in 3 dimensions. In this method, x-rays at a specific wavelength, λ, are directed at a sample with a given incident angle, θ, and scatter off planes of electrons that sit on atoms within the crystal. These planes are separated by a constant distance, d, from each other. Bragg proposed that reflected wave will interact constructively given the reflection is in-phase with the incident wave:

$$n\lambda = 2dsin\theta$$

This constructive interference condition at a given angle for diffraction planes results in intensity peaks that can be detected. By varying the incident angle, one can map the angles that result in constructive interference, resulting in an intensity profile that corresponds to the distance of atomic planes of a crystal at a certain orientation. For a detailed analysis of XRD theory, please read the dissertations of Dr. Dan Druffel and section 2.3.1 and Dr. Lauren McRae section 2.4.1.

In powder x-ray diffraction (PXRD), a crystal is ground into a very fine powder. Ideally, the powder will have an infinite number of orientations normal to the sample holder. Thus, diffraction from these samples across all measured incident angles will result in peaks that correspond to all families of planes.

If chemical powders are not taken directly from a vendor, I used a mortar and pestle to grind large particle materials into powders with particle sizes ~1-10 μm in diameter. These powders were then transferred to a quartz XRD sample holder slide. In order to mitigate effects of oxidation, I placed a 1.5" width piece of 1-sided Kapton tape over the sample on the quartz slide. To transfer air-sensitive samples to the XRD instrument, I sealed the sample holders in a HDPE bag heat-sealed under Ar atmosphere.

All measurements at UNC-Chapel Hill were run in a Rigaku Smartlab diffractometer. Furthermore, I used a Bragg-Brentano geometry across a range of 20−90° 2-theta using Cu Kα (λ= 1.54056 Å)[39]. In the Bragg-Brentano geometry, the sample is set at a fixed radius from the x-ray beam and x-ray detector. The sample orientation is fixed, while a goniometer rotates both the incident beam and detector arms. Resolution of the measurement was set by fixing the step distance of the measurement angle, while varying the time at which the measurement would record data at that angle. This increased the signal to noise ratio by increasing the measured counts at a given angle.

The measured samples were then indexed and refined using the PDXL software from Rigaku. In crystalline samples, the background was first subtracted from the signal by manual subtraction. Peaks were then indexed using the known composition of the measured materials and cross-checking against the ICSD crystal materials database[40]. In cases where the material was unindexed (i.e. Y_2CF_2), crystal structure geometries optimized in DFT were converted to .CIF files and used to index material peaks.

Using identified structures to match all identified diffraction peaks, one can optimize peak fits with given material properties and measurement parameters. Intrinsically, the width of a diffraction peak is a function of domain size, crystal lattice strain, and lattice defects [Cite, McRae]. Extrinsically, detector geometry and inhomogeneity in wavelengths also effect peak broadening [cite, McRae]. Peak height is a function of the intensity of the reflection. Intrinsically, this is affected by the charge density around the atoms, and the concentration of the diffraction plane per unit volume. In layered Van-der-Waal materials such as Y_2C, Ca_2N, and graphite, materials preferentially break along the Z direction due to the high density of

atoms in this direction[41]. This is known as the cleavage plane, and layered materials have a high density of microparticles that preferentially texture on surfaces along these planes[41]. Thus, when measuring diffraction, layered materials tend to have high intensities along the *00l* family of planes. When fitting patterns, the texturing effect must be taken into account.

Once peaks are identified and fit according to instrument and material properties, component analysis can be used to identify the mass ratios of each chemical to each other[42].

2.4.2 X-ray Absorption Spectroscopy

2.4.2.1 XAS Sample Preparation

Samples were prepared according to guidelines outlined by the Cornell High Energy Synchrotron Source staff. Aluminum sample holders were sent from Cornell. These sample holders were machined to an 8mm width x 10mm length x 1mm thick aluminum sheet, with a 3mm diameter hole milled in the center.

Samples for X-ray absorption spectroscopy (XAS), including transmission, fluorescence, and high-energy resolution fluorescence detection (HERFD) experiments, must be adequately diluted to avoid spectral distortions caused by overly concentrated materials[43]. Neat samples typically require dilution using a low-absorption diluent such as boron nitride (BN) or graphite (C).

To establish appropriate dilution levels, the sample attenuation length must first be determined. The calculation requires the chemical formula, material density, and absorption cross sections (σ) of each element at energies just above the absorption edge of interest. Cross-section data are available online (e.g., http://www.csrri.iit.edu/periodic-table.html).

Using Y_2C as a representative example, at the Y K-edge (17080 eV), the density is around 4.54 g/cm³, according to the materials project, and cross sections at 17080 eV are:

- σ(Y) = 101.1 cm²/g
- σ(C) = 0.315 cm²/g

The total absorption cross section (σ) is calculated in Excel by adding together the individual cross-section:

$$\sigma(\mathrm{Y_2C}) = 101.1\frac{cm^2}{g} x\ mass\ \%\ of\ yttrium + 0.315\frac{cm^2}{g} x\ mass\ \%\ of\ carbon$$

resulting in σ = 94.72 cm²/g. Multiplying σ by the density provides the linear absorption coefficient (μ):

$$\mu(17080) = 94.72\frac{cm^2}{g}\ x\ 4.54\frac{g}{cm^3} = 430.05\ cm^{-1}$$

The required thickness (path length) for μ = 1 is thus:

$$\text{Path Length} = \frac{1}{\mu} = \frac{1}{430.05 cm^{-1}}\ x\ 10{,}000 = 23.25\mu\text{m diameter particles}$$

This indicates the necessity of fine particle sizes, generally smaller than ~25 μm, to ensure accurate data collection. This can be achieved simply by grinding Y_2C powder in a mortar and pestle for about 5 minutes.

The required dilution for samples placed in 1 mm thick cells was calculated using the MUCAL tool (https://www-ssrl.slac.stanford.edu/smbin/mucalwebnew.pl). This tool calculates X-ray absorption cross sections [http://ixs.csrri.iit.edu/database/programs/mcmaster.html] and is based on empirical models by McMaster et al.[44] and Krause[45].

Input parameters include a total mass of 40 mg diluted sample and an area of 0.31 cm², the dimensions for PIPOXS sample holder cells. The calculated optimal dilution ratio to achieve μ(E) = 2 for Y_2C is:

- 6.2 mg Y_2C : 33.8 mg BN

Maintaining this weight ratio allows scaling up the amounts as needed, and provides higher accuracy mass measurements for highly diluted sample with large atomic numbers and densities.

Samples prepared in aluminum cells were sealed using Kapton tape and had to meet specific criteria to ensure high-quality data collection. These criteria included fine, uniform powders with particle sizes ideally around 10 μm or smaller, complete and uniform filling of the cell window, and maintaining clean and properly sealed cell sides and faces.

First, a flat piece of Kapton tape was affixed to a flat working surface with the sticky side facing upwards, secured by Scotch tape. The aluminum cell was then placed flat onto this Kapton tape. Any

exposed adhesive surfaces were subsequently covered with Scotch tape, except for the area of the cell window. The edges of the sample cell were protected with Scotch tape, leaving tabs to facilitate easy removal.

Next, calculated amounts of the sample and boron nitride (BN) were ground together thoroughly to ensure uniformity and an appropriate particle size distribution. The cell window was then filled with the ground powder, forming a slight mound. This powder mound was compressed into a flat, parallel surface using a spatula, applying steady, even pressure.

The protective Scotch tapes were carefully removed in reverse order of application to maintain a clean cell face. Another layer of Kapton tape was applied over the cell window to seal the powder securely, taking care to avoid any wrinkles or creases. The sealed sample was labeled clearly using a fine-tipped marker. Finally, any excess tape was carefully trimmed away to ensure the cell could be easily mounted during subsequent experiments. For transport, samples were bagged in 3 layers of heat-sealed HDPE bags under Argon atmosphere.

XAS measurements were conducted at the Photon in, Photon out X-ray Source at Cornell's High Energy Synchrotron Source. High energy resolution fluorescence detected XAS of the yttrium K-edge was collected after calibrating the yttrium signal to yttrium foil. XANES measurements were collected. For XANES, measurements were recorded between 16900eV and 17550eV. For EXAFS, data was collected between 16900eV and 18080eV. To increase the signal to noise of detected samples, multiple runs were conducted, especially for EXAFS scans.

REFERENCES

1. Kresse, G. & Furthmü, J. *Efficient Iterative Schemes for Ab Initio Total-Energy Calculations Using a Plane-Wave Basis Set*. (1996).

2. Bartók, A. P. & Yates, J. R. Regularized SCAN functional. *J Chem Phys* 150, 161101 (2019).

3. Ong, S. P. *et al.* Python Materials Genomics (pymatgen): A robust, open-source python library for materials analysis. *Comput Mater Sci* 68, 314–319 (2013).

4. Singh, J., Lamberti, C. & van Bokhoven, J. A. Advanced X-ray absorption and emission spectroscopy: in situ catalytic studies. *Chem Soc Rev* 39, 4754–4766 (2010).

5. Bauer, M. HERFD-XAS and valence-to-core-XES: New tools to push the limits in research with hard X-rays? *Physical Chemistry Chemical Physics* 16, 13827–13837 (2014).

6. van Bokhoven, J. A. *et al.* Activation of Oxygen on Gold/Alumina Catalysts: In Situ High-Energy-Resolution Fluorescence and Time-Resolved X-ray Spectroscopy. *Angewandte Chemie International Edition* 45, 4651–4654 (2006).

7. Ghigna, P. *et al.* Lithiation Mechanism in High-Entropy Oxides as Anode Materials for Li-Ion Batteries: An Operando XAS Study. *ACS Appl Mater Interfaces* 12, 50344–50354 (2020).

8. Radu, D. *et al.* Geometric and electronic structure of α-oxygen sites in Mn-ZSM-5 zeolites. *Journal of Physical Chemistry C* 112, 12409–12416 (2008).

9. Vorwerk, C., Aurich, B., Cocchi, C. & Draxl, C. Bethe-Salpeter equation for absorption and scattering spectroscopy: Implementation in the exciting code. *Electronic Structure* 1, (2019).

10. Gulans, A. *et al.* exciting: a full-potential all-electron package implementing density-functional theory and many-body perturbation theory. *Journal of Physics: Condensed Matter* 26, 363202 (2014).

11. Aipatova, N. M., Zabusova, S. E. & Tomilov, A. P. *The Reduction of Organic Compounds by Solvated Electrons Generated Electrochemically*. *Translated from Uspekhi Khimii* vol. 55 (1986).

12. Krukau, A. V, Vydrov, O. A., Izmaylov, A. F. & Scuseria, G. E. Influence of the exchange screening parameter on the performance of screened hybrid functionals. *J Chem Phys* 125, 224106 (2006).

13. Carbone, M. R. *et al.* Lightshow: a Python package for generating computational x-ray absorption spectroscopy input files. (2022).

14. Zeegers, S. T., Costantini, E., De Vries, C. P. & Tielens, A. G. G. M. *Investigating Dense Interstellar Environments in the X-Rays PoS(LCDU 2013)065*. http://pos.sissa.it/ (2013).

15. Marusak, R. A. Physical Methods in Bioinorganic Chemistry: Spectroscopy and Magnetism (ed. Que, Lawrence Jr.). *J Chem Educ* 77, 1413 (2000).

16. Kroneck, P. M. H. *et al.* Multifrequency EPR evidence for a bimetallic center at the CuA site in cytochrome c oxidase. *FEBS Lett* 268, 274–276 (1990).

17. Farrar, J. A., Lappalainen, P., Zumft, W. G., Saraste, M. & Thomson, A. J. Spectroscopic and Mutagenesis Studies on the CuA Centre from The Cytochrome-c Oxidase Complex of Paracoccus Denitrificans. *Eur J Biochem* 232, 294–303 (1995).

18. Rehr, J. J. & Albers, R. C. Theoretical approaches to x-ray absorption fine structure. *Rev Mod Phys* 72, 621–654 (2000).

19. Rehr, J. J. *et al.* Ab initio theory and calculations of X-ray spectra. *C R Phys* 10, 548–559 (2009).

20. Ashley, C. A. & Doniach, S. Theory of extended x-ray absorption edge fine structure (EXAFS) in crystalline solids. *Phys Rev B* 11, 1279–1288 (1975).

21. Wong, R. & Alamillo, J. EXAFS-Theory. *LibreTexts Chemistry* 1867–1867 (2023).

22. Ravel, B. & Newville, M. ATHENA, ARTEMIS, HEPHAESTUS: Data analysis for X-ray absorption spectroscopy using IFEFFIT. in *Journal of Synchrotron Radiation* vol. 12 537–541 (2005).

23. Newville, M. *Larch for XAFS Analysis: 6 Fourier Transforms*. (YouTube, United States, 2021).

24. Newville, M. *Larch for XAFS Analysis 8: Running Feff to Calculate EXAFS Contributions*. (YouTube, United States, 2021).

25. Newville, M. *Larch for XAFS Analysis Using Feff and Feffit @ XAFS2021*. (2021).

26. Newville, M. *EXAFS Analysis with Feff, Larch, Artemis*. https://tinyurl.com/Larch2018 (2018).

27. Davis, V. K. *et al.* Fluoride-ion solvation in non-aqueous electrolyte solutions. *Mater Chem Front* 3, 2721–2727 (2019).

28. Davis, V. K. *et al.* Room-temperature cycling of metal fluoride electrodes: Liquid electrolytes for high-energy fluoride ion cells. *Science (1979)* 362, 1144–1148 (2018).

29. Düvel, A., Ruprecht, B., Heitjans, P. & Wilkening, M. Mixed Alkaline-Earth Effect in the Metastable Anion Conductor Ba1–xCaxF2 (0 ≤ x ≤ 1): Correlating Long-Range Ion Transport with Local Structures Revealed by Ultrafast 19F MAS NMR. *Journal of Physical Chemistry C* 115, 23784–23789 (2011).

30. Nowroozi, M. A., Wissel, K., Rohrer, J., Munnangi, A. R. & Clemens, O. LaSrMnO4: Reversible Electrochemical Intercalation of Fluoride Ions in the Context of Fluoride Ion Batteries. *Chemistry of Materials* 29, 3441–3453 (2017).

31. Nowroozi, M. A. *et al.* Fluoride ion batteries - past, present, and future. *Journal of Materials Chemistry A* vol. 9 5980–6012 Preprint at https://doi.org/10.1039/d0ta11656d (2021).

32. Tojigamori, T. *et al.* Fluorination/Defluorination Behavior of Y2C in Fluoride-Ion Battery Anodes. *ACS Appl Energy Mater* 7, 1100–1108 (2024).

33. Druffel, D. L. *et al.* Synthesis and Electronic Structure of a 3D Crystalline Stack of MXene-Like Sheets. *Chemistry of Materials* 31, 9788–9796 (2019).

34. McRae, L. M. *et al.* Sc2C, a 2D Semiconducting Electride. *J Am Chem Soc* 144, 10862–10869 (2022).

35. Persson, I. *et al.* On the organization and thermal behavior of functional groups on Ti3C2 MXene surfaces in vacuum. *2d Mater* 5, (2018).

36. Harris, K. J., Bugnet, M., Naguib, M., Barsoum, M. W. & Goward, G. R. Direct Measurement of Surface Termination Groups and Their Connectivity in the 2D MXene V2CTx Using NMR Spectroscopy. *The Journal of Physical Chemistry C* 119, 13713–13720 (2015).

37. Schultz, T. *et al.* Surface Termination Dependent Work Function and Electronic Properties of Ti3C2Tx MXene. *Chemistry of Materials* 31, 6590–6597 (2019).

38. VahidMohammadi, A., Rosen, J. & Gogotsi, Y. The world of two-dimensional carbides and nitrides (MXenes). *Science (1979)* 372, eabf1581 (2021).

39. Cockcroft, J. Instrument X-ray Optics I. Reflection Geometry. *School of Crystallography, Birkbeck College, University of London* (2006).

40. Zagorac, D., Muller, H., Ruehl, S., Zagorac, J. & Rehme, S. Recent developments in the Inorganic Crystal Structure Database: Theoretical crystal structure data and related features. *J Appl Crystallogr* 52, 918–925 (2019).

41. Bunge, H. J. *Texture Analysis in Materials Science*. (1982).

42. Rietveld, H. M. A profile refinement method for nuclear and magnetic structures. *J Appl Crystallogr* 2, 65–71 (1969).

43. Bunker, G. *Preparation of XAFS Samples*. (2009).

44. McMaster, W. H., Del Grande, N. K., Mallett, J. H. & Hubbell, J. H. *COMPILATION OF X-RAY CROSS SECTIONS.* https://www.osti.gov/biblio/4794153 (1969).

45. Krause, M. O. Atomic radiative and radiationless yields for K and L shells. *J Phys Chem Ref Data* 8, 307–327 (1979).

46. *Lithium-Ion Batteries*. (PUBLISHED BY IMPERIAL COLLEGE PRESS AND DISTRIBUTED BY WORLD SCIENTIFIC PUBLISHING CO., 2004). doi:doi:10.1142/p291.

This work is based on research conducted at the Center for High-Energy X-ray Sciences (CHEXS), which is supported by the National Science Foundation (BIO, ENG and MPS Directorates) under award DMR-2342336.

CHAPTER 3: ELECTRON-ANION EXCHANGE: EXPERIMENTAL DEMONSTRATION OF A NOVEL INTERCALATION MECHANISM

Connor C. Slamowitz

3.1 Introduction

Recent advances in rechargeable battery materials have supported new markets in grid storage and electric vehicles. Although cation shuttle batteries, such as lithium-ion, are widely used, relatively unexplored anion shuttle batteries could offer alternative functions or improved performance. The fluoride ion battery is uniquely situated for scientific exploration because of the recent discovery of highly conductive liquid electrolytes that contain fluoride[1,2]. To exploit this new electrolyte, we have begun a systematic search for new electrode materials. Recently, we found that yttrium carbide (Y_2C) can be reversibly converted to Y_2CF_2, thereby providing an electrode for fluoride-ion storage with roughly double the capacity of state-of-the-art lithium-ion battery electrodes[3].

Underlying this discovery are many fascinating scientific questions. Y_2C is an electride: a material in which lattice sites contain a bare electron. These electrons do not reside within atomic orbitals and, therefore, the chemical composition can be written as $[Y_2C]^{2+}(2e^-)$. In this material, the electron lattice sites are sandwiched between positively charged yttrium carbide layers (Figure 3-1c). This unusual material—and its electrochemical conversion into Y_2CF_2—provide a fascinating test ground to explore a fundamentally different kind of electron transfer process. Specifically, we predict that the conversion of Y_2C into Y_2CF_2 involves the direct exchange of electrons for fluorides[3]. If this prediction is correct, it would imply that electron transfer is occurring without any associated reduction or oxidation process. This is a new type of electron transfer process and has important implications for energy storage, such as the ability to reduce the activation energy of ion movement. Recently, we have given this process the name electrochemical

electron-anion exchange (EAX). If we can gain additional experimental evidence to support EAX, we will establish redox-less electron transfer as a new kind of electron transfer mechanism.

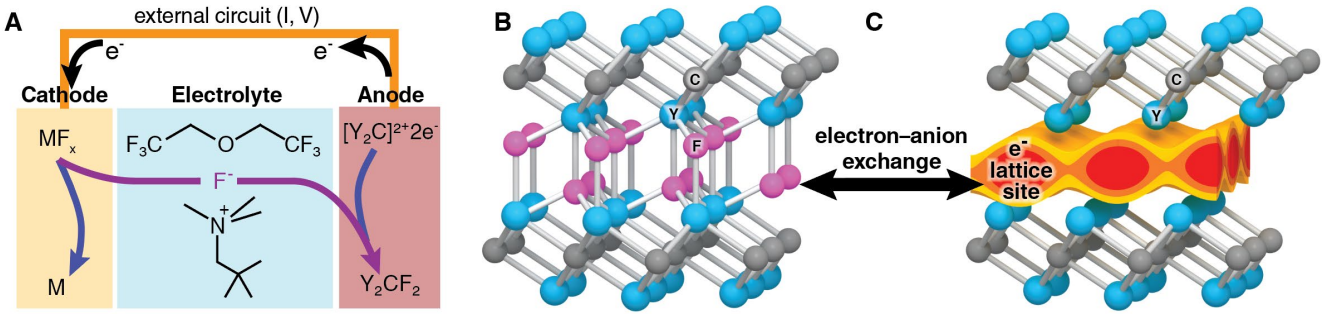


Figure 3 - 1: (a) Concept of electron−anion exchange. The battery configuration incorporates $[Y_2C]^{2+}(2e^-)$ as an anode, an F^- electrolyte, and a cathode (e.g., a metal fluoride).The reversible conversion of (b) Y_2CF_2 to (c) $[Y_2C]^{2+}(2e^-)$ under an applied bias where yellow, orange, and red show isosurfaces of the anionic electrons at the Fermi level.

As atoms lose electrons (oxidation), some screening effects between the core electrons and outer electrons are lost. This causes a shift in the density of the core electrons towards the nucleus, effectively increasing the binding energy of those core electrons to the atom. This effect is reversed in the case of reduction[4]. By spectroscopically probing the energy of the core electrons as they transition from the core, or K-edge, to unoccupied energy bands, the degree of redox can be probed[4–10]. This is the basis of oxidation state analysis using x-ray absorption spectroscopy at the near edge (XANES) for bulk materials, and x-ray photoelectron spectroscopy (XPS) for surface species.

In this study, we measure the slight changes in the binding energies of electrons to the yttrium nucleus as Y_2C fluorinates to Y_2CF_2 using XANES collected at Argonne National Laboratory and Cornell's High Energy Synchrotron. Using these experiments, we calibrate DFT calculations that utilize the Bethe-Salpeter Equation[11–15] to quantify energy shifts of exciton pairs due to Coulombic attraction in the excited state. Using this calibrated DFT, we partitioned the electron localization function (ELF) at zero-flux surfaces between atoms and electrons, integrate the charge density within these regions, and quantify both the electride charge density and valence state of the atoms[16]. Using these advanced quantitative techniques,

we identify a theoretically robust method to experimentally validate electron-anion exchange as a redox-free method of intercalation.

3.2 Methods

3.2.1 XAS

We used the PIPOXS Beamline at the Cornell High Energy X-ray Source (CHEXS) to offer the high-quality data required to confirm redox-less electron transfer in the Y_2C/Y_2CF_2 system. HERFD XAS[4,17] allowed us to record high resolution Y K-edge data from these samples. The HERFD energy resolution improvement is needed because the "standard" XAS absorption edge of yttrium as measured with a Si(111) mono has a broadening of about 6.0 eV, which obscures the changes in edge position that occur on Y oxidation / reduction. Using HERFD and a high resolution monochromator (Si(311) or Si(333) mono), an improvement in resolution of up to 3x is possible over standard XAS[4]. Additionally, the PIPOXS beamline allowed us to perform operando oxidation studies to detect intermediate oxidation states, which may be different from the starting (Y_2C) or ending (Y_2CF_2) compositions.

We performed XANES on well-defined "reference" yttrium-containing compounds that have a single type of yttrium oxidation state. This included as-synthesized Y_2C and Y_2CF_2, which should contain just one oxidation state. We analyzed yttrium metal (Y^0), yttrium oxide (Y^{3+}), yttrium sulfide (Y^{3+}), and yttrium fluoride (Y^{3+}).

3.2.2 Modeling XANES Spectra using the Bethe-Salpeter Equation

The x-ray absorption near edge spectra (XANES) was modeled using a computational pipeline designed for highly accurate simulations of excited states using core-hole attraction modeled by the Bethe-Salpeter Equation implemented by the EXCITING code[18]. First, we performed a structure relaxation of Y_2C and Y_2CF_2 structures using the Vienna Ab-Initio Simulation Package (VASP)[19], implementing the hybrid density HSE06 functional[20]. The plane-wave energy cutoff was 520 eV and a gamma centered k-point grid with a spacing of 0.25 $Å^{-1}$ was used. The output structure was fed into the input generation module created by Lightshow[21], a Python package designed to easily generate spectroscopy input files. We used the yttrium K-edge using default EXCITING parameters.

We then modeled the XAS spectra by first modeling the ground state with the GGA PBE functional with a k-point grid of 6x6x6. The XAS was broadened to a Lorentzian broadening setting of 0.1 to match lifetime broadening effects in experiment. An energy window between 613 eV and 645 eV was used. The output of this script produced 3 spectra polarized on the X, Y, and Z axes. As the XAS measurement was performed on bulk powder, the modeled spectra were averaged together. Finally, the modeled spectra were energy corrected[10,12,13,15] to match the experimental energy shift of Y_2C or Y_2CF_2.

3.2.3 Charge Partitioning of the Electron Localization Function

Structure optimizations were performed using Simmate[22], which automates density functional theory (DFT) calculations performed by VASP DFT calculations used the projector-augmented wave potentials to describe core electrons[23]. For each calculation an initial structural relaxation was performed using the GGA PBEsol functional[24] followed by another structural relaxation and single-point energy calculation using the hybrid density HSE06 functional[20]. The plane-wave energy cutoff was 520 eV and a gamma centered k-point grid with a spacing of 0.25 $Å^{-1}$ was used. These conditions are the exact conditions used to model the XANES spectra in EXCITING. The break condition for the energy in the electronic SC-loop in the relaxation step was dynamically set as 5 x 10^{-5} eV/atom. The DFT-D3 dispersion correction of Grimme with Becke-Johnson damping function was used[25,26]. Voxel densities of 40 voxels/Å along each unit cell edge were rounded to the nearest integer and used for ELF and charge density calculation.

We designed the BadELF algorithm to automatically identify possible electride sites. This was done by searching for ELF maxima that were outside the ELF radius of each atom. Nearest neighbors for each atom were identified using pymatgen's CrystalNN class[27]. The ELF was interpolated along a line between an atom and each of its neighbors. For each interpolation, we measured the distance from the atom to the ELF minimum. This yielded several distances for each atom. The largest of these distances was then used to define the boundary of an atom for the purposes of identifying an electride. This distance should not be confused with the ELF radius, which was the smallest of these distances. Within the unit cell, each atom's boundary was identified using this largest distance. We then searched for ELF maxima that were outside the boundary of all atoms. These ELF maxima were considered as possible electride sites, and we labeled these sites within the crystal structure with a dummy atom (helium). We note, however, that this algorithm

alone is not sufficient to identify a site as being an electride. Additional considerations are that the ELF maxima should generally have a value above 0.5, and that the size of the electride site be similar to a monoatomic anion like hydride or fluoride.

To identify the effective oxidation state of Y_2C and Y_2CF_2, the charge density was first partitioned on the identified ELF minima. The oxidation state was then calculated by first integrating the charge density to get the total charge per atomic volume, and then subtracting the electrons assigned as non-valence electrons.

3.3. Results and Discussion

To explore our proposed mechanism, Druffel et al.[3] employed calculations and experiments in the Y_2C/Y_2CF_2 material system. Using density functional theory (DFT) and the nudged elastic band (NEB) method, they found that the diffusion of fluoride through Y_2C has an activation energy of 196 meV, which is a smaller barrier than lithium in graphite (260 meV)[28] or lithium in CoO_2 (300 meV)[29]. This suggests that the reversible conversion of Y_2C to Y_2CF_2 should occur at room temperature and under electrochemical control.

From these initial calculations, we predict that the electrochemical insertion of F^- into Y_2C to form Y_2CF_2 represents a unique addition to the electrochemical model of intercalation. During discharge, an electron is extracted from the electrode, powering electronic devices, before recombining with the cathode. By integrating the charge density around the yttrium and carbon during the intercalation process (coupled to discharge), Druffel predicted that the oxidation states of Y (+1.91) and C (-2.06) in Y_2CF_2 are nearly identical to those in Y_2C (+1.95 and -2.10, respectively). This calculation showed, preliminarily, that this process of ion movement (and the associated electron transfer) occurs effectively without reduction or oxidation (Figure 3-2) of the atoms within the host materials. Instead, the electron is extracted from the electride electron site.

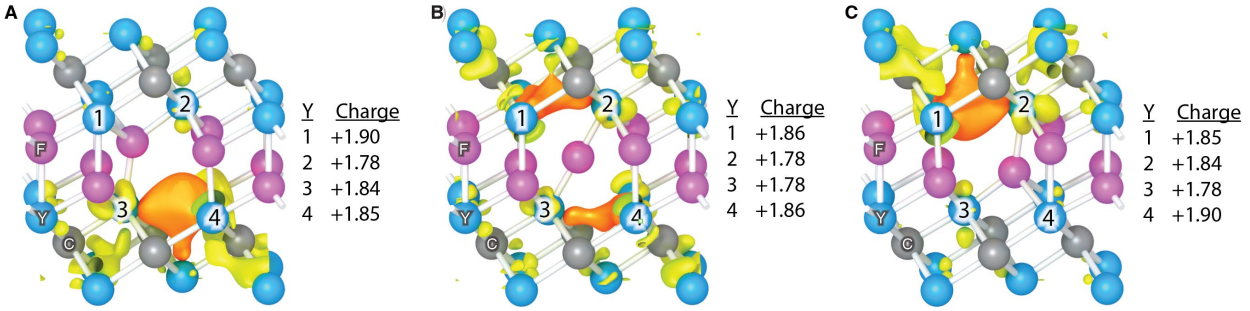


Figure 3 - 2: Electron density isosurfaces near the Fermi level. (A) The ground state of Y_2CF_2 with one F vacancy showing a F^- (purple) and an anionic electron(orange) at tetrahedral sites prior to exchange. (B) Transition state during electron−anion exchange. (C) Ground state after the exchange. The corresponding oxidation states of four involved yttrium atoms during each transition step are shown.

These calculations laid the groundwork for the key hypothesis to be tested experimentally: that an electron can be exchanged for an anion without reduction or oxidation of the atoms in a material. To begin exploring this hypothesis, we performed X-ray absorption near-edge structure (XANES, previously performed at Argonne, Figure 3-3b). The XANES is ambiguous, however, because the near-edge features are poorly resolved due to broadening intrinsic to the yttrium k-edge. This broadening would further obscure the assignment of oxidation states if two oxidation states are simultaneously present in a single sample (i.e., as could be seen during electrochemical cycling) or in cases of surface oxidation (i.e., as possibly observed in XPS). Therefore, we sought to resolve the ambiguity of previous measurements using a direct, bulk-sensitive probe of effective nuclear charge (high-energy resolution fluorescence detected XAS, HERFD XAS). These measurements enhanced our fundamental understanding and helped develop design rules that could improve battery performance.

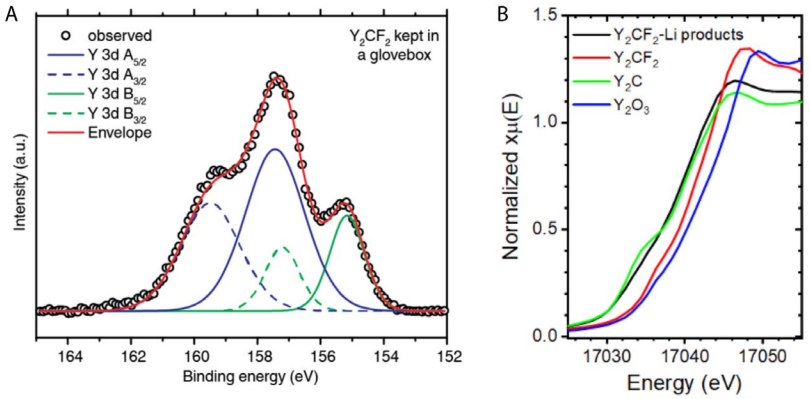


Figure 3 - 3: (A) X-ray photoemission spectra from Y_2CF_2 stored in a glovebox for the yttrium 3d core electron binding energies (B) XANES of Kα fluorescence for Y_2C, Y_2CF_2 and chemically defluorinated Y_2CF_2.

The solid lines in Figure 3-4a show the near-edge x-ray absorption spectroscopy (XANES) signatures of Y_2C and Y_2CF_2. The measurements were normalized to the linear fit of the extended x-ray absorption fine structure (EXAFS) signal. There are defined pre-edge features at 17040.1eV and 17042.4eV for Y_2C and Y_2CF_2, respectively. Pre-edge features can be attributed to excitations from 1s to the d-band in transition metals[8]. Therefore, unoccupied states in the 4d band account for both Y_2C and Y_2CF_2 pre-edge features. The energy transitions between the 1s and 5p orbitals cause the edge peak at 17051.6eV for Y_2C and 17052.7eV for Y_2CF_2. The excitation energies are shifted down about 1-2eV from Y_2C to Y_2CF_2. These shifts in energy can be caused by many factors. For instance, bonding fluorine to yttrium can shift the absorption energy due to orbital hybridization[6]. The shift could also be caused by Coulombic interactions between the excited electron interacting with electrons in the valence band and the orbitals of surrounding atoms. This effect, known as screening, can be affected by covalency, atomic number, coordination number, and oxidation state[30].

Due to the changes in structure between the Y_2C and Y_2CF_2, the interpretation of XAS measurements can be difficult. Indeed, XAS is primarily a "fingerprinting" technique, where a standard sample is used to calibrate a spectrum, and slight additions such as surface absorbate[31], doping concentration[32], and geometry[33] can result in systematic peak shifts. To better understand the spectral dependence on structure in the Y_2C/Y_2CF_2 system, one must create a model to relate features to electronic structure effectively.

Thus, we employed high-quality electronic structure[18,] models to understand the spectral characteristics observed in the XANES, providing deep insight into the electronic structure of our materials. The most rigorous of approaches for calculating the core-hole absorption XAS spectra, particularly in the near-edge region that gives information about oxidation states[11], use the Bethe-Salpeter Equation (BSE) paired with DFT to model core-hole attraction. These structural optimizations predict structural motifs for both Y_2C and Y_2CF_2 that can be observed experimentally with XRD. Thus, we have a high degree of confidence for using these structural optimizations to model the near-edge XAS features. The dotted red lines in Figure 3-4a show the simulated spectra for Y_2C and Y_2CF_2 XAS calculations, accounting for lifetime broadening to identify and their corresponding transitions. We found that the near edge features predicted by DFT-BSE in the EXCITING code were nearly identical to the near edge features observed experimentally for each material calculated. Thus, we have confidence that the electronic structure models predicted in DFT apply to the experimentally synthesized systems.

Creating a DFT model that reflects observed electronic structure characterization provides a test bed to further understand Y_2C and Y_2CF_2 *in silico*. Thus, we set out to predict the oxidation states of these materials using a novel algorithm, BadELF, developed to partition the electride electron and integrate its charge density[16]. This method found that the experimental spectroscopic signatures of both Y_2C and Y_2CF_2 are a result of yttrium atoms existing in the +1.98 and +2.10 oxidation state, respectively (Figure 3-4b, 3-4c).

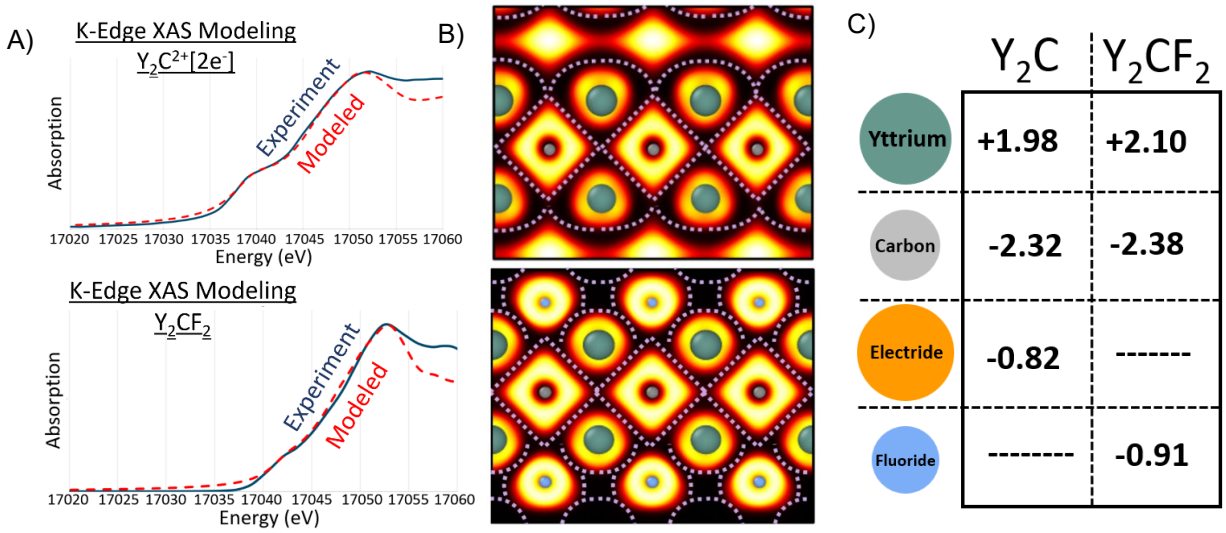


Figure 3 - 4: Electronic structure characterization of using A) K-Edge Synchrotron X-Ray Absorption Spectroscopy, subsequently modeled by the Bethe-Salpeter Equation as part of the EXCITING Density Functional Theory Package. B) Using Bader partitioning of the electron-localization function (BadELF), the charge density was integrated around both nuclear and non-nuclear electron attractors to find C) oxidation states of atomic species in Y_2C and Y_2CF_2

3.4 Conclusion

These results are extremely exciting; they suggest that the yttrium atoms do not undergo oxidation or reduction upon electrochemical fluorination**.** The exotic electronic behavior of the electride suggests a mechanism in which the fluoride ions exchange directly for the electride electron upon fluorination. This results in surprising behavior of the host crystal lattice – upon fluorination, the structure only undergoes a

7% change in volume. The slight structural reorganization could lead to batteries that can undergo long charging and discharging cycles without degradation - ultimately providing batteries with higher capacity that operate for longer periods of time.

REFERENCES

1. Celik Kucuk, A., Yamanaka, T., Yokoyama, Y. & Abe, T. Low-Cost Fluoride Source for Organic Liquid Electrolyte-Based Fluoride Shuttle Battery. *J Electrochem Soc* **168**, 010501 (2021).

2. Davis, V. K. *et al.* Room-temperature cycling of metal fluoride electrodes: Liquid electrolytes for high-energy fluoride ion cells. *Science (1979)* **362**, 1144–1148 (2018).

3. Druffel, D. L. *et al.* First-Principles Prediction of Electrochemical Electron–Anion Exchange: Ion Insertion without Redox. *J Phys Chem Lett* **11**, 9210–9214 (2020).

4. Bauer, M. HERFD-XAS and valence-to-core-XES: New tools to push the limits in research with hard X-rays? *Physical Chemistry Chemical Physics* **16**, 13827–13837 (2014).

5. Zhuo, Z. *et al.* Spectroscopic Signature of Oxidized Oxygen States in Peroxides. *Journal of Physical Chemistry Letters* **9**, 6378–6384 (2018).

6. Geoghegan, B. L. *et al.* Combining Valence-to-Core X-ray Emission and Cu K-edge X-ray Absorption Spectroscopies to Experimentally Assess Oxidation State in Organometallic Cu(I)/(II)/(III) Complexes. *J Am Chem Soc* **144**, 2520–2534 (2022).

7. Kowalska, J. K., Lima, F. A., Pollock, C. J., Rees, J. A. & DeBeer, S. A Practical Guide to High-resolution X-ray Spectroscopic Measurements and their Applications in Bioinorganic Chemistry. *Israel Journal of Chemistry* vol. 56 803–815 Preprint at https://doi.org/10.1002/ijch.201600037 (2016).

8. De Groot, F., Vankó, G. & Glatzel, P. The 1s x-ray absorption pre-edge structures in transition metal oxides. *Journal of Physics Condensed Matter* **21**, (2009).

9. Springer-Verlag, ©, Waychunas, G. A., Apted, M. J. & Brown, G. E. *PHYSICS CIIEMIS]RY MIHERALS X-Ray K-Edge Absorption Spectra of Fe Minerals and Model Compounds: Near-Edge Structure*. *Phys Chem Minerals* vol. 10 (1983).

10. Bzheumikhova, K. *et al.* Near-edge x-ray absorption and emission of cyanates and thiocyanates. *Phys Rev B* **106**, (2022).

11. Vorwerk, C., Aurich, B., Cocchi, C. & Draxl, C. Bethe-Salpeter equation for absorption and scattering spectroscopy: Implementation in the exciting code. *Electronic Structure* **1**, (2019).

12. Gilmore, K. *et al.* Efficient implementation of core-excitation Bethe Salpeter equation calculations. (2016) doi:10.1016/j.cpc.2015.08.014.

13. Vinson, J. Advances in the ocean-3 spectroscopy package. *Physical Chemistry Chemical Physics* vol. 24 12787–12803 Preprint at https://doi.org/10.1039/d2cp01030e (2022).

14. Yao, Y., Golze, D., Rinke, P., Blum, V. & Kanai, Y. All-Electron BSE@ GW Method for K-Edge Core Electron Excitation Energies. *J Chem Theory Comput* **18**, 1569–1583 (2022).

15. Vinson, J. Faster exact exchange in periodic systems using single-precision arithmetic. *Journal of Chemical Physics* **153**, (2020).

16. Weaver, S. M. *et al.* Counting Electrons in Electrides. *J Am Chem Soc* **145**, 26472–26476 (2023).

17. Hamalainen, K., Siddons, D. P., Hastings, J. B. & Berman, L. E. *Elimination of the Inner-Shell Lifetime Broadening in X-Ray-Absorption Spectroscopy*. (1991).

18. Gulans, A. *et al.* exciting: a full-potential all-electron package implementing density-functional theory and many-body perturbation theory. *Journal of Physics: Condensed Matter* **26**, 363202 (2014).

19. Kresse, G. & Furthmüller, J. Efficient iterative schemes for ab initio total-energy calculations using a plane-wave basis set. *Phys Rev B* **54**, 11169–11186 (1996).

20. Krukau, A. V, Vydrov, O. A., Izmaylov, A. F. & Scuseria, G. E. Influence of the exchange screening parameter on the performance of screened hybrid functionals. *J Chem Phys* **125**, 224106 (2006).

21. Carbone, M. R. *et al.* Lightshow: a Python package for generating computational x-ray absorption spectroscopy input files. (2022).

22. Sundberg, J. D., Benjamin, S. S., McRae, L. M. & Warren, S. C. Simmate: a framework for materials science. *J Open Source Softw* **7**, 4364 (2022).

23. Blöchl, P. E. Projector augmented-wave method. *Phys Rev B* **50**, 17953–17979 (1994).

24. Perdew, J. P. *et al.* Restoring the Density-Gradient Expansion for Exchange in Solids and Surfaces. *Phys Rev Lett* **100**, 136406 (2008).

25. Moellmann, J. & Grimme, S. DFT-D3 Study of Some Molecular Crystals. *The Journal of Physical Chemistry C* **118**, 7615–7621 (2014).

26. Grimme, S., Ehrlich, S. & Goerigk, L. Effect of the damping function in dispersion corrected density functional theory. *J Comput Chem* **32**, 1456–1465 (2011).

27. Ong, S. P. *et al.* Python Materials Genomics (pymatgen): A robust, open-source python library for materials analysis. *Comput Mater Sci* **68**, 314–319 (2013).

28. Toyoura, K., Koyama, Y., Kuwabara, A., Oba, F. & Tanaka, I. First-principles approach to chemical diffusion of lithium atoms in a graphite intercalation compound. *Phys Rev B* **78**, 214303 (2008).

29. Okubo, M., Tanaka, Y., Zhou, H., Kudo, T. & Honma, I. Determination of Activation Energy for Li Ion Diffusion in Electrodes. *J Phys Chem B* **113**, 2840–2847 (2009).

30. Singh, J., Lamberti, C. & Bokhoven, J. A. V. Advanced X-ray absorption and emission spectroscopy: In situ catalytic studies. *Chem Soc Rev* **39**, 4754–4766 (2010).

31. van Bokhoven, J. A. *et al.* Activation of Oxygen on Gold/Alumina Catalysts: In Situ High-Energy-Resolution Fluorescence and Time-Resolved X-ray Spectroscopy. *Angewandte Chemie International Edition* **45**, 4651–4654 (2006).

32. Ghigna, P. *et al.* Lithiation Mechanism in High-Entropy Oxides as Anode Materials for Li-Ion Batteries: An Operando XAS Study. *ACS Appl Mater Interfaces* **12**, 50344–50354 (2020).

33. Radu, D. *et al.* Geometric and electronic structure of α-oxygen sites in Mn-ZSM-5 zeolites. *Journal of Physical Chemistry C* **112**, 12409–12416 (2008).

This work is based on research conducted at the Center for High-Energy X-ray Sciences (CHEXS), which is supported by the National Science Foundation (BIO, ENG and MPS Directorates) under award DMR-234233

CHAPTER 4: HIGH-THROUGHPUT DISCOVERY OF ELECTRIDE DOPANTS

Connor C. Slamowitz, Samuel M. Weaver

4.1 Introduction

Rechargeable batteries have led to a revolution in sustainable energy storage, facilitating the transport and containment of power for use in electric vehicles and consumer electronics[1]. Due to the promise of cheap and available energy storage, battery chemistries that use alternative ions are being explored to develop high-capacity batteries that operate for longer periods of time at lower monetary costs. Among these chemistries is fluoride – an ion that is stable against oxidation, highly abundant in Earth's crust, and light in weight[2].

A key challenge for fluoride-ion batteries has been the development of stable electrodes that cycle repeatedly at room-temperature. The first fluoride-ion battery electrodes, reported in 2011, were binary metal-fluorides that underwent conversion reactions under electrochemical bias[3]. Since then, only a few layered electrodes[4–9] that percolate fluoride through topologically connected pathways have been developed. However, much of the volume of these layered materials is inactive for fluoride intercalation[8], resulting in low capacities. Moreover, most operate at cathodic voltages, meaning that layered anodes are largely unexplored.

To this end, we have proposed the use of Y_2C as a fluoride-ion battery anode[10]. Y_2C is an electride, meaning the structure holds an anionic electron in unique crystallographic lattice sites. Y_2C crystallizes in the $R\bar{3}m$ space group, in which layers of electron gas are sandwiched between layers of yttrium and carbon. We hypothesized that we could exchange the electride electron with a fluoride anion to form Y_2CF_2[11], and that this exchange would happen at highly reducing potentials, thus offering optimal properties for use as an anode in a fluoride-ion battery. Computational analysis predicted fast ion transport, with nudged-elastic band calculations predicting an activation energy of 156 meV to move fluoride between Wycoff sites[10]. These promising simulations and experiments suggest that Y_2C may be an optimal material for operation as an anode in a room-temperature fluoride-ion battery.

Although the activation energy to move fluoride between equivalent sites is small, initial electrochemical impedance spectroscopy experiments conducted with collaborators at the University of Stuttgart on fully fluorinated Y_2CF_2 showed exceedingly slow diffusion—indeed, so slow that it could not be measured. We hypothesize that the Y_2CF_2 fluorinates completely, leaving no F vacancies to facilitate F-ion transport. Thus, we predicted that if we doped the material to create vacancy sites, we could improve F-ion conductivity[12–15] .

In this chapter, we attempt to improve F-ion transport by doping the yttrium site in the Y_2C/Y_2CF_2 anode. Due to the many candidates for doping Y_2C, we utilize high-throughput computation to screen metal dopants. The study reveals that the most promising dopant candidates are calcium and strontium, which are 1 column to the left of yttrium. To conceptually understand these dopants, we explore the electronic structure of a calcium-doped Y_2C, and compare this to a titanium-doped Y_2C, which is 1 column to the right of yttrium. Finally, we show promising experiments that indicate Ca and Sr may indeed be doped into Y_2CF_2.

4.2 Methods

4.2.1 High Throughput DFT Studies

Systematic doping of Y_2C and Y_2CF_2 was performed using a high-throughput computational method combining Vienna ab-initio Simulation Package (VASP)[16] and Python. The aim was to identify suitable metal dopants from a set of 30 metals based on their potential to create vacancy-conductive structures. Five distinct structures were modeled: metal-doped $Y_{2-x}M_xC$; metal-doped $Y_{2-x}M_xCF_2$; metal-doped $Y_{2-x}M_xCF_{2-x}$ with vacancies localized either near or far from the dopant; and metal-doped $Y_{2-x}M_xCF_{2-(x^*_{ox})}$ containing two vacancies near the dopant. Formation energies were analyzed to assess dopant stability, synthesizability, vacancy formation near dopants, and resistance to full fluorination.

Initial geometry optimization was conducted on Y_2C and Y_2CF_2 structures using VASP with the r^{2}SCAN functional[17], an energy cutoff of 520 eV, and a k-spacing of 0.15 Å^{-1}. Optimized geometries served as seeds for generating cubic supercells (>9 Å lattice vector) via pymatgen[18] in Python, resulting in a 90-atom Y_2CF_2 and a 54-atom Y_2C supercell. Subsequently, Python scripts were employed to systematically

replace yttrium with dopant metals, prepare input files (POTCAR, POSCAR, INCAR), and automatically submit geometry optimization and single-point energy calculations.

4.2.2 DFT of Doped Electrides

All DFT calculations used for Charge Density and ELF calculations were performed using VASP[16]. The projector-augmented wave potentials were used[19] to describe core electrons and all calculations were performed taking spin polarization into account. For each dopant (Y, Ti, Ca) a single dopant atom was placed in a supercell of Y_2C ($Y_{36}C_{18}$) or Y_2CF_2 ($Y_{36}C_{18}F_{36}$). An initial structural relaxation was performed followed by a single-point energy calculation using the meta-GGA r^{2}SCAN functional[17]. For the relaxations, the plane-wave energy cutoff was 520 eV and a gamma centered k-point grid with a spacing of 0.5 $Å^{-1}$ was used. The energy break condition in the electronic SC-loop was set to 1 x 10^{-4} eV and the break condition for the ionic step was 1 x 10^{-3} eV. Similar settings were used for the single-point energy calculations, but the k-point grid spacing was decreased to 0.15 $Å^{-1}$ and the charge density and ELF grids were set to a voxel density of ~27 voxels/Å along each unit cell edge. Additional relaxation and static-energy calculations were performed on larger supercells of Y_2C ($Y_{288}C_{144}$). The settings were the same as that for the relaxations of the smaller supercells.

Oxidation states and charge density/ELF difference plots were obtained using the BadELF algorithm[20] incorporated in the Simmate software[21].

4.2.3 Synthesis of Calcium Doped Y_2CF_2

The synthesis of calcium doped Y_2CF_2 is adapted from Druffel at alias' synthesis of Y_2CF_2[11]. First, Y_2C was synthesized by first arc-welding yttrium metal (Alfa Aesar, ~40mesh powder, 99.6% (REO)) with graphitic carbon (Sigma-Aldrich). Metal doped Y_2CF_2 was then synthesized by the solid-state reaction of YF_3, Y_2C, graphite (Sigma-Aldrich), and MF_2 (M = Ca, Sr, Strem Chemicals). The reagents were ground into a fine powder in a stoichiometric ratio and pressed into a pellet under ~0.56 GPa of pressure using a hydraulic press. The pellet was welded inside an ampule made of tantalum (Ta) metal. To fashion an ampule, a Ta cap was hammered into Ta tubing and sealed in argon by welding the cap and tubing together with an electric arc. The Ta tubing, 99.95% Ta seamless tubing, was purchased from Eagle Alloys in a 1 cm diameter and cut to 5 cm lengths. The caps were made of the same Ta. After welding the reagents inside a Ta ampule, the Ta ampule was sealed in a fused quartz ampule under 1 mbar Ar. Then the vessel

was placed in a tube furnace and heated to 1513 K at a ramp rate of 10 K/min. The temperature was held at 1513 K for 3 days, then cooled to 1273 K over 10 h, then to 1073 K over 5 h, and to room temperature over 5 h. The ampule was then brought into the glovebox and opened with a pipe cutter. The pellet remained intact through the reaction.

4.3 Results and Discussion

4.3.1 High Throughput Discovery of Stable Dopants

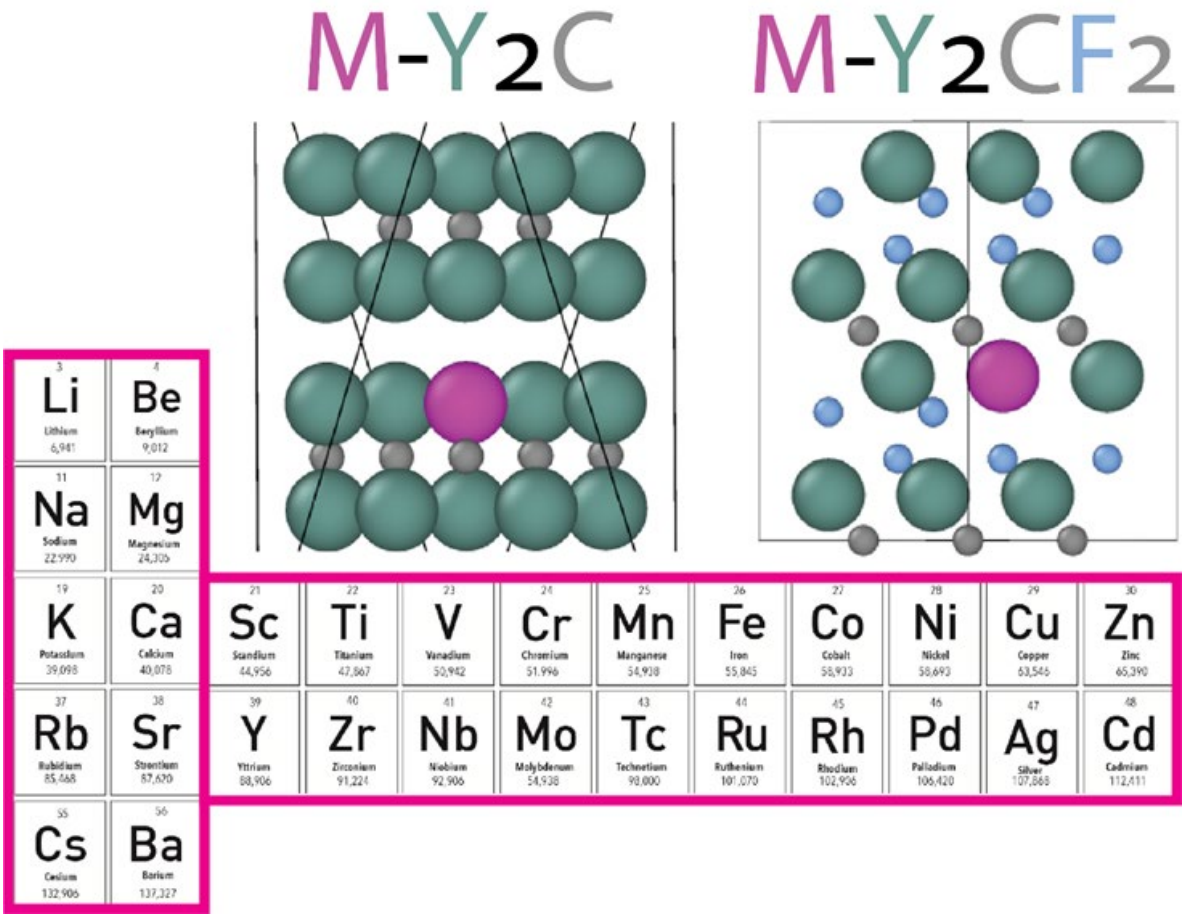


Figure 4 - 1: Schematic of dopant structure and metals used in high throughput doping calculations. Supercells were created such that coulombic interactions were negligible between vacancy sites,

with 90 atoms in M-Y_2CF_2, 89 in M-Y_2CF_2 - 1x, and 88 in M-Y_2CF_2 - 2x. 54 atoms were used in the M-Y_2C structures.

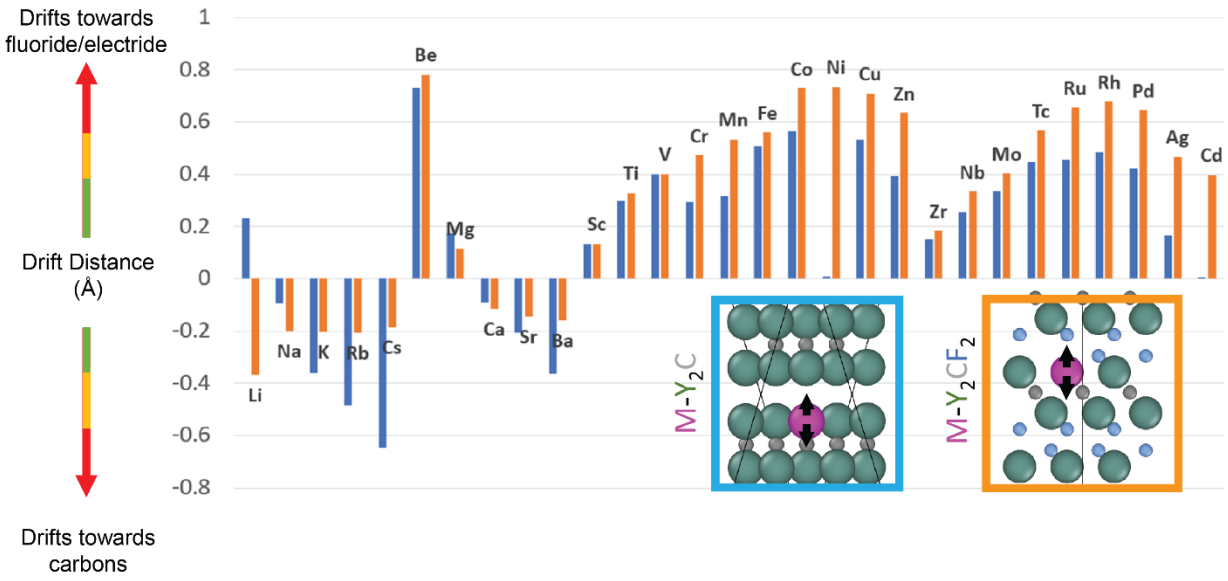


Figure 4 - 2: Measurement of the displacement in the z-direction of inserted ions during the geometry optimization of doped structures. The atoms drifted either towards the fluoride/electride layer, resulting in a positive drift, while a negative drift corresponds to drift towards the carbide layer. We set arbitrary drift magnitude limits of 0.3 Å by qualitatively analyzing relaxed structures.

We conducted a high-throughput DFT study of metals that could replace the yttrium atom and induce systematic vacancies and enable fluoride transport. This analysis optimized 150 Y_2C and Y_2CF_2 superstructures. These structures consisted of 30 potential metal dopants at 3% doping concentration, seeded on yttrium sites such that Coulombic interactions between doped sites were negligible. The structures were fluorinated to various degrees to measure the thermodynamic favorability of vacancy formation.

We first performed a geometry optimization of doped Y_2C and Y_2CF_2 structures to determine the favorable position of the metal dopant. To do this, we calculated the displacement of the dopant ion before and after optimizing the geometry. We found that alkali and alkali earth elements relaxed towards the carbide layer, while transition metals relaxed towards the electride layer. Furthermore, we found that ions that were closest in size to yttrium relaxed the smallest distance. To this end, it is possible that the migration of the ion during relaxation could be a function of electronegativity.

The movement of the dopant from the original yttrium site likely has some bearing on the effectiveness of the dopant in creating a stable material with the desired fluoride vacancy. If the dopant is not stable in the yttrium site, the synthesis of a material with a large dopant concentration could profoundly transform its structure and alter the diffusion pathway for fluoride.

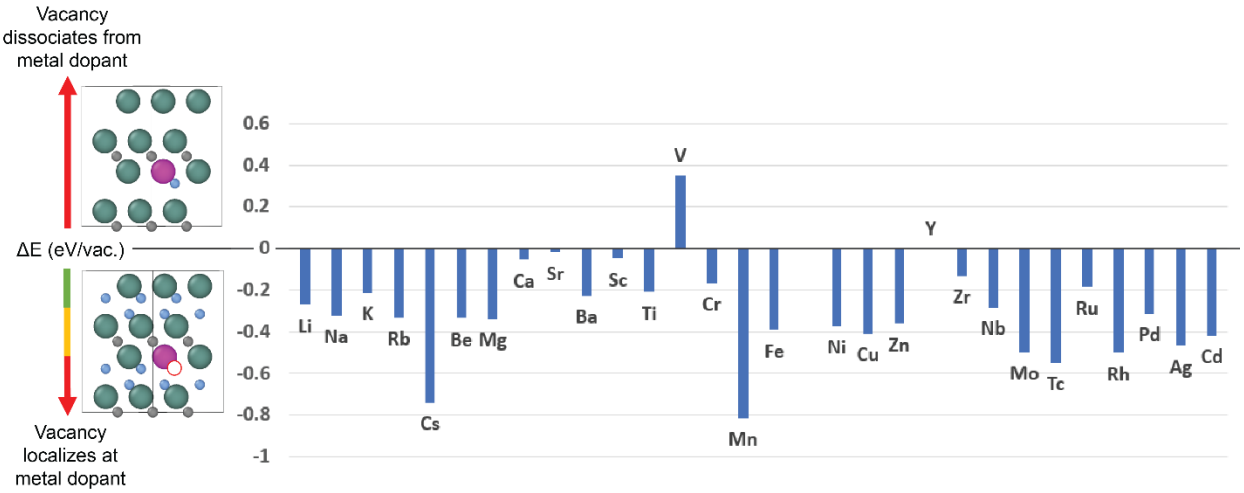


Figure 4 - 3: DFT calculations resulting in the enthalpy of formation (eV/vac) for structures with fluoride near the dopant site and a vacancy near the dopant site. A negative ΔE is ideal as it represents favorable formation energy for materials with vacancies that localize at the dopant site. However, the near-vacancy structure should not be too stable, as it would significantly increase the activation energy for vacancy hopping.

However, just because a system forms vacancies, does not mean that the vacancy is mobile. This is important because the energy to fluorinate the doped system must be high enough to induce vacancies. However, one must consider sites that are too high energy as inaccessible. In a sense, exceptionally high energy vacancy sites would *reduce* the ionic conductivity, because the vacancy would not be mobile.

To understand the tendency for the vacancy to localize at the dopant, we looked at the energy difference between structures with the vacancy adjacent to the dopant and the vacancy placed some distance away from the dopant. Among all dopants, we found that only calcium, strontium and cadmium induced vacancies that were moderately lower in energy than the fully fluorinated doped materials, allowing fluoride to pass through the vacancy sites without significant activation energy. Ultimately, these materials would allow fluoride to pass through the crystallographic sites without significantly hindering the energy density of the material.

Finally, we calculated the enthalpy of formation for the doped systems. This provided insight into the reactions for which we would be able to synthesize. For each condition, we proposed a reaction mechanism:

$M - Y_2C$: $Y_2C + M_x \rightarrow Y_{2-x}CM_x + Y_x$

$M - Y_2CF_2$: $Y_2CF_2 + M_x \rightarrow Y_{2-x}CM_xF_2 + Y_x$

$M - Y_2CF_2 - 1x$: $Y_2CF_2 + M_x \rightarrow Y_{2-x}CM_xF_{2-x} + {}^1/_3 YF_3 + {}^2/_3 Y_x$

$M - Y_2CF_2 - 1x$: $Y_2CF_2 + M_x \rightarrow Y_{2-x}CM_xF_{2-(x*ox.)} + {}^2/_3 YF_3 + {}^1/_3 Y_x$

to determine the enthalpy of reaction given a dopant. We found that the electride like structures tended to be the most stable, most likely caused by the large interlayer space of Y_2C which provides room for structural expansion or contraction. As the vacancy concentration increased, we found that the enthalpy of formation also increased. The materials that had the highest probability for formation were Ca, Sr, Ti, V, Co, Zn, Ru, and Cd. Taking into account all success criteria, we find that the dopants with the highest probability of success would be Ca, Sr, Ti, and Cd. Given safety concerns with Cd, we propose to synthesize Ca and Sr doped structures and analyze the effects of Ti in an electridic environment.

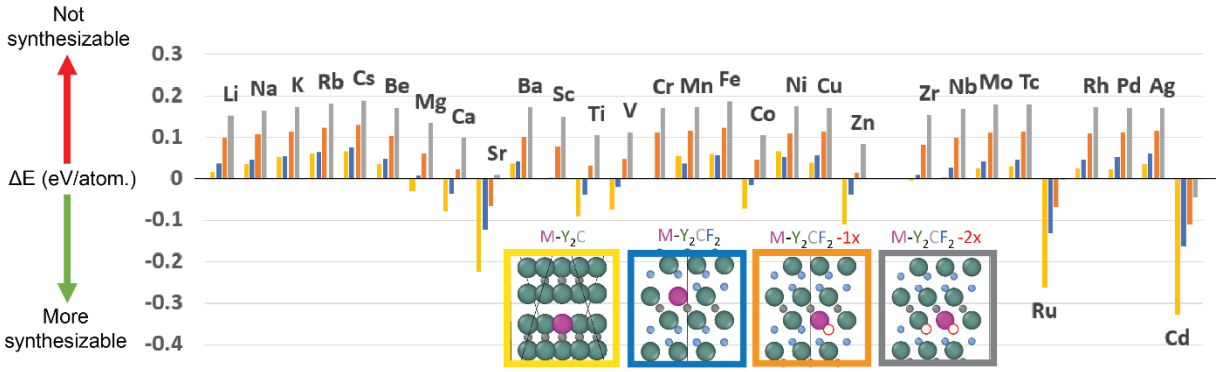


Figure 4 - 4: Enthalpy of formation for metal doped Y_2C (yellow), metal doped Y_2CF_2 (blue), metal doped Y_2CF_2 with 1 vacancy site (orange), and metal doped Y_2CF_2 with 2 vacancy sites (grey).

4.3.2 Doping Effects on Electride Characteristics

To investigate the effect of the dopant in Y_2C, we performed BadELF[20] calculations on Ca and Ti doped Y_2C supercells ($MY_{35}C_{18}$) to compare oxidation states and electron counts to the undoped system. Ti and Ca add and remove a valence electron in the system respectively. However, the dopants take on

oxidation states that result in relatively small changes to charges in the overall system. The Y in undoped Y_2C takes an oxidation state of +1.95, close to a formal oxidation state of +2. Ca and Ti take on similar oxidation states of +1.51 and +2.09 respectively. While this is a common oxidation state for Ca, it is less so for Y and Ti which typically prefer +3 and +4 respectively. The low-lying d-orbitals in these transition metals combined with the large excess of electrons in the system are likely the cause of this phenomenon. Interestingly, this consistency in oxidation state results in fairly small changes to the bare electron count for the whole system. $TiY_{35}C_{18}$ gains 0.2 bare electrons and $CaY_{35}C_{18}$ loses 0.2 bare electrons. This suggests that regardless of dopant, it is difficult to change the bulk electron count.

However, the local bare electron cloud is quite fragile. Charge density difference plots of the bare electron cloud show a decrease in charge density adjacent to the dopant regardless of type (Figure 4-6). In Ca system this is likely caused by the Ca having fewer electrons to provide to the bare electron volume relative to the surrounding Y atoms. In the Ti system, this may be the result of the abnormally low oxidation state indicating an excess of electrons on the Ti atom which repulse nearby bare electrons. In both cases, the decrease in charge density around the dopant suggests that fluoride would likely avoid the immediate area of the dopant, likely contributing to increased energy of fluoride movement.

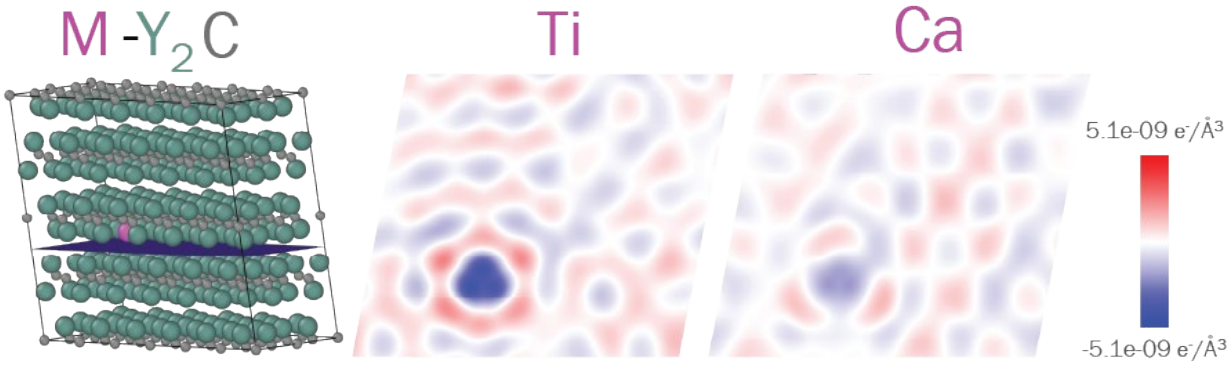


Figure 4 - 5: Charge density difference plots through an electride layer. Lower values (blue) correspond to regions where charge density is lower relative to the undoped Y_2C.

Interestingly, a similar trend is seen in the charge density around the fluoride vacancy of doped $Y_{2-x}CF_{2-x}$ supercells ($MY_{35}C_{16}F_{35}$). Both dopants result in a decrease in charge density at the F vacancy, corresponding to the loss of a bare electron at the site (Figure 4-7). This is further evidenced by an ELF difference plot which shows a decrease of 0.95 indicating the loss of localization at this site. In Ca's case,

this reflects the inability of the structure to take on another fluoride while still allowing for fluoride movement through the vacant space.

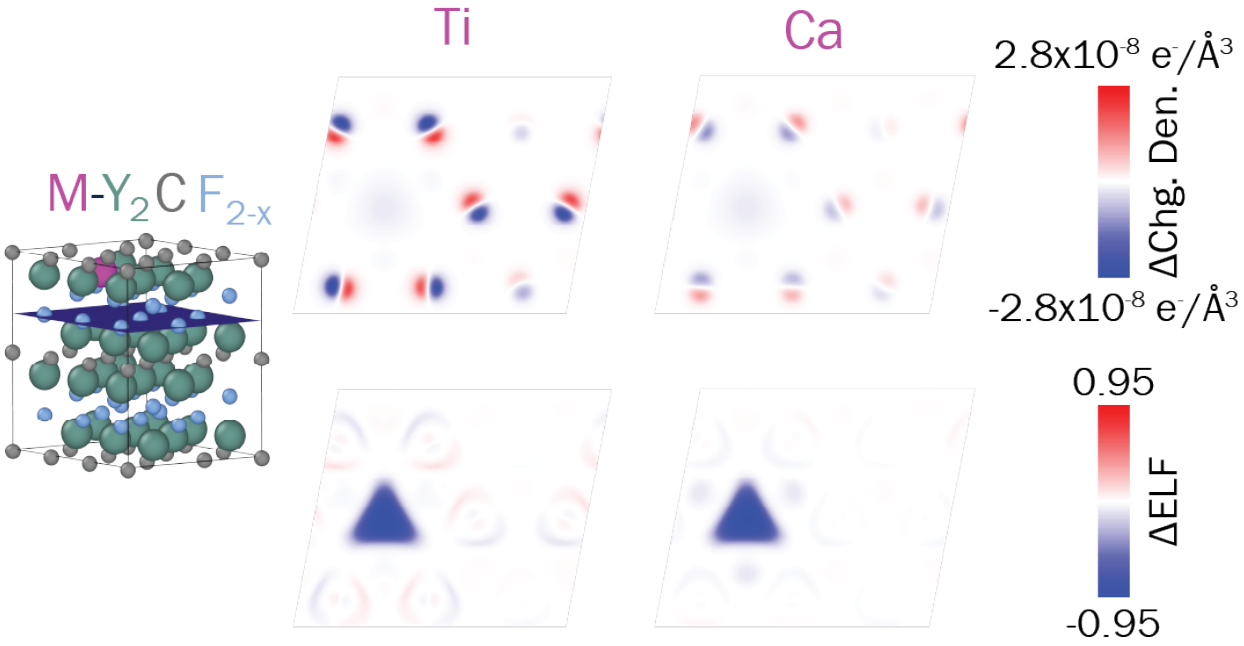


Figure 4 - 6: Charge density and ELF difference plots through a fluoride layer with a single vacancy. Lower values (blue) correspond to regions where the charge density or ELF is lower relative to the undoped Y_2C.

4.3.3 Synthesis of Doped Y_2CF_2

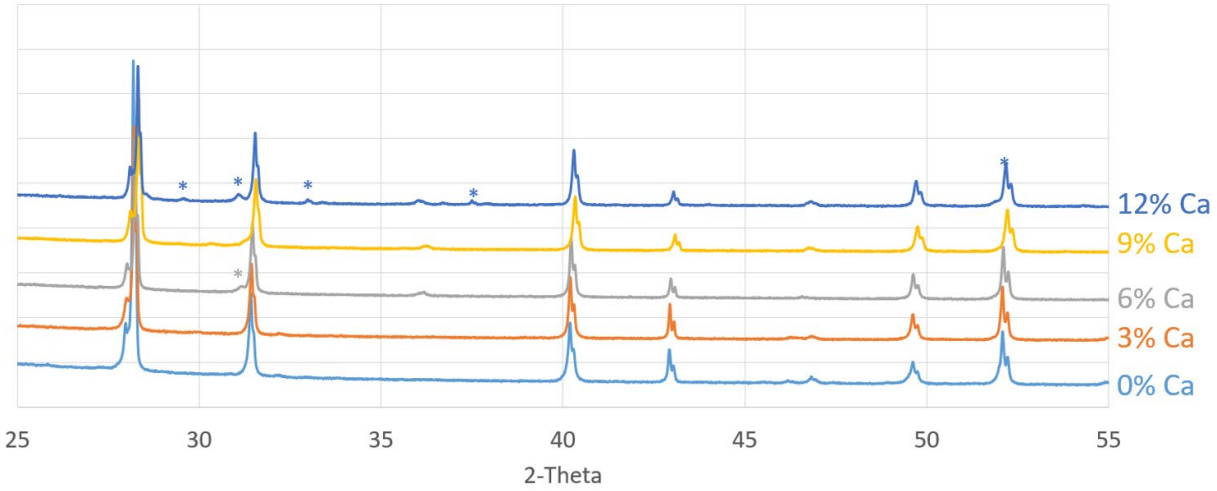


Figure 4 - 7: XRD of $Y_{2-x}Ca_xCF_{2-x}$, where x represents the moles of Calcium stoichiometrically added to the synthesis. The % doped represents the % of yttrium sites occupied by calcium. As the percentage of calcium increases past 9%, the formation of parasitic phases begin to grow, represented by blue asterisks.

We have successfully synthesized the calcium doped $Y_{2-x}CF_{2-x}$ sample and characterized using x-ray diffraction. The XRD reveals an interesting trend as a function of doping concentration. As calcium concentration increases, peaks along the *00l* reflection decrease in intensity (Figure 4-8). I hypothesize that the calcium dopant disorders the fluorine that sit in the interlayer space of $Y_{2-x}Ca_xCF_{2-x}$. Furthermore, as the concentration of calcium increases, we observe parasitic phases nucleate and grow. Due to this, a concentration of Ca above 9% occupation would have large effects on the performance of doped batteries. These parasitic side reactions are also observed with Sr doped Y_2CF_2 and nucleate at lower concentrations (Figure A4-1). Thus, further investigation into the Ca doped Y_2CF_2 is preferred. With these data in mind, my next goal is to electrochemically characterize the ionic conductivity in collaboration with the Pasta Laboratory at Oxford University before utilizing the material in a full battery architecture.

To better understand interactions between the electride electron and the doped metal, I am also working on methods to experimentally dope layered Y_2C instead of Y_2CF_2, which could lead to an interesting study on doped metal-electride hybridization. We plan to synthesize these materials, characterize them, and study their electronic structure. Difficulty in this procedure arises from the volatility of the dopant metal. The

synthetic procedure for synthesizing Y_2C calls for the use of a high temperature, arc welding apparatus that can reach temperatures exceeding 5000°C. I may be able to explore reactants such as SrC_2 and CaC_2, both of which have higher boiling points than their bulk elemental counterparts, to directly dope Y_2C.

4.4 Conclusion

The discovery of new fluoride battery electrodes motivates the exploration of exotic materials for high-voltage, large capacity batteries. The Y_2C layered electride is an exceptionally promising anode for FIBs – however, the full conversion of Y_2C to Y_2CF_2 prohibits fast diffusion due to low vacancy concentration. Inspired by LIBs, we perform a high throughput doping study to find accessible dopants to systematically induce vacancies into Y_2CF_2. From this study, we identified 4 potential metal dopants that are aliovalent to yttrium yet roughly have the same ionic radius. We show how heuristics that determine ideal dopants for non-electride dopants hold true for electrides. Furthermore, due to the unique electronic nature of the Y_2C, we study the effects of these dopants on the electronic structure of the material. Across the periodic table, we find that transition metals with low-lying d-orbitals tend to have dynamic oxidation states, accessing unique oxidation states for the metal cations. However, alkali and alkali-earth metals tend to remain in their most stable oxidation state. These trends create a system in which both titanium and calcium decrease the electron density in the electride site, effectively acting as a vacancy-inducing dopant. Finally, I attempted to synthesize Ca and Sr doped Y_2CF_2. Although Sr creates a binary phase system, Ca successfully incorporates into yttrium sites up to nearly 10% occupation. These exciting results lay the groundwork to test the ionic conductivity electrochemically.

REFERENCES

1. *2024 Battery Report*. (2024).

2. Nowroozi, M. A. *et al.* Fluoride ion batteries - past, present, and future. *Journal of Materials Chemistry A* vol. 9 5980–6012 Preprint at https://doi.org/10.1039/d0ta11656d (2021).

3. Anji Reddy, M. & Fichtner, M. Batteries based on fluoride shuttle. *J Mater Chem* **21**, 17059–17062 (2011).

4. Clemens, O. *et al.* Electrochemical fluorination of perovskite type BaFeO2.5. *Dalton Transactions* **43**, 15771–15778 (2014).

5. Nowroozi, M. A., Wissel, K., Rohrer, J., Munnangi, A. R. & Clemens, O. LaSrMnO4: Reversible Electrochemical Intercalation of Fluoride Ions in the Context of Fluoride Ion Batteries. *Chemistry of Materials* **29**, 3441–3453 (2017).

6. Nowroozi, M. A., Ivlev, S., Rohrer, J. & Clemens, O. La2CoO4: A new intercalation based cathode material for fluoride ion batteries with improved cycling stability. *J Mater Chem A Mater* **6**, 4658–4669 (2018).

7. Nowroozi, M. A., Wissel, K., Rohrer, J., Munnangi, A. R. & Clemens, O. LaSrMnO4: Reversible Electrochemical Intercalation of Fluoride Ions in the Context of Fluoride Ion Batteries. *Chemistry of Materials* **29**, 3441–3453 (2017).

8. Cao, Z. *et al.* Reversible Fluoride-Ion (De)Intercalation of CuLaO2 Cathodes with Crystalline/Amorphous Phase Transition Involving Multi-Electron Reaction. *ACS Appl Energy Mater* (2024) doi:10.1021/acsaem.4c01271.

9. Nowroozi, M. A. *et al.* High cycle life all-solid-state fluoride ion battery with La2NiO4+d high voltage cathode. *Commun Mater* **1**, (2020).

10. Druffel, D. L. *et al.* First-Principles Prediction of Electrochemical Electron-Anion Exchange: Ion Insertion without Redox. *Journal of Physical Chemistry Letters* 9210–9214 (2020) doi:10.1021/acs.jpclett.0c02266.

11. Druffel, D. L. *et al.* Synthesis and Electronic Structure of a 3D Crystalline Stack of MXene-Like Sheets. *Chemistry of Materials* **31**, 9788–9796 (2019).

12. Zhang, M. *et al.* Recent progress, challenges and prospects of electrolytes for fluoride-ion batteries. *Energy Reviews* **3**, 100083 (2024).

13. Trnovcová, V., Fedorov, P. P. & Furár, I. Fluoride solid electrolytes. *Russian Journal of Electrochemistry* **45**, 630–639 (2009).

14. Liu, L. *et al.* SnF2-based fluoride ion electrolytes MSnF4 (M = Ba, Pb) for the application of room-temperature solid-state fluoride ion batteries. *J Alloys Compd* **819**, (2020).

15. Wang, J. *et al.* A Fluoride-Ion-Conducting Solid Electrolyte with Both High Conductivity and Excellent Electrochemical Stability. *Small* **18**, (2022).

16. Kresse, G. & Furthmü, J. *Efficient Iterative Schemes for Ab Initio Total-Energy Calculations Using a Plane-Wave Basis Set*. (1996).

17. Furness, J. W., Kaplan, A. D., Ning, J., Perdew, J. P. & Sun, J. Accurate and Numerically Efficient r2SCAN Meta-Generalized Gradient Approximation. *J Phys Chem Lett* **11**, 8208–8215 (2020).

18. Ong, S. P. *et al.* Python Materials Genomics (pymatgen): A robust, open-source python library for materials analysis. *Comput Mater Sci* **68**, 314–319 (2013).

19. Blöchl, P. E. Projector augmented-wave method. *Phys Rev B* **50**, 17953–17979 (1994).

20. Weaver, S. M. *et al.* Counting Electrons in Electrides. *J Am Chem Soc* **145**, 26472–26476 (2023).

21. Sundberg, J. D., Benjamin, S. S., McRae, L. M. & Warren, S. C. Simmate: a framework for materials science. *J Open Source Softw* **7**, 4364 (2022).

CHAPTER 5: EXPLORATION OF ELECTROCHEMICAL (DE)INSERTION OF FLUORIDE IN THE Y_2C ELECTRIDE

Connor C. Slamowitz, Lauren M. McRae*, Daniel L. Druffel*

**contributing equally*

5.1 Introduction

The development of beyond-lithium-ion batteries relies on the advancement of electrodes in varying chemistries. While conversion-based anodes have been studied in metal-fluoride based electrodes[DON], the large volume changes that occur upon phase transformations require large overpotentials and dramatically limit the cycling stability[1]. Intercalation-type anodes are known to offer far superior cyclability; however, to date, studies on intercalation-type anode materials are very limited[2,3]. Few materials have been investigated as intercalation-type anodes, $SrTiO_3F_2$[4], $Sr_3Ti_2O_5F_4$[5] and Y_2C[6]. Unfortunately, these materials perform poorly because they did not have the key electrode properties necessary for stable intercalation and key electrolyte properties for room-temperature operation.

Intercalation involves the charge-transporting ion inserting/deinserting into a host material. In a high-performing electrode, intercalation/deintercalation results in a small expansionin the host's volume with minimal disruption of the bonding in the host structure. The lack of structural change limits mechanical degradation, which is one of the primary reasons that intercalation-type batteries offer superior cyclability. In addition, low activation energy for the charge-carrying ion to hop between sites in the electrode (ideally < 500 meV) directly correlates to faster ion diffusion, which facilitates the fast charge and discharge rates typical for intercalation-type batteries.Itercalation often employs an efficient atom economy (for example, in $LiCoO_2$ a ratio of 1:3 charge-carrying atoms:host atoms), which provides high maximum volumetric and gravimetric capacities.

Recently, we predicted a new mechanism of ion-insertion, called electron-anion exchange (EAX), that does not change the oxidation states of the host lattice and causes no significant volume expansion, making it ideal for intercalation chemistry[7]. EAX leverages the direct exchange of anions for electrons in

materials called electrides where bare electrons occupy distinct sites in the crystal lattice apart from atomic nuclei. In addition, the 2D electron gas (2DEG) formed by the partially delocalized electrons facilitates the diffusion of ions because the ions hardly experience deflection in 2DEG. We suggested that this chemistry could enable a class of anode materials for intercalation-type batteries.

In this study, we use computational methods to explore the feasibility of Y_2C to act as an anode in a FIB. Using the cluster expansion method followed by Monte Carlo simulations, we found several ground state structures with varying amounts of fluoride exist with the Y_2C $R\bar{3}m$ structure. Between $Y_2CF_{0.25}$ and Y_2CF_2, the ABC and AA-stacked structures exist concurrently as a hybrid of the $R\bar{3}m$ and $P\bar{3}m1$ structure in an alternating stacking structure. From this phase diagram, we are able to produce a voltage profile. To support the calculated voltage profile and explore the feasibility of electron-anion exchange experimentally, we used electrochemical experiments to fluorinate a Y_2C electrode. We find that the experimental voltage profile takes on a similar shape to the calculated profile, and we use x-ray diffraction (XRD) to explore the structure at points along the profile.

5.2 Methods

5.2.1 Density Functional Theory

Density functional theory (DFT) calculations were performed in the Vienna ab-initio Simulation Package (VASP) using the projector-augmented wave potentials to describe core electrons[8,9]. The generalized gradient approximation PBE functional was used for structural relaxation and energy calculations[10]. Prior to running DFT, we found symmetry for each structure with a tolerance of 0.001Å. For each structure, a structural relaxation was performed with an electronic break condition of 10^{-6} eV followed by a more rigorous single-point energy calculation with an electronic break condition of 10^{-7} eV. The plane-wave energy cutoff in both steps was 500 eV and the smallest allowed spacing between k-points was 0.4 $Å^{-1}$. The break condition for the forces in the ionic relaxation loop was 0.02 eV/Å and the zero damping DFT-D3 dispersion correction of Grimme was used[11].

5.2.2 Cluster Expansion Modeling

We mapped the energies obtained from our DFT calculations onto the CE model using the Cluster Expansion in Atomic Simulation Environment (CLEASE) code[12]. We trained the CE model using a total of

300+ configurations with supercells ranging from 2 to 256 atoms in size. The training set consisted of an initial pool of random structures, ground-state structures predicted by the CE model, and "probe structures" as described by Seko *et. al*[13]. We considered 1-, 2-, 3- and 4-body clusters with a maximum diameter of 7.0 Å for the 2- and 3-body clusters and 5.0 Å for the 4-body clusters. The effective cluster interactions (ECI) were evaluated using an l1-regularized linear regression scheme to minimize the leave-one-out cross validation (LOOCV) score.

5.2.3 Monte Carlo Simulations

Using the CE model, canonical Monte Carlo (MC) simulations were performed on expanded supercells consisting of more than 10,000 atoms using 100,000 trial steps. The positions of the F and vacancies were allowed to swap freely even if from different bases as in the H1-3 phase while the Y and C atoms were constrained. The temperature was fixed at 298 K.

5.2.4 Electrochemical Set-up

Y_2C is first synthesized using a high-temperature TIG welder at high voltage. An arc of electricity melts pure yttrium pieces with graphite flakes to create the ABC stacked layered Y_2C phase (shown in the XRD pattern, Figure 5-1a). Once the synthesis is confirmed, the material can be ground into a powder using planetary milling. Milling is done for approximately 15 minutes to allow the particles to become fine and uniform (SEM image, Figure 5-1b). The particles are mixed with Super P conductive additive and polyvinylidene fluoride (PVDF) binder at a weight ratio of 80:10:10. A slurry is created with propylene carbonate (PC). The mixture is doctor bladed onto tantalum foil. The slurry is allowed to dry overnight at 120^{o} C, and 15mm discs are punched from the foil (Figure 5-1c).

Electrochemical testing proceeded in a 3-electrode setup (Figure 5-1d), with a platinum counter electrode and silver wire reference electrode submerged in a 0.1M solution of silver triflate in MPPy-TFSI. Due to the chance of HF formation in the Np1F:BTFE electrolyte, the electrochemical cell consists of a custom built Teflon case. All charging experiments are completed with 0.3M Np1F in BTFE. Charging is done with a chronopotentiometry experiment, where a voltage is applied to the working electrode to achieve a constant current. The constant current and electrode mass dictate the charging rate (C-Rate) of the material.

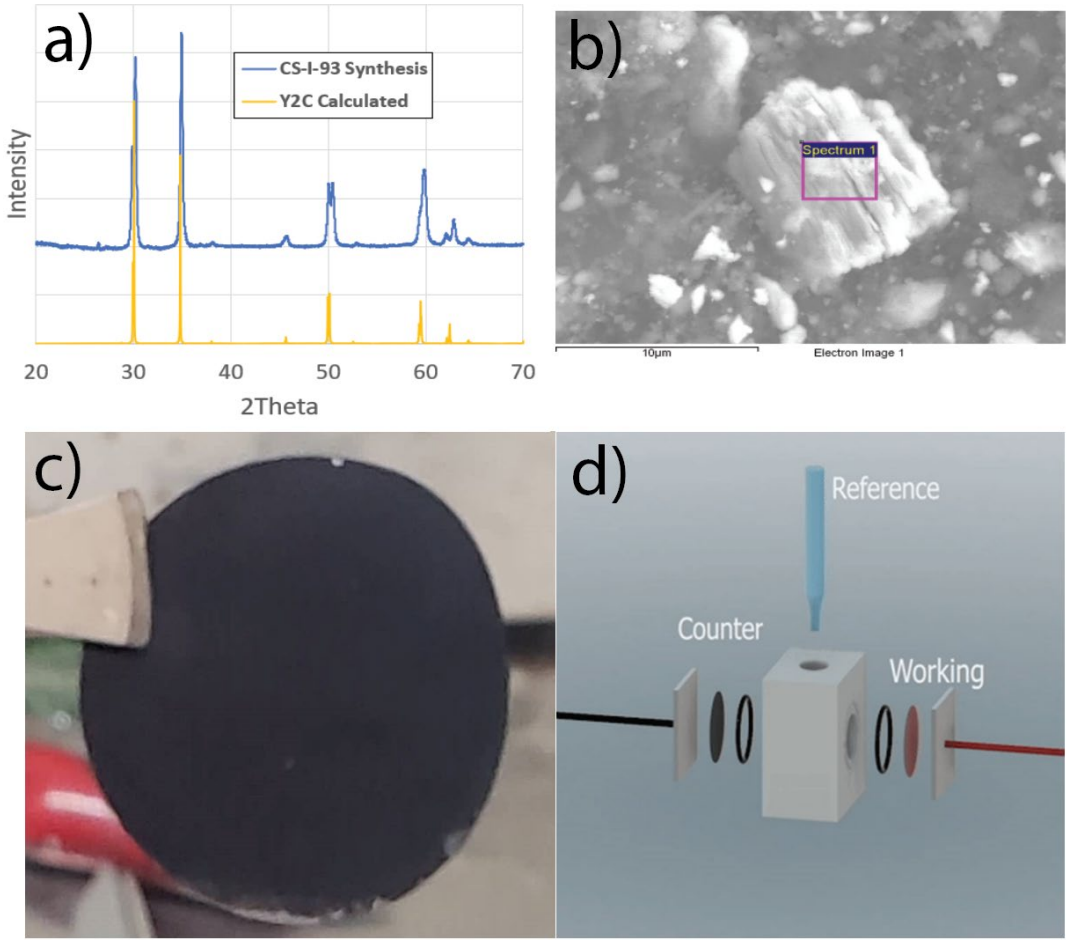


Figure 5 - 1: Preparation of the Y_2C intercalation electrochemical testing cell. a) Calculated vs synthesized spectra showing phase-pure Layered Y_2C, b) ball milled Y_2C particles, c) fabricated 15mm diameter electrode consisting of 80%wt Y_2C, 10%wt Super P, and 10% PVDF binder, and d) Full cube cell assembly.

5.2.5 Structure Analysis

All analyses were performed under inert atmosphere. Powdered samples of Y_2CF_x were characterized by x-ray diffraction (XRD) at room temperature in a capillary transmission geometry across a range of 20−150° using Cu Kα (λ=1.54056 Å) in a Rigaku Smartlab diffractometer. The pattern was indexed and refined using the PDXL software from Rigaku. Samples for transmission electron microscopy (TEM) and scanning transmission electron microscopy (STEM) were prepared by suspending Y_2CF_x powder in 1,3-dioxolane and sonicating for 30 minutes. Three microliters of the suspension were drop-cast onto a lacey carbon grid and dried under vacuum for 16 hours. The samples were loaded into a Thermo Scientific

Talos F200X Transmission Electron Microscope and studied at room temperature under high vacuum at an accelerating voltage of 200 kV. STEM samples were probed with a 7 nm condensed beam.

5.3 Results and discussion

5.3.1 Computational Exploration of Fluorinated Phases

To understand the phase evolution in Y_2C/Y_2CF_2 and to calculate the voltage profile for intercalation, we performed cluster expansion and Monte Carlo simulations. Cluster expansion rigorously extracts the effective F-F and F-vacancy interactions from hundreds of DFT calculations. Subsequently we employed those effective cluster interactions (ECI) in Monte Carlo simulations that result in our reported hull diagram and voltage profile.

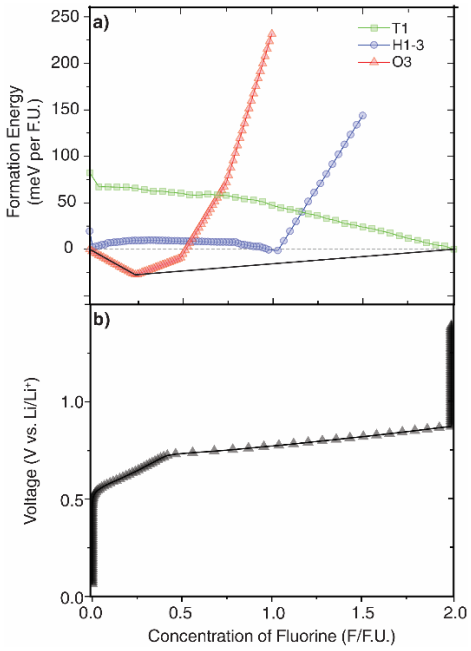


Figure 5 - 2: a) The convex hull for fluorine intercalation in Y_2C considering the O3, T1, and H1-3 phases with the formation energies given in meV/formula unit. The energies are calculated by canonical Monte Carlo simulations at 0K using ECIs from cluster expansion fitting. b) The predicted voltage profile for fluorine intercalation in Y_2C. The voltage is derived from chemical potential calculated with semi-grand canonical Monte Carlo simulations at 298K.

To use the cluster expansion method, we first identified a set of host phases that are likely to be stable. We considered three host phases, O3, T1, and H1-3, illustrated in Figure A5-1. We introduced the

O3 and T1 structures previously. The third, the H1-3 structure, is a hybrid of both O3 and T1. In the H1-3 structure, the unit cell consists of six layers of Y_2C in the $R\bar{3}m$ space group alternating between O3 and T1 stacking sequences. The unit cell of H1-3 shares the same a lattice vector as O3, but the c lattice vector is double that of the O3 phase to account for the six layers. In all the hosts, we assumed that the Y and C ions do not migrate. This is supported by DFT calculations suggesting that the activation barrier for C migration is more than 2 eV. Considering these three phases, we ran DFT calculations to calculate the ECIs and used the ECIs in Monte Carlo simulations to construct the convex hull diagram shown in Figure 5-2a.

Several important features about the phase stability are implied by the convex hull (solid black line in Figure 5-2). First, in agreement with our earlier calculations, at a concentration of zero F, the O3 host is more stable than the T1 host; Y_2C adopts the O3 phase. Second, at complete fluorination, the T1 host is more stable than the O3 host; Y_2CF_2 adopts the T1 phase. These findings match the experimental observation that at high temperatures the syntheses of Y_2C and Y_2CF_2 yield the O3 and T1 phases respectively. In addition, the convex hull reveals several stable ground states at low F concentrations. The convex hull is mainly shaped by the ground state at 0.25 F/F.U. with this O3-configuration exhibiting a formation energy of −25 meV/F.U. There are also ground states, all with the O3-stacking sequence, that lie below the linear interpolation between 0-0.25 F/F.U. (0-12.5%), affording a smoothly varying hull diagram in this region. This suggests that in the low F regime, the ordered configurations of fluorine within the O3-stacking sequence of the Y_2C lattice effectively evolve continuously with intercalation of fluorine up to 0.25 F/F.U. With intercalation of fluorine beyond 0.25 F/F.U. ($12.5\% < x < 100\%$), we find a single two-phase region of coexisting O3-$Y_2CF_{0.25}$ and T1-Y_2CF_2. Interestingly, the H1-3 host lies above the convex hull at all concentrations of fluorine, meaning that it is less stable than the two-phase mixture.

We can also examine the metastable intermediates in addition to the ground state structures. Metastable intermediates are known to contribute to the kinetics of charge and discharge in experimental studies[14,15]. At all compositions from zero fluorination to complete fluorination, the formation energies for some metastable intermediates are low, even near kT at room temperature. As an example, at 1 F/F.U. an H1-3 intermediate is only 22 meV/F.U. above the hull. This single-phase non-equilibrium path of fluorine intercalation through metastable intermediates involves topotactically related phases with minimal

difference in lattice constants and is kinetically accessible. This suggests that fluorine insertion through intermediate Y_2CF_x structures is possible with minimal input of energy or overpotential. Importantly, a single-phase transformation bypasses the extra kinetic barriers of nucleation and growth that are required for a two-phase transformation. This feature has important ramifications for battery performance and has been used to explain why $LiFePO_4$ functions as an electrode with high rate-capability[16].

Our discovery that fluorine intercalation in Y_2C has a kinetically accessible solid-solution path should facilitate optimization of battery performance and experimentation. First, it suggests that particle size will play an important role in the charge/discharge process of Y_2C. Nanosizing particles tends to increase the solubility limits of the two phases whereas larger particles tend to facilitate phase separation [17]. Like nanosized $LiFePO_4$ or other two-phase ground-state intercalation systems, we expect smaller particles of Y_2C to exhibit faster kinetics and achieve better rate-capabilities than large particles. Secondly, while fluorine intercalation may proceed through a single-phase transformation, the ground state consists of two phases. A partially charged electrode at rest will relax to the ground-state and under ex-situ observation the particles will appear only as ground-state structures. This has been observed in similarly behaving Li-ion electrodes[18]. Therefore, ex-situ TEM and XRD will reveal a mixture of O3-Y_2CF_x ($0<x<0.25$) or fully fluorinated T1-Y_2CF_2, but this should not be taken as evidence that the (de)intercalation involves a two-phase transformation. This study will be conducted in future work.

With the convex hull, we obtain a piecewise voltage profile by evaluating the equilibrium voltage between the adjacent phases that make up the hull. The voltage profile shows a multitude of voltage steps, with the small steps (<0.05 V) originating from the numerous shallow ground states at low F concentrations. Voltage steps are associated with single phase, ordered regions; however, we observe continuous ground-state orderings within the resolution of our Monte Carlo simulations. Therefore, given the small size of the voltage steps and differences in an experimental setting to the considerations of our calculations like temperature and kinetic effects, we expect that in experiment the voltage profile will vary smoothly between 0 and 0.4 F/F.U.

The dominant feature of the voltage curve, however, is the flat voltage plateau with fluorine intercalation beyond 0.4 F/F.U. accounting for 80% of the fluorination. This plateau owes to the two-phase

mixture of O3-$Y_2CF_{0.25}$ and T1-Y_2CF_2. A similarly large voltage plateau is well known for the lithium electrode materials $LiFePO_4$[19] and $Li_4Ti_5O_{12}$[20].

The second important feature of the voltage profile is the voltage itself. To yield a large cell voltage when paired with a cathode, ideally an anode material has a low reduction potential similar to that of lithium. In Y_2C, fluorination begins at 0.54 V vs. Li/Li+ and plateaus at 0.73 V vs. Li/Li+ resulting in an average voltage of 0.74 V vs. Li/Li+. While not as extreme as that of Li or LiC_6, the reduction potential of Y_2C is still very low, making it an excellent candidate as an anode in a FIB.

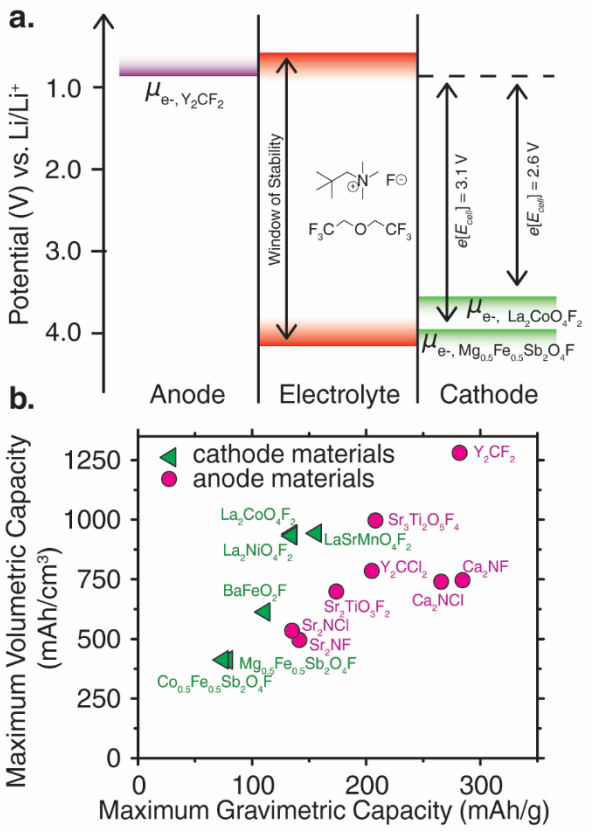


Figure 5 - 3: a) Potential diagram a F- battery with a Y_2CF_2 anode, a Np1F/BTFE liquid electrolyte, and intercalation-type cathodes (e.g. $La_2CoO_4F_2$ and $Mg_{0.5}F_{0.5}Sb_2O_4F$). The potentials for the cathodes are taken from reported DFT calculations[21]. b) Comparison of the gravimetric and volumetric capacities of the electrodes in this work and previously studied intercalation-type electrodes.

To put this voltage into context, it is useful to consider the cell voltage that could be expected from pairing the Y_2C anode with FIB cathode materials. In Figure 5-3a, we show a potential diagram of a F-battery utilizing Y_2C as an anode, with N,N,N-trimethyl-N-neopentylammonium fluoride (Np_1F) dissolved in blends of bis(2,2,2-trifluoroethyl)ether and tetraethylene glycol dimethyl ether as the electrolyte, and various candidate cathode materials. Np_1F is the best performing liquid electrolyte for F-ion batteries with high F-mobility and a large electrochemical window[22].

In addition to exploring the voltage, we plot the capacities of all the intercalation type electrodes studied for FIBs in Figure 5-3b. Y_2C, owing to its efficient atom economy, outperforms all the electrodes both in terms of gravimetric and volumetric capacities.

To perform as a battery system, the charge and discharge properties of layered electrides should be controllable and reproducible. To this end, we have completed rigorous electrochemical testing of the Y_2C/Y_2CF_2 system.

5.3.2 Electrochemical fluorination of Y_2C Electrodes

Electrochemical testing is conducted at most 2-days after electrode drying due to the high probability of electrode oxidation, even in an inert atmosphere. The oxidation of the electrode surface significantly increases the overpotential of the system, pushing the voltage outside of the stability window of the electrolyte, and decreasing overall phase conversion.

The charging curve is broken down into three main regions, as shown in Figure 5-4b. In region 1, we begin charging as the electrode interacts with the electrolyte. The voltage immediately drops, indicating instability at the electrode/electrolyte interface. We predict that the surface of the electride contains bare electrons that are highly reducing. As the fluoride salt runs into the reducing surface, the surface electron exchanges for the weakly bound fluoride and leaps into the lattice. Indeed, these predictions are supported by various reports of highly reducing bare electron models[23,24]. As shown in the voltage curve, this hypothetical reaction is energetically favorable, as evidenced by a significant drop in voltage. The hypothesis is also supported by XRD of samples subjected to open-circuit potential experiments, revealing up to 46% phase conversion upon submersion for 23hrs (Figure A5-2).

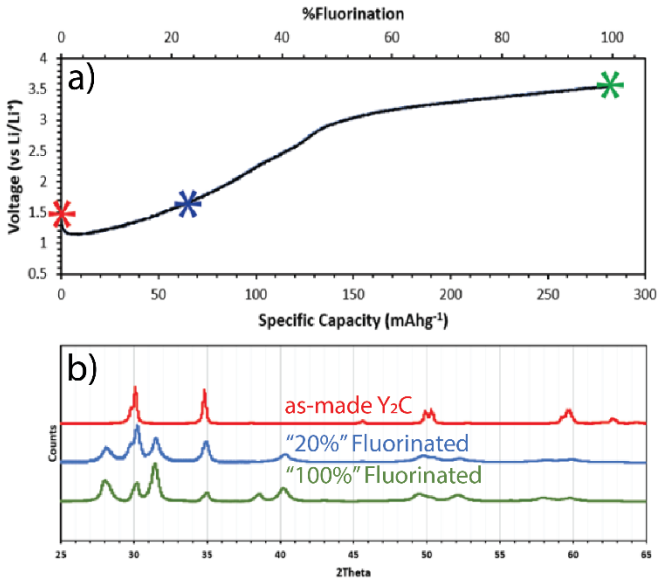


Figure 5 - 4: Experimental and computational demonstration of layered-Y_2C charging. A) Cluster expansion calculation showing the phase change from layered-Y_2C (AB stacked) to Y_2CF_2 (AA Stacked) at 25% charge. B) Experimental charging curve during a chronopotentiometry experiment, showing 3 distinct regions highlighted with a red star, blue star, and green star. C) XRD patterns at the associated stars, highlighting a single phase change from Y_2C to Y_2CF_2.

The second region is the charging curve predicted by calculations. The curve has a slope that increases as a function of capacity. This voltage is quite typical for a battery system with a single-phase transition. The slope is expected to remain constant while fluorine intercalates into a single phase, until a concentration reaches a point such that the system converts from Y_2C to Y_2CF_2. Note that the slope is larger than the predicted voltage. The discrepancy can be explained by various competing factors. 1) impedance caused by phase transitions into insulating Y_2CF_2, and 2) the decomposition of the electrolyte, causing impedance across the cell and increasing the voltage. Decomposition leads into region 3, where the curve plateaus. Through XRD, we find that the phase transition at the endpoint (fully charged to 282mAh/g) and at the bend (150mAh/g) are mostly the same, reaching a comparable charging capacity of nearly 80% conversion (220mAh/g) over 23hrs (Figure 5-4b). We expect the discrepancy between the charging curves and shown phase transition caused by significant passive fluorination during charge. The bend indicates not a phase transition in the Y_2C/Y_2CF_2 system, but a current caused by faradaic processes during electrolyte decomposition.

The interaction between the electrode and electrolyte is believed to hinder the charging and reversibility of electride electrodes. Even at a "fully charged" state, the electrodes do not undergo discharge to any extent upon current inversion. Therefore, we predict that the surface of the electrode becomes saturated in a non-passivating solid-electrolyte interphase (SEI).

A possible route to overcome solid-electrolyte interactions is to create an artificial barrier that improves stability and passivation. Artificial SEIs are beneficial over natural SEIs because the natural SEI forms using environmental constituents, i.e., lithium in LIBs or fluorine in FIBs. Therefore, over time, the capacity fades as the concentration of charge carriers decreases. Additionally, artificial SEIs benefit the cell by protecting the bare electrode from corrosive impurities in the electrolyte. Therefore, creating an electrochemical cell configuration that actively decreases interactions between electrolyte and electrode is crucial.

5.4 Conclusions

In the field of fluoride-ion batteries, introducing Y_2C as a champion anode is a major step forward. Y_2C is promising by every metric. Its maximum capacity is the highest reported for any intercalation-type FIB electrode. Its reduction potential is low, nearly as low as it can be while being in the electrochemical stability window of F-ion liquid electrolytes. Its combination of a very small change in volume upon intercalation coupled with its solid-solution intercalation path may suggest that it will offer good cyclability. Together, this suggests that just as graphite is the champion anode for LIBs that Y_2C will be the champion anode for FIBs.

Layered electrides in fluoride ion batteries may unlock high-capacity cells with long cycle stability. Interestingly, layered Y_2C electrides can store two fluorides in every unit cell, giving batteries twice the volumetric capacity compared to state-of-the-art lithium-based cells. Combined with a CuF_2 cathode, these cells could reach 2.8 volts. Furthermore, the realization of redox-less electron-anion exchange under electrochemical manipulation has exciting implications for understanding energy transfer mechanisms. Our calculations show that EAX occurs without significant lattice expansion or contraction, often leading to electrode degradation over time.

REFERENCES

1. Nowroozi, M. A. & Clemens, O. Insights on the Behavior of Conversion-Based Anode Materials for Fluoride Ion Batteries by Testing against an Intercalation-Based Reference Cathode. *ACS Appl Energy Mater* **1**, 6626–6637 (2018).

2. Nowroozi, M. A., Wissel, K., Rohrer, J., Munnangi, A. R. & Clemens, O. LaSrMnO4: Reversible Electrochemical Intercalation of Fluoride Ions in the Context of Fluoride Ion Batteries. *Chemistry of Materials* **29**, 3441–3453 (2017).

3. Nowroozi, M. A. *et al.* Fluoride ion batteries – past, present, and future. *J Mater Chem A Mater* **9**, 5980–6012 (2021).

4. Wissel, K. *et al.* Developing intercalation based anode materials for fluoride-ion batteries: topochemical reduction of Sr2TiO3F2via a hydride based defluorination process. *J Mater Chem A Mater* **6**, 22013–22026 (2018).

5. Wissel, K. *et al.* Topochemical Fluorination of La2NiO4+d: Unprecedented Ordering of Oxide and Fluoride Ions in La2NiO3F2. *Inorg Chem* **57**, 6549–6560 (2018).

6. Tojigamori, T. *et al.* Fluorination/Defluorination Behavior of Y2C in Fluoride-Ion Battery Anodes. *ACS Appl Energy Mater* **7**, 1100–1108 (2024).

7. Druffel, D. L. *et al.* First-Principles Prediction of Electrochemical Electron–Anion Exchange: Ion Insertion without Redox. *J Phys Chem Lett* **11**, 9210–9214 (2020).

8. Kresse, G. & Furthmüller, J. Efficient iterative schemes for ab initio total-energy calculations using a plane-wave basis set. *Phys Rev B* **54**, 11169–11186 (1996).

9. Blöchl, P. E. Projector augmented-wave method. *Phys Rev B* **50**, 17953–17979 (1994).

10. Perdew, J. P., Burke, K. & Ernzerhof, M. Generalized Gradient Approximation Made Simple. *Phys Rev Lett* **77**, 3865–3868 (1996).

11. Moellmann, J. & Grimme, S. DFT-D3 Study of Some Molecular Crystals. *The Journal of Physical Chemistry C* **118**, 7615–7621 (2014).

12. Chang, J. H. *et al.* CLEASE: A versatile and user-friendly implementation of Cluster Expansion method. (2018) doi:10.1088/1361-648X/ab1bbc.

13. Seko, A., Koyama, Y. & Tanaka, I. Cluster expansion method for multicomponent systems based on optimal selection of structures for density-functional theory calculations. *Phys Rev B* **80**, 165122 (2009).

14. Liu, H. *et al.* Capturing metastable structures during high-rate cycling of LiFePO4 nanoparticle electrodes. *Science (1979)* **344**, 1252817 (2014).

15. Hannah, D. C., Sai Gautam, G., Canepa, P. & Ceder, G. On the Balance of Intercalation and Conversion Reactions in Battery Cathodes. *Adv Energy Mater* **8**, 1800379 (2018).

16. Malik, R., Zhou, F. & Ceder, G. Kinetics of non-equilibrium lithium incorporation in LiFePO4. *Nat Mater* **10**, 587–590 (2011).

17. Wagemaker, M. & Mulder, F. M. Properties and Promises of Nanosized Insertion Materials for Li-Ion Batteries. *Acc Chem Res* **46**, 1206–1215 (2013).

18. Delmas, C., Maccario, M., Croguennec, L., Le Cras, F. & Weill, F. Lithium deintercalation in LiFePO4 nanoparticles via a domino-cascade model. *Nat Mater* **7**, 665–671 (2008).

19. Padhi, A. K., Nanjundaswamy, K. S. & Goodenough, J. B. Phospho-olivines as Positive-Electrode Materials for Rechargeable Lithium Batteries. *J Electrochem Soc* **144**, 1188 (1997).

20. Deschanvres, A., Raveau, B. & Sekkal, Z. Mise en evidence et etude cristallographique d'une nouvelle solution solide de type spinelle Li1+xTi2−xO4 $0 \leqslant x \leqslant 0$, 333. *Mater Res Bull* **6**, 699–704 (1971).

21. Hartman, S. T. & Mishra, R. Layered electrides as fluoride intercalation anodes. *J Mater Chem A Mater* **8**, 24469–24476 (2020).

22. Davis, V. K. *et al.* Room-temperature cycling of metal fluoride electrodes: Liquid electrolytes for high-energy fluoride ion cells. *Science (1979)* **362**, 1144–1148 (2018).

23. Alpatova, N. M., Zabusova, S. E. & Tomilov, A. P. The Reduction of Organic Compounds by Solvated Electrons Generated Electrochemically. *Russian Chemical Reviews* **55**, 99 (1986).

24. Rybkin, V. V. Mechanism of Aqueous Carbon Dioxide Reduction by the Solvated Electron. *J Phys Chem B* **124**, 10435–10441 (2020).

CHAPTER 6: STRUCTURAL CHARACTERISTIZATION OF SURFACE ENGINEERED AIR STABLE Y_2C ELECTRIDE

Connor C. Slamowitz, Karen M. Ehrhardt, Tommi Aalto, Scott C. Warren

6.1 Introduction

The electrochemical interaction between electrode and electrolyte at their interface remains a key scientific research thrust in battery materials science[1]. A delicate balance between stability and degradation profoundly affects battery performance. For instance, chemical reactions between the electrode and electrolyte can cause self-discharge[2,3], metal dissolution[4], and ion-passivating films[5]. However, in positive cases, reactions cause mechanical stabilization[6–8], solid-electrolyte interphases[9–11], and self-limited degradative passivation[1,12]. Therefore, the careful design and integration of solid-electrolyte interphases (SEIs) into batteries provides a basis for stable cycling of electrochemical systems.

SEIs are extremely useful in cases where the electrode is unstable under electrochemical conditions in electrolyte[1]. In the case of the layered Y_2C electride, high-energy electrons that exist as anionic electrons within the crystal lattice are highly reducing[13]. Thus, the incorporation of Y_2C as electrodes for fluoride-based batteries is technically difficult. The difficulty is amplified by the lack of large stability-windowed electrolytes that can conduct fluoride at room temperature[14]. Recently, Davis et al. developed a liquid electrolyte that has a 3.1V stability window and fast ion conductivity at room temperature: Np1F[4]. Unfortunately, this electrolyte still reacts when put in contact with Y_2C based electrodes.

By using heuristics developed by decades of lithium-ion battery technology, one can imagine a way to stabilize the highly reducing Y_2C electrode to enable stable cycling within full battery cells. In most commercial LIB cases, the SEI is a natural degradation product as the electrode reacts with the electrolyte[15]. Unfortunately, Davis et al. noted that the Np1F electrolyte degrades into bifluorite and hydrofluoric acid[16], etching metallic electrodes and significantly harming electrode performance. Thus, developing an intentional, artificial solid-electrolyte interphase would be ideal for our system. Indeed, to enhance performance, Davis integrated a lanthanum fluoride artificial SEI to increase stability[4]. For Y_2C, an alternative SEI is needed due to its reaction with water in aqueous synthetic conditions.

In this chapter, we have designed and optimized surface coatings to create a barrier between the high energy Y_2C electrons and the electrolyte. This coating must physically separate the electride electrons from our electrolyte while maintaining the ability for fluoride to move into Y_2C during electrochemical fluorination. Sulfur was hypothesized to be an ideal candidate for coating for multiple reasons; the ionic radius of sulfur is larger than oxygen, thus decreasing the likelihood of fast sulfur intercalation, and sulfur is a single element, creating an ideal model system for computational and experimental analysis. To this end, I refined an experimental process to successfully apply a sulfur coating to yttrium surfaces through furnace-based gas phase powder deposition.

6.2 Methods

6.2.1 Synthesis of Y_2C

Cleaned yttrium was reacted with a pressed pellet of graphite in a 2:1 Y:C stoichiometry with a high-voltage, tungsten-inert-gas (TIG) welding setup. The sample was arc welded at a current of 150 A, flipped over, and welded again. This process was repeated 4 times. The synthesis of the layered Y_2C phase was confirmed via PXRD.

6.2.2 Synthesis of Sulfur Coated Y_2C

Y_2C was first ground into a fine powder using a mortar and pestle. The Y_2C was moved into the bottom of a 15mL Swagelok high temperature reaction vessel constructed of 316L stainless steel parts. Pure sulfur (Sigma-Aldrich) was placed into the end of a borosilicate glass centrifuge tube. This tube was cut to about 2 cm in length in order to fit into the barrel of the reaction vessel. The elemental sulfur in the glass tube was placed over the Y_2C powder. Then, the end cap of the Swagelok cell was screwed into place and tightened using a wrench. The reaction vessel was then placed in a furnace, careful not to invert or spill the sulfur, at elevated temperatures until reaction was complete.

6.2.3 X-ray diffraction

All analyses were performed under inert atmosphere except for studies of sample oxidation. Electrode composites were characterized by powder x-ray diffraction (PXRD) at room temperature in a Bragg-Brentano geometry across a range of 20−70° 2-theta using Cu Kα (λ= 1.54056 Å) in a Rigaku Smartlab diffractometer. Both Y_2C and S@Y_2C were covered with Kapton tape to keep the sample air-free.

Oxidation studies were performed in the same XRD optical geometry with no Kapton covering over 45 minutes with each scan lasting 5 minutes.

6.2.4 Transmission Electron Microscopy

Samples for transmission electron microscopy (TEM) and scanning transmission electron microscopy (STEM) were prepared by drop-casting chemically fluorinated S@Y_2C powder in anhydrous toluene on a standard Cu mesh grid with lacey carbon. Samples were dried under vacuum and sealed under Ar for transport. These samples were loaded into a Thermo Scientific Talos F200X TEM with an accelerating voltage of 200 keV. Selected area electron diffraction was collected with a 20 μm selected area aperture and STEM-EDS was performed with a 7-nm condensed beam. The images and diffraction patterns were analyzed using Gatan Digital Micrograph version 3.

6.2.5 Chemical Fluorination

Chemical fluorinations proceeded inside an Ar-filled glovebox with < 1 ppm O_2 and H_2O. First, as-made Y_2C was ground into a coarse powder using an agate mortar and pestle.

A sand bath was heated on a hot plate until a stable temperature of 115 ^oC was achieved as measured by an alcohol thermometer. Y_2C (200 mg) was placed in the bottom of an HDPE bottle. A quantity of XeF_2 to yield a 1.5 XeF_2:Y_2C molar excess was placed in an HDPE bucket and suspended from the cap of the HDPE bottle containing Y_2C. The cap was screwed onto the bottle and the assembly was placed into a pre-heated sand bath to react for 2 hours.

6.3 Results and Discussion

6.3.1 Structural Characterization of Surface Coating

XRD revealed that the composition of the resulting powder diffracts Y_2C planes when heated to 350^oC for 24 hours. Past 350^oC, Y_2S_3 crystals begin to nucleate, resulting in characteristic peaks in XRD. Thus, further reactions were performed at or below 350^oC. As no discernable peaks were identified, the interphase is assumed to be amorphous.

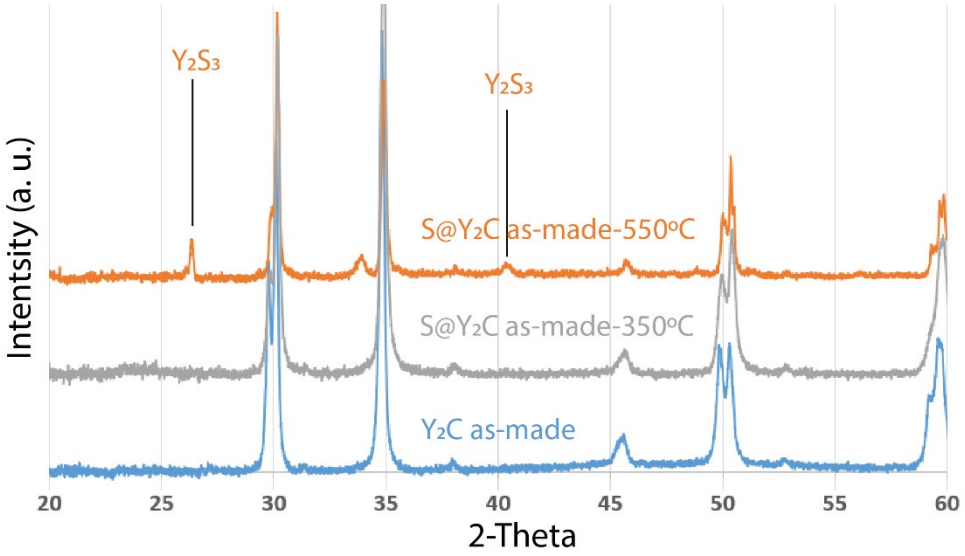
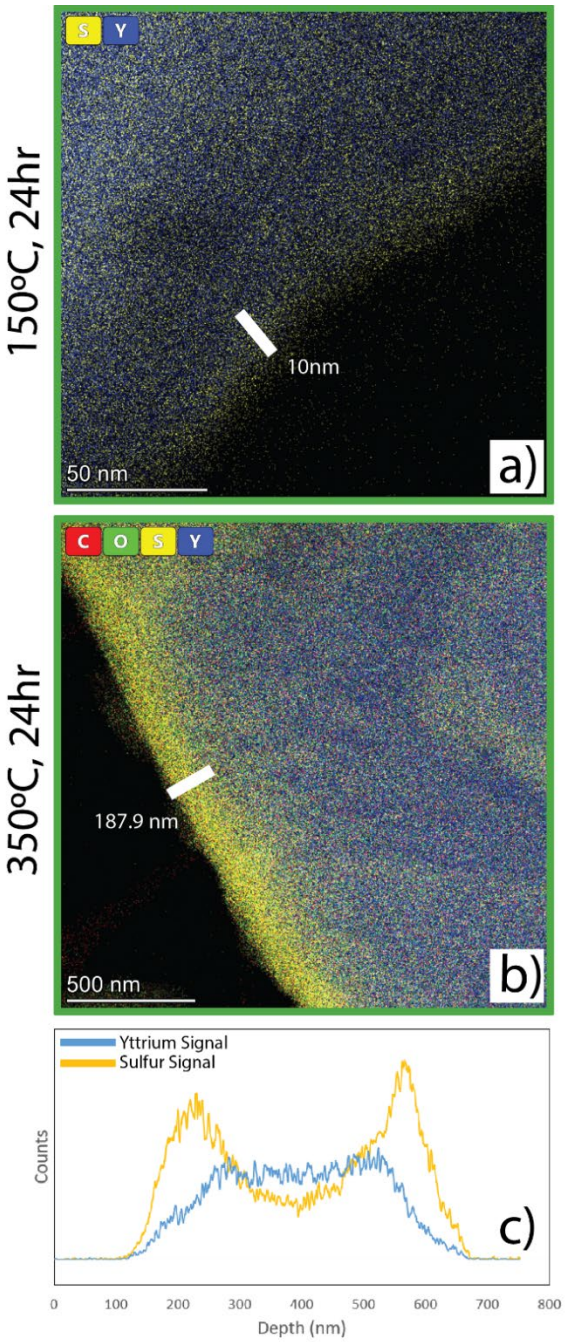


Figure 6 - 1: XRD of the synthesized S@Y_2C material. As evidence from comparing as made Y_2C and S@Y_2C synthesized at 350°C, no new phases appear. However, as the temperature increases to 550°C for 24hr, we see the growth of peaks associated with Y_2S_3.

To understand the interaction between vaporous sulfur and Y_2C, I performed transmission electron microscopy (TEM). Energy dispersive spectroscopy (EDS) depth mapping revealed characteristic core-shell morphology, with sulfur-to-yttrium ratios increasing at particle edges and decreasing dramatically towards the particle core (Figure 6-2c). Furthermore, depth mapping revealed a surface stoichiometry close to the yttrium sulfide (Y_2S_3) phase. However, electron diffraction in the TEM indicated that this coating was amorphous, supporting evidence observed in XRD.



By decreasing the reaction temperature, I hypothesized that the growth of the sulfur phase towards the core can be slowed. I performed new experiments at 350°C, 275°C, 200°C, and 150°C and analyzed the amorphous surface coating in TEM (Figure 6-2b). I found that this hypothesis was essentially correct – as temperature decreased, the growth was slowed, resulting in surface coatings that varied between 10nm and 200nm (Figure 6-2a-b). These results indicate that I will be able to control the shell thickness, an important property for SEIs that conduct fluoride yet resist electrons.

These experiments were repeated with a sample of Y_2C that was purposely synthesized in the disordered cubic phase, in which the carbon sites are disordered into the interlayer space of the layered Y_2C. Upon repeating the sulfidation, we found that sulfur did not coat cubic-Y_2C in the same way that it coated layered-Y_2C. These initial results hint at a mechanism for coating formation; the sulfur is reduced by the Y_2C, then slowly intercalates into the interlayer space, disorders

Figure 6 - 2: Energy Dispersive Spectroscopy mapping of Transmission Electron Microscopy images for sulfur coated Y_2C reacted at 150°C for 24hrs (a) and 350°C for 24hrs (b). Yellow indicates spectroscopic identification of sulfur, blue indicates spectroscopic identification of yttrium. We performed a depth analysis of the EDS signal (c) to show the exceptional core shell morphology of the sulfur-coated Y_2C particles. The stoichiometry of the sulfur to yttrium is ~2 parts yttrium to ~3 parts sulfur at the shell, decreasing in the particle, and increasing again.

the Y_2C phase into an amorphous Y_2S_3 mixed with an amorphous carbon phase, and grows toward the core. If there are nonviable pathways for the sulfur to diffuse (ie pathways in cubic-Y_2C) a surface coating is unachievable. These results indicate a kinetic model for the amorphous sulfur-yttrium coating.

6.3.2 Stability in Air

To observe the passivating nature of the sulfur coated electride, I exposed the electride and sulfur coated electride to air and monitored the change in structure with XRD. Pure layered Y_2C began to degrade in just 5 minutes as indicated by peak broadening (Figure 6-3a). After 10 minutes, the peaks at 29.7 2θ and 49.7 2θ begin to disappear. After 20 minutes, a broad peak at 31.5 2θ begins to grow in. This indicates a degradation mechanism in which oxygen is reduced at the surface of the electride and begins to move into the interlayer space of the electride. This disorders the interlayer space, resulting in the breakdown of the *00l* family of planes. As this process progresses, the yttrium further oxidizes and forms Y_2O_3. Finally, as all Y_2C is degraded, broad, amorphous Y_2O_3 forms mixed with amorphous carbon (Figure A6-4a).

In contrast, I found the sulfidated samples maintained the crystalline Y_2C phase while exposed to air for up to a full week (Figure A6-4b). This, in conjunction with the TEM EDS data, indicates that there could be a uniform, amorphous, and passivating surface coating on the surface of Y_2C after sulfidation. As the coating is passivating to oxygen, it is possible that the coating could also passivate Y_2C to fluoride in our electrolyte.

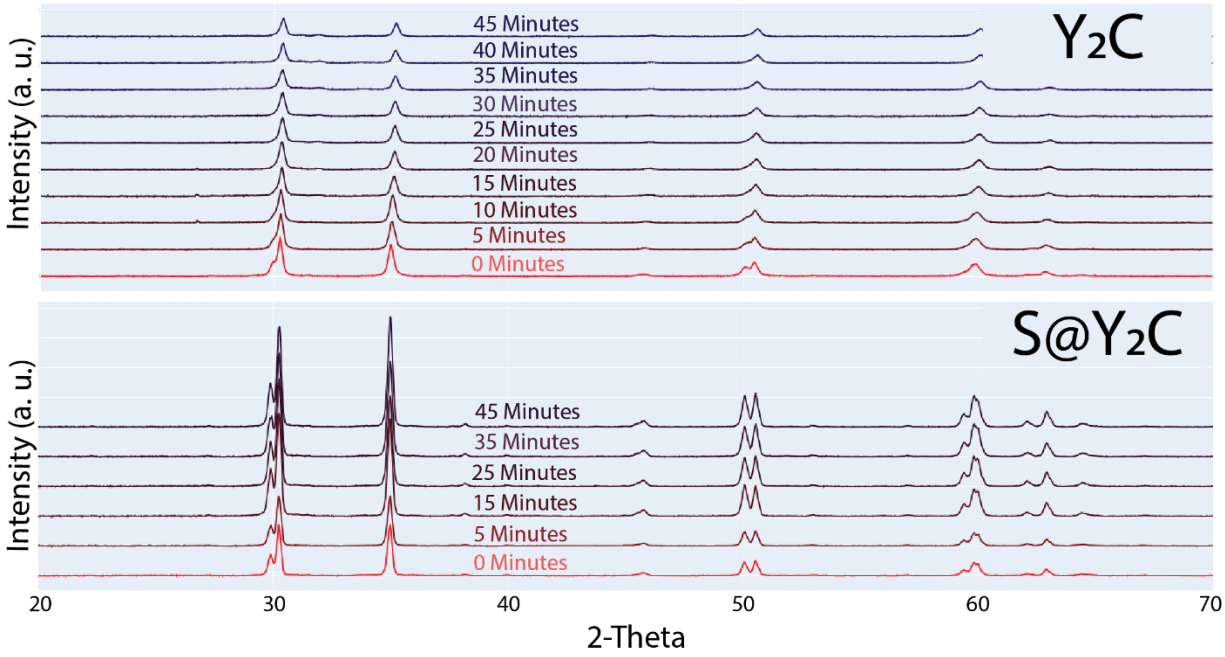


Figure 6 - 3: Time-resolved XRD of Pure Y_2C (top) and sulfur coated Y_2C ($S@Y_2C$, bottom). For Y_2C (top), we observed the growth of graphite peaks at 27 2θ as the 00l planes (29.7 2θ & 49.7 2θ) begin to disorder as oxygen diffuses into the interlayer spacing of Y_2C. We also observe polycrystalline/amorphous Y_2O_3 phase begin to grow after 20 minutes at ~32.0 2θ.

6.3.3 Fluorination Dynamics

For the sulfidated Y_2C samples, my goal is to incorporate the materials with fluoride containing electrolytes. Previous experiments show that pure Y_2C spontaneously reacts with all fluoride electrolytes that we have tested thus far. Initial testing of the sulfur coated Y_2C, however, indicates that the surface coating is passivating to fluoride, as indicated by moderate temperature exposure to gaseous XeF_2.

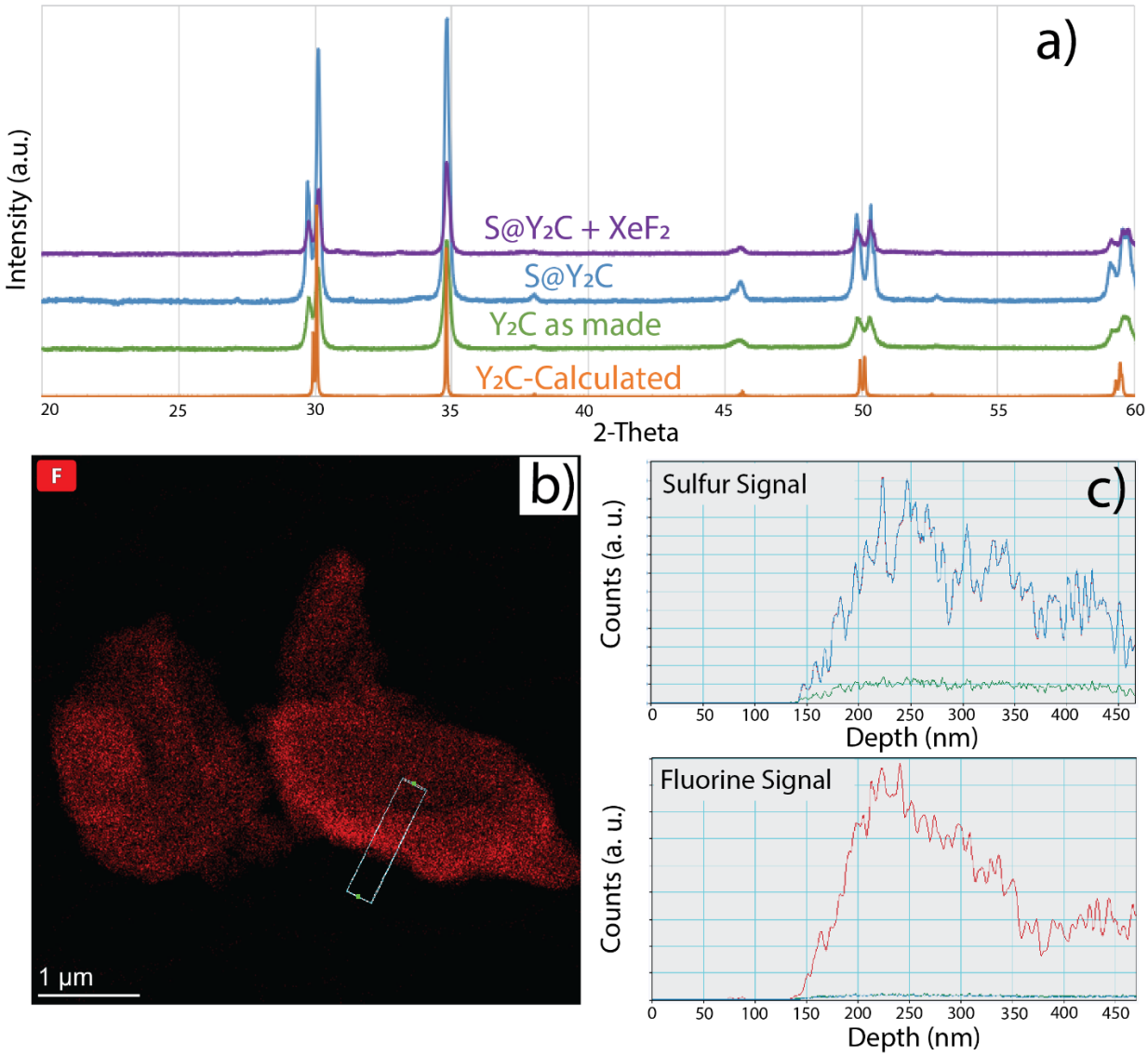


Figure 6 - 4: a) Structural characterization of as-made Y_2C, S@Y_2C and S@Y_2C fluorinated with gaseous XeF_2 using XRD result in no structural modification of the material. However, b) EDS mapping of samples collected in TEM reveals significant fluorine. Using c) depth profiling, we show that the fluoride is trapped in the amorphous sulfur-yttrium shell, creating a new amorphous Y-S-F passivating shell.

By exposing S@Y_2C to XeF_2, we found that there was no conversion to the expected Y_2CF_2 phase in the $\boldsymbol{P\bar{3}m1}$ space group (Figure 6-4a). Indeed, we see no change in the phase of the material, with diffraction peaks only observed for Y_2C across all processing steps.

To further understand the structure, we performed TEM-EDS mapping of the post-fluorinated S@Y_2C sample. We found that particles exposed to XeF_2 gas formed a mixed Y-S-F shell (Figure 6-4b). This shell was amorphous due to the lack of diffraction signal from the surface coating. By analyzing the depth profile of the coating across the particle, we found that the Y-S coating inhibits the diffusion of fluoride through the surface coating and into the Y_2C core - effectively passivating the underlying Y_2C to fluorine. Thus, we hypothesize that the coating may be passivating to electrolytes as well. My next steps will be to test the electrochemical performance of the sulfur coated Y_2C. By controlling the surface coating thickness, I can test my battery in a variety of chemical environments and temperatures.

I aim to continue to conduct high-temperature battery operation experiments at the University of Stuttgart and UNC-Chapel Hill. Stuttgart is an international hub for battery research, and I will have access to experts who can advise optimal procedures for battery fabrication, such as controlling electrode composition and further mitigating unwanted side reactions. I aim to explore long-term battery performance and examine any degradation mechanisms.

6.4 Conclusion

In this chapter, we present a vapor-deposition method for coating highly reactive electride powders. Using this method, we exposed the Y_2C electride to vaporous sulfur in a confined Swagelok reaction vessel. By tuning the temperature and time of the reaction, we were able to create shells with varying thicknesses and crystallinity. Exposing these core-shell particles to air revealed the passivating nature of the sulfur-coated particles – surprisingly, there was no degradation of the Y_2C electride when exposed to air even up to a full week. This passivating property of the amorphous yttrium-sulfur shell extended to fluorine. When exposed to fluorine gas, no conversion to Y_2CF_2 is observed and find that the fluoride is trapped in the sulfur coating. These experiments provide a strong baseline for further experimentation in electrochemical environments. Given a thin enough shell and a high enough potential, we predict that we can overcome the diffusion barrier for fluoride mobility through the shell, creating a strong SEI for long-term battery operation.

REFERENCES

1. *Lithium-Ion Batteries*. (PUBLISHED BY IMPERIAL COLLEGE PRESS AND DISTRIBUTED BY WORLD SCIENTIFIC PUBLISHING CO., 2004). doi:doi:10.1142/p291.

2. Ike, I. S., Sigalas, I. & Iyuke, S. Understanding performance limitation and suppression of leakage current or self-discharge in electrochemical capacitors: a review. *Physical Chemistry Chemical Physics* 18, 661–680 (2016).

3. Merrill, L. C., Rosenberg, S. G., Jungjohann, K. L. & Harrison, K. L. Uncovering the Relationship between Aging and Cycling on Lithium Metal Battery Self-Discharge. *ACS Appl Energy Mater* 4, 7589–7598 (2021).

4. Davis, V. K. *et al.* Room-temperature cycling of metal fluoride electrodes: Liquid electrolytes for high-energy fluoride ion cells. *Science (1979)* 362, 1144 (2018).

5. Montesperelli, G., Nunziante, P., Pasquali, M. & Pistoia, G. Li passivation in different electrolytes during storage and cycling — An impedance spectroscopy study. *Solid State Ion* 37, 149–156 (1990).

6. Nitta, N., Wu, F., Lee, J. T. & Yushin, G. Li-ion battery materials: present and future. *Materials Today* 18, 252–264 (2015).

7. Itou, Y. & Ukyo, Y. Performance of LiNiCoO2 materials for advanced lithium-ion batteries. *J Power Sources* 146, 39–44 (2005).

8. Bloom, I. *et al.* Effect of cathode composition on capacity fade, impedance rise and power fade in high-power, lithium-ion cells. *J Power Sources* 124, 538–550 (2003).

9. "Delahay, P. & "Tobias, C. W. *Advances in Electrochemistry and Electrochemical Engineering. Volume 8. Electrochemical Engineering*. (Wiley. Interscience,Chichester, Sussex, England, United Kingdom, 1971). doi:https://doi.org/.

10. Dey, A. N. & Sullivan, B. P. The Electrochemical Decomposition of Propylene Carbonate on Graphite. *J Electrochem Soc* 117, 222 (1970).

11. Peled, E. Film forming reaction at the lithium/electrolyte interface. *J Power Sources* 9, 253–266 (1983).

12. Kanamura, K., Tamura, H., Shiraishi, S. & Takehara, Z. Morphology and chemical compositions of surface films of lithium deposited on a Ni substrate in nonaqueous electrolytes. *Journal of Electroanalytical Chemistry* 394, 49–62 (1995).

13. Zhang, X. *et al.* Two-dimensional transition-metal electride Y2C. *Chemistry of Materials* 26, 6638–6643 (2014).

14. Nowroozi, M. A. *et al.* Fluoride ion batteries - past, present, and future. *Journal of Materials Chemistry A* vol. 9 5980–6012 Preprint at https://doi.org/10.1039/d0ta11656d (2021).

15. Fong, R., von Sacken, U. & Dahn, J. R. Studies of Lithium Intercalation into Carbons Using Nonaqueous Electrochemical Cells. *J Electrochem Soc* 137, 2009–2013 (1990).

16. Davis, V. K. *et al.* Fluoride-ion solvation in non-aqueous electrolyte solutions. *Mater Chem Front* 3, 2721–2727 (2019).

CHAPTER 7: AMORPHOUS METAL SUBCARBIDE FLUORIDE FOR HIGH-PERFORMANCE FLUORIDE-ION BATTERIES

Connor C. Slamowitz†, Tommi Aalto‡, Karen M. Ehrhardt†, Oliver Clemens‡, Scott C. Warren†

†Department of Chemistry, The University of North Carolina, Chapel Hill, North Carolina 27514, United States.

‡Institute for Materials Science, Materials Synthesis Group. University of Stuttgart, Heisenbergstraße 3, 70569 Stuttgart (Germany).

7.1 Introduction

The transition toward a sustainable energy landscape relies on the development of high-capacity, long lifetime batteries to store renewable energy. Among the promising new technologies explored, fluoride-ion batteries (FIBs) are emerging as lithium alternatives that provide large energy densities driven by large voltages[1]. However, the development of cyclable fluoride electrodes that operate with high capacities is still necessary to reach commercial viability.

Recent studies[2,3] have shown that the layered electride Y_2C is a promising material for high-capacity, large-voltage, fluoride-ion battery electrodes. Electrides are interesting materials because of their exotic electronic structure; the materials are so electron rich that electrons are ejected from the orbitals of cationic metals and localize within interstitials. The bare electrons effectively act as anions within the host lattice by providing electrostatic stabilization to nearby cations. In the electride Y_2C, which has a crystallographic space group of $R\bar{3}m$, these electrons localize in planes sandwiched between layers of yttrium and carbon[4]. Because $R\bar{3}m$ Y_2C is structurally related to many layered LIB electrodes and the thermodynamically stable halide analog Y_2CF_2 exists[5], we predicted that Y_2C could be fluorinated to form Y_2CF_2 under an electrochemical bias[6] given a fluoride source. These electrodes, although extremely exciting from a scientific standpoint, still face cycle stability issues in practice caused by parasitic side reactions resulting in the degradation of both the electrode and electrolyte[2,3].

In this study, we present a synthetic strategy that further increases the already large free volume of Y_2C, creating a three-dimensional (3D) transport network for fluoride while simultaneously reducing long-range order. We find that ball milling and electrochemical cycling irreversibly expand the material's volume by approximately 5%. Structural characterization via diffraction and hybrid reverse Monte Carlo reveals that Y_2C is partially amorphized and that Y_2CF_2 becomes fully amorphous. This structural change introduces an interconnected 3D transport network for fluoride. Despite the loss of crystallinity, electronic structure analysis revealed that some yttrium and carbon atoms occupy environments that are more electron rich than those in conventional electrides, suggesting the presence of solvated electrons within disordered Y_2C[7–10]. Notably, the disordered Y_2C electrode achieves high cycling stability and high capacities of up to 282 mAh/g. We propose that the high stability of the amorphous phase arises from these solvated electrons, which stabilize the large vacancies formed when fluoride departs. Moreover, the direct exchange of a solvated electron with a fluoride ion offers a low-activation energy pathway for the reversible conversion of disordered Y_2C to amorphous Y_2CF_2. This provides a material that achieves large capacities, high voltages, and negligible volume changes across many charge–discharge cycles.

7.2 Methods

7.2.1 Synthesis of Y_2C

We obtained yttrium from Strem Chemicals and graphite from Sigma–Aldrich. To remove oxygen from the as-received yttrium, 0.5 to 1 g pieces were arc-melted to create a smooth yttrium button. The buttons were sealed in a tantalum cylinder with 50 wt.% freshly dried YCl_3. The sealed tantalum tube was sealed in a quartz ampule under 10^{-2} mbar of pressure. The mixture was heated at 850 °C for 48 hrs. with heating and cooling rates of 2.3 °C/min., yielding YOCl on the surface of the yttrium pellet. Within a glovebox, the excess YCl_3 and YOCl were removed from the material surface via a handheld electronic grinder (Dremel).

Cleaned yttrium was reacted with a pressed pellet of graphite in a 2:1 Y:C stoichiometry with a high-voltage, tungsten-inert-gas (TIG) welding setup. The sample was arc welded at a current of 150 A, flipped over, and welded again. This process was repeated 4 times. The synthesis of the layered Y_2C phase was confirmed via PXRD.

7.2.2 Fabrication of Electrodes

The $Ca_{0.5}Ba_{0.5}F_2$ solid electrolyte was synthesized by ball-milling equimolar amounts of CaF_2 and BaF_2 for 6 h at 600 rpm using 51 g of 5 mm ZrO_2 balls in a 50 ml ZrO_2 jar with isopropanol as a dispersing agent[11]. After ball milling, the isopropanol was evaporated, and the resulting powder was dried under vacuum at 170 °C for 15 h.

Y_2C was hand ground in an agate mortar. Copper was heated at 300 °C for 8 h in a flow of 5 % H_2 in Ar to remove surface oxides. Copper and Y_2C were ball milled in equal weight fractions for 10 h at 200 rpm using ten 10 mm ZrO_2 balls in a 50 mL ZrO_2 jar. Milling was conducted in an Ar atmosphere, and the jar was dried at 65 °C for at least 12 h before use.

The final electrode composite was obtained by ball-milling 3 parts of the Y_2C/Cu mixture with one part of the $Ca_{0.5}Ba_{0.5}F_2$ solid electrolyte for 2 h at 250 rpm with 10 pieces of 10 mm ZrO_2 balls in a 50 mL ZrO_2 jar. Milling was conducted under Ar after drying the jar and balls for at least 12 h.

A $Pb/PbF_2/C$ cathode composite was prepared by ball-milling 45 wt.% Pb, 45 wt.% PbF_2 and 10 % carbon black for 6 h at 600 rpm using 51 g of 5 mm ZrO_2 balls in 50 mL ZrO_2 in an Ar atmosphere. The composite was subsequently dried for 15 h at 170 °C under vacuum.

7.2.3 Electrochemical (de)fluorination

Electrochemical cells were manufactured by pressing 20 mg of $Pb/PbF_2/C$ composite and 4 mg of $Y_2C/Cu/Ca_{0.5}Ba_{0.5}F_2$ composite on either side of a 50 mg layer of $Ca_{0.5}Ba_{0.5}F_2$ solid electrolyte. The cells were placed in an airtight Ar-filled cell and heated to 170 °C for cycling.

7.2.4 Chemical Fluorination Reactions

Chemical fluorination proceeded inside an Ar-filled glovebox with < 1 ppm O_2 and H_2O. First, as-made Y_2C was ground into a coarse powder using an agate mortar and pestle. The material was transferred into a 2.5 mL stainless steel jar with one 6.35 mm stainless steel ball. The jar was closed with a Teflon O-ring and sealed with Kapton tape under Ar. The contents were ground using a Spex SamplePrep BM-400 Mixer/Mill in an Ar glovebox with a 10 min on/20 min off cycle for a total elapsed time of 72 hours.

A sand bath was heated on a hot plate until a stable temperature of 100 °C was achieved, as measured by an alcohol thermometer. Ball-milled Y_2C (200 mg) was placed at the bottom of an HDPE

bottle. A quantity of XeF_2 (Sigma) to yield Y_2CF_2 stoichiometrically was placed in an HDPE bucket and suspended from the cap of the HDPE bottle containing Y_2C. The cap was screwed onto the bottle, and the assembly was placed into a preheated sand bath to react for 100 hours.

7.2.5 Transmission Electron Microscopy and X-ray Diffraction

All analyses were performed under an inert atmosphere except for studies of sample oxidation. Electrode composites were characterized by powder X-ray diffraction (PXRD) at room temperature in a Bragg–Brentano geometry across a range of 20–70° 2-theta using Cu Kα (λ= 1.54056 Å) in a Rigaku Smartlab diffractometer. The amorphous Y_2CF_2 (aY_2CF_2) was covered with Kapton tape to keep the sample air-free, whereas the pristine and electrochemically treated electrode composites were measured in Rigaku airtight sample holders. The pattern was indexed and refined via Bruker Topas software.

After the initial ball milling, the ratio of crystalline to amorphous Y_2C was calculated from the Rietveld fit. This was accomplished by comparing the weight fractions of Y_2C and copper—derived from the integral intensity—while accounting for the scattering strength of each element.

Samples for transmission electron microscopy (TEM) and scanning transmission electron microscopy (STEM) were prepared by drop-casting chemically fluorinated aY_2CF_2 powder in anhydrous toluene on a standard Cu mesh grid with lacey carbon. The samples were dried under vacuum and sealed under Ar for transport. These samples were loaded into a Thermo Scientific Talos F200X transmission electron microscope (TEM) with an accelerating voltage of 200 keV. The selected area electron diffraction data were collected with a 20 μm selected area aperture, and STEM-EDS was performed with a 7-nm condensed beam. The images and diffraction patterns were analyzed via Gatan Digital Micrograph version 3.

7.2.6 Computational Analysis

Hybrid reverse Monte Carlo (HRMC) was performed to obtain an experimentally derived atomistic model of the aY_2CF_2 structure. Our custom HRMC code uses a Markov-chain Monte Carlo algorithm to fit the experimental pair distribution function and simultaneously minimize structural energy[12]. Our code uses an interface for energy calculations from the large-scale atomic/molecular massively parallel simulator[13]. A machine-learned force field for energy calculations of aY_2CF_2 was trained with FLARE[14] from DFT

calculations in VASP[15–17]. The DFT calculations used the PBE functional with a cutoff energy of 520 eV and a 2x2x2 k-point grid in a supercell of 180 atoms. The forcefield was trained to a cutoff radius of 5.0 Å with a Chebyshev basis and a quadratic cutoff function, with the error for training remaining below 0.01 eV/Å. HRMC was performed for 5.2 million steps on a cell of 1200 atoms with periodic boundary conditions. An initial temperature of 1000 K and an experimental error constant of 0.05 were used. These parameters were quenched as follows:

$$T_{n+1} = T_n \cdot q_T^n,$$

$$\sigma_{n+1} = \sigma_n \cdot q_\sigma^n,$$

where n is the step number, T is the temperature, σ is the experimental error constant, k_B is the Boltzmann constant, and q is a quenching rate of 0.9995.

Analysis of the coordination number distribution from the HRMC model was performed via the CrystalNN algorithm from PyMatGen[18].

7.3 Results and Discussion

7.3.1 Stable Cycling of Amorphous Electrodes

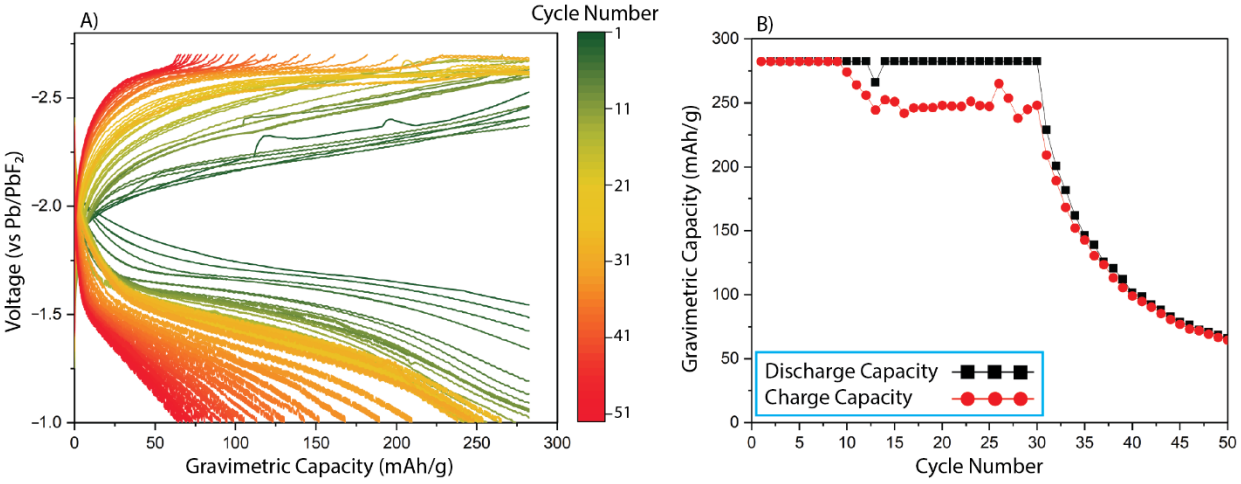


Figure 7 - 1: A) Cycling behavior of ball milled Y_2C electrodes reveals good cyclability at a theoretical capacity of 282 mAh/g for at least 10 cycles before overpotentials begin to build in the electrochemical cell. B) Discharge capacity and charge capacity show that the theoretical capacity

was reached for both cycles for 10 cycles. After 10 cycles, an 89% charge capacity was maintained, whereas a 100% discharge capacity was maintained. After 31 cycles, the capacity quickly decreased to 27% and was maintained until cycling was ended.

Previous reports have shown that ball milling Y_2C with $Ca_{0.5}Ba_{0.5}F_2$ led to degradation reactions[2]. Consequently, we first ball milled Y_2C with Cu powder (1:1 by weight) for 10 h at 200 rpm to aggressively reduce the particle size, followed by ball milling the resulting composite with $Ca_{0.5}Ba_{0.5}F_2$ for 2 h at 250 rpm. As the milling time increased, the progressive broadening of the XRD peaks signaled a decrease in the crystallite size (Figure A7-4).

We used the composite to form the anode of a battery with $Ca_{0.5}Ba_{0.5}F_2$ as the electrolyte and Pb/PbF_2 as the cathode and then cycled it until failure. During the first ten cycles, the Y_2C electrode was cycled 10 times to its full capacity of 282 mAh/g with minimal overpotentials. Afterward, its capacity decreased slightly and stabilized at 240 mAh/g for the next 30 cycles. Following this, the capacity decayed toward zero as cycling continued.

These results indicate a nearly 5-fold increase in the number of cycles relative to previous reports of the Y_2C/Y_2CF_2 system[2]. Thus, we sought to understand the effects of long ball milling times on the microstructure of the Y_2C composite and how its structure affects the cycle lifetime of the battery cell.

7.3.2 Identification of the Amorphous Phase in a Y_2C/Y_2CF_2 Electrochemical Cell

To understand the structure of the electrode upon electrochemical fluorination and defluorination, we performed PXRD. Surprisingly, upon the first discharge, we found that there was no detectable crystalline structure associated with the expected intercalated phase, Y_2CF_2 (Figure 7-2)[2]. This result is unlike previously reported Y_2C/Y_2CF_2 electrodes that remained crystalline[2,3], suggesting that the expected intercalated phase has been altered in important ways. Therefore, upon full discharge to 282 mAh/g, a new amorphous material with an approximate composition of Y_2CF_2 (yttrium subcarbide fluoride) was produced.

As shown in Figure 7-2, the amorphous yttrium subcarbide fluoride (aY_2CF_2), which was fabricated via ball milling and subsequent discharge of $Cu/Y_2C/Ca_{0.5}Ba_{0.5}F_2$, was able to recharge to the full capacity

of 282 mAh/g. Upon recharge, we identify previously unreported peaks at ~28.0 2-theta and ~33.0 2-theta. Rietveld analysis revealed a structural fit to the $R\bar{3}m$ Y_2C phase with a 5% expanded volume.

Since the reflections attributed to copper are sharp, it can be assumed that the copper remained crystalline throughout the ball milling process. The nominal weight ratio of 50 wt.% Cu:50 wt.% Y_2C is very well reflected in the XRD-calculated weight fractions of 52 wt.% Cu:48 wt.% Y_2C. For this comparison, the weight fraction of the electrolyte is neglected.

We observed that the intensity of the Y_2C peaks in the XRD pattern was lower than that of the original material prior to cycling. After electrochemical fluorination and subsequent defluorination, the weight fraction of Cu:Y_2C was 40:60, indicating that approximately one-third of the Y_2C remained amorphous after defluorination, resulting in total weight fractions of (33 wt.% crystalline Y_2C + 17 wt.% amorphous Y_2C):50 wt.% Cu. From these observations, we propose a model in which nanocrystals of volume-expanded Y_2C are surrounded by a matrix of amorphous Y_2C.

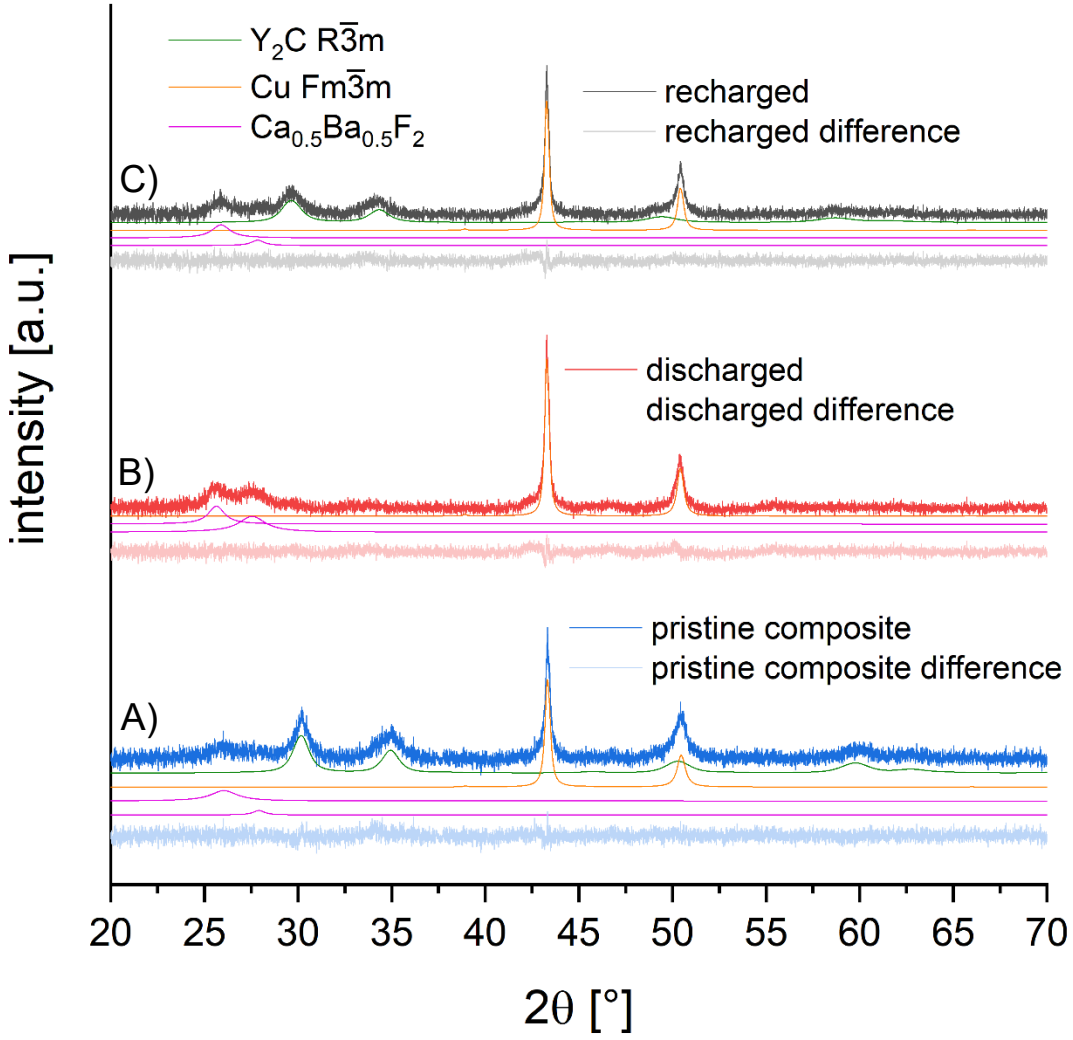


Figure 7 - 2: Behavior of the ball milled $Y_2C/Cu/Ca_{0.5}Ba_{0.5}F_2$ composite upon the first discharge/charge cycle. The first discharge achieves a reversible gravimetric capacity of 282 mAh/g. A) The pristine composite after ball milling shows distinct peaks for Cu, whereas the phases identified as YC and $Ca_{0.5}Ba_{0.5}F_2$ show decreased intensity and peak broadening. B) XRD after the discharge cycle to Y_2CF_2 provides evidence of an amorphous phase with no long-range ordering. C) Upon recharge, the Y_2C peaks shift to lower 2-theta angles, revealing an expanded electride.

7.3.3 Structural characterization of the amorphous fluorinated phase

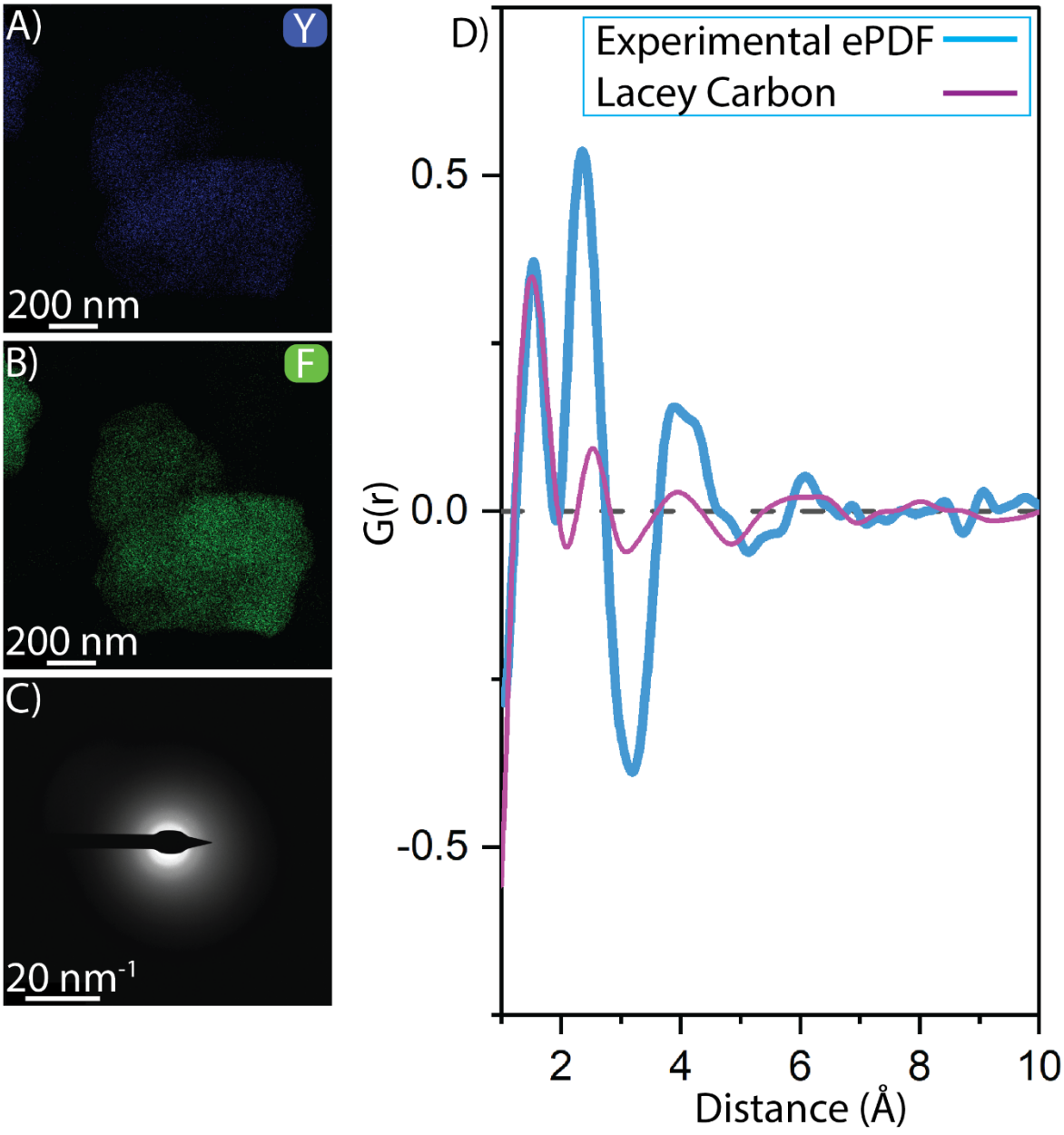


Figure 7 - 3: TEM–EDS mapping of the amorphous Y_2CF_2 material prepared via chemical fluorination with XeF_2, revealing A) Yttrium and B) fluorine signals at equal atomic concentrations. C) Electron diffraction image revealing diffuse rings with a noncrystalline morphology. D) The Fourier transform across the radial intensity map provides the electron pair distribution function (ePDF). The ePDF shows approximate coordination shells of 2.41 Å and 4.02 Å, corresponding to the approximate bonding of Y-F or Y-C and Y-Y, respectively. Bonding signals less than 1.91 Å are attributed to the signal of the lacey carbon grid used as the sample holder.

To understand the amorphous structure of this complex material system, we first ball-milled Y_2C and then chemically fluorinated it to produce amorphous Y_2CF_2. We utilized chemical fluorination rather than electrochemical fluorination to avoid contributions from either copper or $Ca_{0.5}Ba_{0.5}F_2$ in the analysis. The amorphous structure was confirmed by XRD analysis, which was consistent with the results of electrochemical cycling. STEM-EDS mapping revealed an average Y:F (at.%) ratio of 42:46 (Table A7-1), which is consistent with an overall composition of approximately Y_2CF_2. For these particles, diffuse scattering in the electron diffraction pattern indicated the presence of amorphous domains. The Fourier transform of the radial scattering intensity profile yields the electron pair distribution function (ePDF). This analysis shows four peaks indicating bonding coordination at 1.60 Å, 2.41 Å, 3.96 Å and 4.11 Å. At larger distances, long-range order is lost, as indicated by the absence of large peaks. The 1.60 Å shell does not share any corresponding bonding arrangement with Y_2CF_2. However, after taking the diffraction pattern of the amorphous lacey carbon grid used to support the fluorinated particles, we can identify this unknown peak as an overlapping signal from the carbon support. The peak at 2.41 Å corresponds to an approximate bonding distance with Y-F (2.41 Å) and Y-C (2.51 Å) bonds in the crystalline phase.

By integrating each peak, we can determine the approximate coordination numbers. The first coordination shell at 2.41 Å indicates 7 coordinating atoms, which is consistent with 3 fluorine atoms and 4 carbon atoms bonded to yttrium. The second coordination shell has maxima at 3.96 Å and 4.11 Å, which is similar to that found in crystalline Y_2CF_2 for the Y-Y distance (4.17 Å). This deviation indicates significant distortion from the crystalline material.

We used Hybrid Reverse Monte Carlo (HRMC) to model the structure of the aY_2CF_2 phase. As the HRMC proceeded, the mean square error (MSE) of the simulated fit decreased to 0.61, whereas the total enthalpy of the system decreased to 0.71 eV/atom above the hull of the thermodynamically stable Y_2CF_2 structure. Thus, the formation of the amorphous phase would only be possible if the defect energy was high. Given the extreme number of ball mills of the Y_2C structure, we conclude that ball milling causes extreme deformations that induce amorphous phase transitions. This finding is consistent with prior reports of ball mill-induced amorphization of other materials[19–23].

Interestingly, the HRMC fit reveals a quasilayered structure of aY_2CF_2. The distortion is quantified by comparing the coordination of yttrium, carbon, and fluoride in $P\overline{3}m1$ Y_2CF_2 versus aY_2CF_2. Moreover, HRMC and coordination analyses revealed distortion of the anion planes containing fluoride. This distortion was so large that it led to the migration of fluoride into the layer, which typically contains only carbon. These results indicate that the amorphization of Y_2CF_2 upon fluorination results in diverse fluoride diffusion pathways, even across layers, leading to improved kinetics across the nanoparticles of the electrode material.

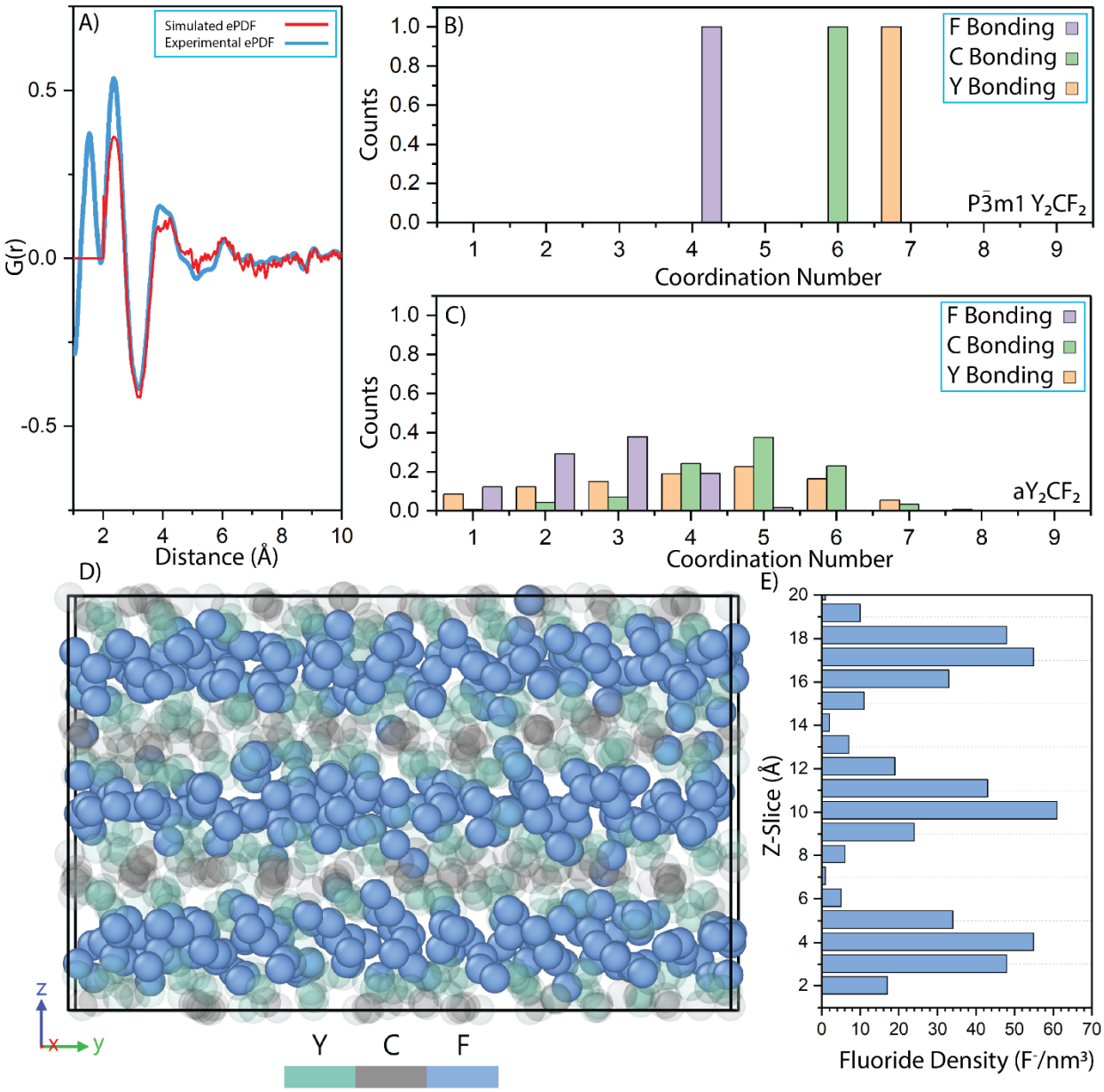


Figure 7 - 4: A) Using the experimental ePDF, we simulated the structure of amorphous Y_2CF_2 using Hybrid Reverse Monte Carlo. Using the simulated structure, a direct comparison of the coordination environment for B) crystalline Y_2CF_2 and C) amorphous Y_2CF_2 can be constructed. The fit reveals a D) general layered structure with E) expanded fluoride pathways bridged across the cationic framework.

7.3.4 Electronic Structure Characterization of Amorphous Fluorinated Phase

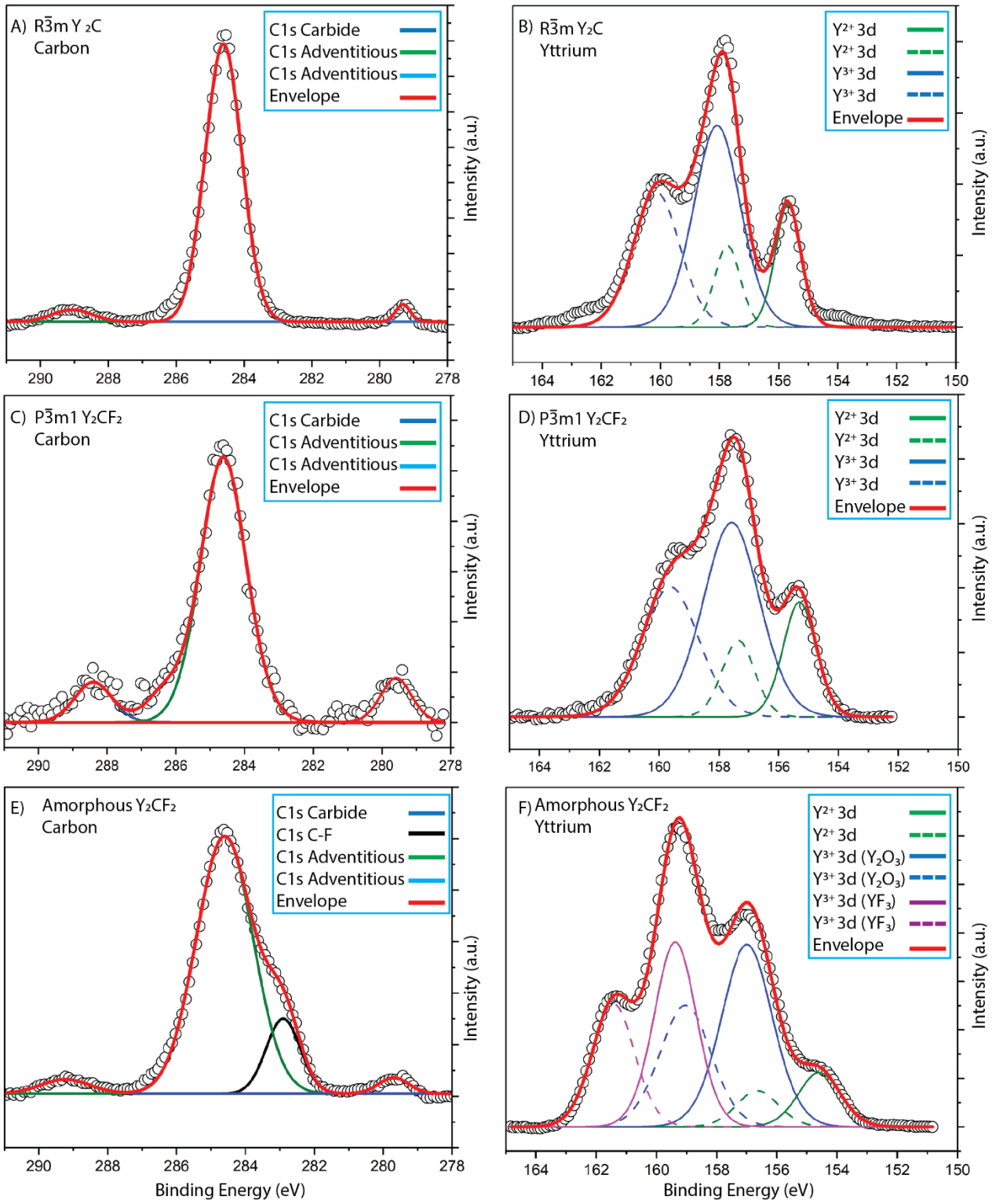


Figure 7 - 5: Background subtracted XPS measurements of a) $R\bar{3}m$ Y_2C carbon 1s binding energy, b) $R\bar{3}m$ Y_2C yttrium 3d binding energy, c) $P\bar{3}m1$ Y_2CF_2 [5] carbon 1s binding energy, d) $P\bar{3}m1$ Y_2CF_2 [5]

yttrium 3d binding energy, c) aY_2CF_2 carbon 1s binding energy, and d) aY_2CF_2 yttrium 3d binding energy.

Using X-ray photoelectron spectroscopy (XPS), we probed changes in the electronic structure of Y_2CF_2 at its surface upon amorphization. Compared with Y_2C or Y_2CF_2, aY_2CF_2 exhibited shifts in the spectrum, which is consistent with a unique and diverse electronic structure. First, the peak attributed to the highly reduced yttrium species shifted to an even more reduced state, with the leading peak at 154.6 eV. Fits for the oxide species also shifted to 157.0 eV, possibly indicating a unique coordination environment for the surface oxide. Compared with crystalline Y_2CF_2 and Y_2C, the amorphous structure exhibited a third novel peak at 159.4 eV. This peak most likely indicates surface fluorination, producing either a Y-O-F or YF_3 phase. Previously reported XPS spectra of common yttrium species show that Y^{3+} bonded to fluoride is more oxidized than Y-O species are, consistently shifting the spectra by 1–2 eV to higher binding energies. Indeed, YF_3 standards do show similar binding energies as the observed aY_2CF_2 spectrum (Figure A7-2a). Furthermore, argon ion sputtering, which is used to ablate surface oxides and adventitious carbon species, removes surface impurities, indicating that the bulk amorphous structure mainly consists of highly reduced yttrium species (Figure A7-2b).

Previous reports of Y_2CF_2[4] (Figure 7-5b) identified a characteristic Yttrium 3d 5/2 peak at a binding energy of 155.3 eV, which was a result of the yttrium being in an atypical 2+ oxidation state[5]. Interestingly, we identified a binding energy shift in the crystalline Y_2C spectrum of 155.7 eV, corresponding to a shared oxidation state both before and after fluorination. These findings corroborate the hypothesis that fluoride anions and electride electrons exert similar electrostatic forces on the host lattice[5]. During electrochemical fluorination, the electride electron and fluoride anion effectively exchange for one another, resulting in no reduction or oxidation of either the cationic framework or the intercalant itself. The peaks at higher binding energies, i.e., at 157.6 eV and 159.6 eV, both correspond to surface oxides, which is consistent with reported Y_2O_3 standards[24].

The carbon signals of Y_2C and Y_2CF_2 present similar electronic structures at the surface of the material. At the highest energy, adventitious carbon peaks attributed to carbon–oxygen bonding can be observed. The main peak at 284.6 eV can be attributed to adventitious carbon. All the spectra were energy-

corrected according to this adventitious carbon peak. The peak at 279.6 eV for the crystalline phase of Y_2CF_2[4] is reported to belong to a reduced carbide species in the Y_2CF_2 structure. This species has the lowest recorded bonding energy for carbide bonds. However, we observe an extremely low energy peak of 279.3 eV for Y_2C, which is even lower than that of Y_2CF_2. In the case of the amorphous phase of Y_2CF_2, we also note the occurrence of the reduced carbide; however, with a 1s electron binding energy of 279.7 eV, it aligns well with crystalline Y_2CF_2. Surprisingly, we find that there is a peak on the low-energy shoulder of the adventitious carbon peak. This peak has been attributed to an oxidized carbide species in previous reports[25]. However, the surface oxygen concentration (Figure A7-3) is the same across all species. Thus, we suggest that the peak arises from a carbide–fluorine bond that forms due to the migration of fluoride into the cationic layer of Y_2CF_2 during the amorphization process. This finding is supported by our simulations (Figure 7-4).

7.3.5 Analysis of the Expanded/Amorphous Y_2C

In the future, by computationally defluorinating the amorphous Y_2CF_2 material, we can qualitatively analyze the expanded Y_2C glass. The electron localization function of the material may reveal a complex topology and multidimensional electron connectivity. In this sense, the expanded Y_2C could transport ions in 3 dimensions, potentially leading to fluoride diffusion pathways with varied activation barriers. Furthermore, the high dimensional topology could lead to sites with relatively high energies for fluoride storage. The material would thus have a higher concentration of fluoride vacancies (inversely - solvated electron density), leading to enhanced vacancy enabled diffusivity. Altogether, this structural deformation, designed by the joint efforts at UNC and UniST, could lead to an electrode with enhanced cycling performance.

Given these results, we hypothesize three reasons for the material enhanced performance: 1) long ball milling in the presence of electrically conductive additives provides the necessary percolation network to efficiently transport electrons and ions, and 2) the amorphous structure facilitates ion transport, decreasing overpotentials associated with solid-state diffusion, and 3) the solvated electron network supports the amorphous structure of the defluorinated material, increasing the overall cycle stability of the material system.

7.4 Conclusions

In this study, we successfully developed an amorphous yttrium subcarbide fluoride material that overcomes the typical limitations of fluoride-ion battery electrodes by creating a stable and efficient pathway for fluoride ion transport. By leveraging the unique structural stability provided by solvated electrons within the amorphous network, this material demonstrated high cycling capacity and reduced degradation over repeated charge–discharge cycles. The amorphous phase, induced by ball milling and electrochemical processing, not only maximizes ion diffusion pathways but also minimizes side reactions typically associated with crystalline materials. Our results indicate that aY_2CF_2 represents a promising advance in fluoride-ion battery design, contributing to a more sustainable energy landscape with high-performance, long-life batteries. Further research into optimization and scalability may enable broader application and commercial viability of this technology in the future.

REFERENCES

1. Nowroozi, M. A. *et al.* Fluoride ion batteries - past, present, and future. *Journal of Materials Chemistry A* vol. 9 5980–6012 Preprint at https://doi.org/10.1039/d0ta11656d (2021).

2. Tojigamori, T. *et al.* Fluorination/Defluorination Behavior of Y2C in Fluoride-Ion Battery Anodes. *ACS Appl Energy Mater* **7**, 1100–1108 (2024).

3. Warren, S. *et al.* Metal Carbides and Metal Nitrides For Fluoride Ion Battery. (2023).

4. Zhang, X. *et al.* Two-dimensional transition-metal electride Y2C. *Chemistry of Materials* **26**, 6638–6643 (2014).

5. Druffel, D. L. *et al.* Synthesis and Electronic Structure of a 3D Crystalline Stack of MXene-Like Sheets. *Chemistry of Materials* **31**, 9788–9796 (2019).

6. Druffel, D. L. *et al.* First-Principles Prediction of Electrochemical Electron-Anion Exchange: Ion Insertion without Redox. *Journal of Physical Chemistry Letters* **11**, 9210–9214 (2020).

7. Edwards, P. P. Electrons in cement. *Science* vol. 333 49–50 Preprint at https://doi.org/10.1126/science.1207837 (2011).

8. Feng, D.-F. & Kevan, L. *Theoretical Models for Solvated Electrons*. *Chemical Reviews* vol. 80 https://pubs.acs.org/sharingguidelines (1980).

9. Society, A. C., Charles, B. & Kraus, A. *General Properties of Solutions of Metals in Liquid Ammonia*. *see This Journal* vol. 29 https://pubs.acs.org/sharingguidelines (1908).

10. Hosono, H. & Kitano, M. Advances in Materials and Applications of Inorganic Electrides. *Chemical Reviews* vol. 121 3121–3185 Preprint at https://doi.org/10.1021/acs.chemrev.0c01071 (2021).

11. Düvel, A., Ruprecht, B., Heitjans, P. & Wilkening, M. Mixed Alkaline-Earth Effect in the Metastable Anion Conductor Ba1–xCaxF2 (0 ≤ x ≤ 1): Correlating Long-Range Ion Transport with Local Structures Revealed by Ultrafast 19F MAS NMR. *Journal of Physical Chemistry C* **115**, 23784–23789 (2011).

12. Opletal, G. *et al.* Hybrid approach for generating realistic amorphous carbon structure using metropolis and reverse Monte Carlo. *Mol Simul* **28**, 927–938 (2002).

13. Thompson, A. P. *et al.* LAMMPS - a flexible simulation tool for particle-based materials modeling at the atomic, meso, and continuum scales. *Comput Phys Commun* **271**, (2022).

14. Vandermause, J. *et al.* On-the-fly active learning of interpretable Bayesian force fields for atomistic rare events. *NPJ Comput Mater* **6**, (2020).

15. Kresse, G. & Hafner, J. *Ab. Initio Molecular Dynamics for Liquid Metals*. vol. 47.

16. Kresse, G. & Furthmüller, J. Efficiency of ab-initio total energy calculations for metals and semiconductors using a plane-wave basis set. *Comput Mater Sci* **6**, 15–50 (1996).

17. Kresse, G. & Furthmü, J. *Efficient Iterative Schemes for Ab Initio Total-Energy Calculations Using a Plane-Wave Basis Set*. (1996).

18. Ong, S. P. *et al.* Python Materials Genomics (pymatgen): A robust, open-source python library for materials analysis. *Comput Mater Sci* **68**, 314–319 (2013).

19. Machon, D. & Mélinon, P. Size-dependent pressure-induced amorphization: A thermodynamic panorama. *Physical Chemistry Chemical Physics* **17**, 903–910 (2015).

20. Johnson, W. C., Lee, J. K. & Shiflet, G. J. Thermodynamic treatment of cyclic amorphization during ball milling. *Acta Mater* **54**, 5123–5133 (2006).

21. Edison, E. *et al.* Electrochemically Induced Amorphization and Unique Lithium and Sodium Storage Pathways in FeSbO4 Nanocrystals. *ACS Appl Mater Interfaces* **11**, 20082–20090 (2019).

22. Guo, T., Hu, P., Li, L., Wang, Z. & Guo, L. Amorphous materials emerging as prospective electrodes for electrochemical energy storage and conversion. *Chem* vol. 9 1080–1093 Preprint at https://doi.org/10.1016/j.chempr.2023.03.032 (2023).

23. Xiong, F., Tao, H. & Yue, Y. Role of Amorphous Phases in Enhancing Performances of Electrode Materials for Alkali Ion Batteries. *Frontiers in Materials* vol. 6 Preprint at https://doi.org/10.3389/fmats.2019.00328 (2020).

24. Moulder, J. F., Stickle, W. F., Sobol, P. E. & Bomben, K. D. Handbook of X-ray photoelectron spectroscopy. 1992. *Eden Prairie, MN* (1992).

25. Kocks, U. F., Argon, A. S. & Ashby, M. F. *Thermodynamics and Kinetics of Slip*. vol. 19 (Pergamon Press Ltd., 1975).

APPENDIX: SUPPORTING INFORMATION FOR CHAPTER 4.

The high throughput discovery of stable dopants resulted in both Ca and Sr as potential aliovalent dopants. Thus, I set out to synthesize both materials. While Ca doping resulted in little variation in the structure, the doping of Sr into Y_2CF_2 resulted in significant formation of competing phases. Although there were no identifiable phases from the ICSD or materials project, the refined peaks corresponded to reflections identifiable with Parisite. Parisite is a carbonite mineral with a composition of $Ca(Ce, La)_2(CO_3)_3F_2$. Given the chemical similarity of Sr to Ca, and Y to other rare-earth metals, oxygen exposure and annealing could form the Cc space-group structure. As Sr content increased, the formation of parasite increased while the Y_2CF_2 $P\bar{3}m1$ structure decreased.

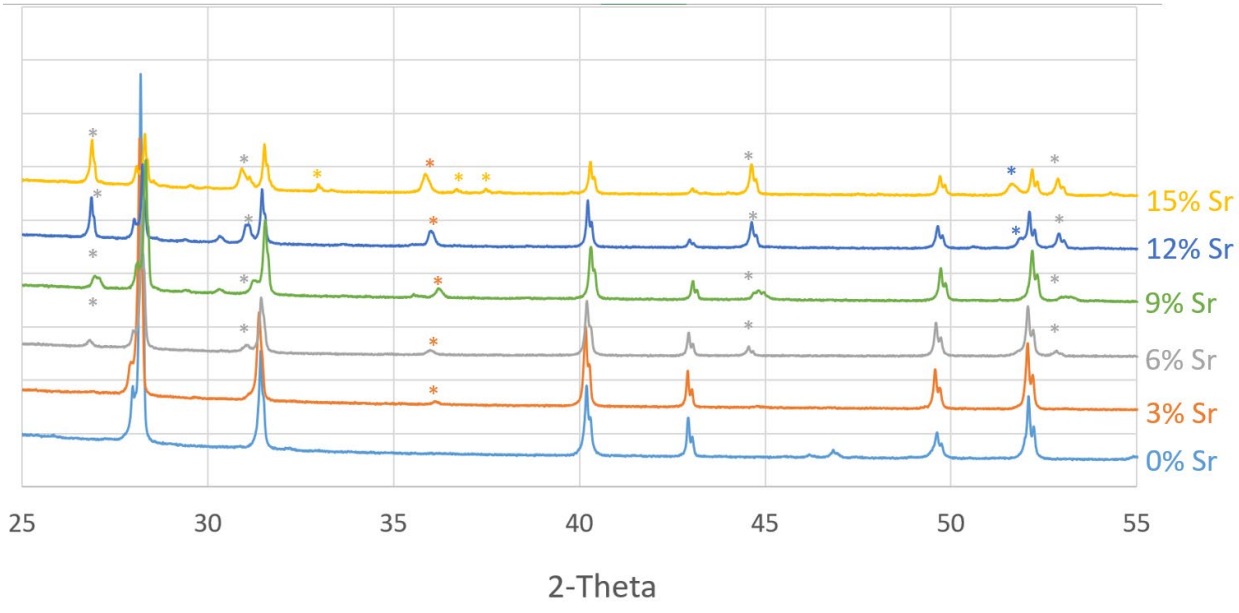


Figure A4 - 1: Decomposition of Sr-doped Y_2CF_2 into parisite as Sr composition increased. Asterisks reveal the decomposition product.

APPENDIX: SUPPORTING INFORMATION FOR CHAPTER 5

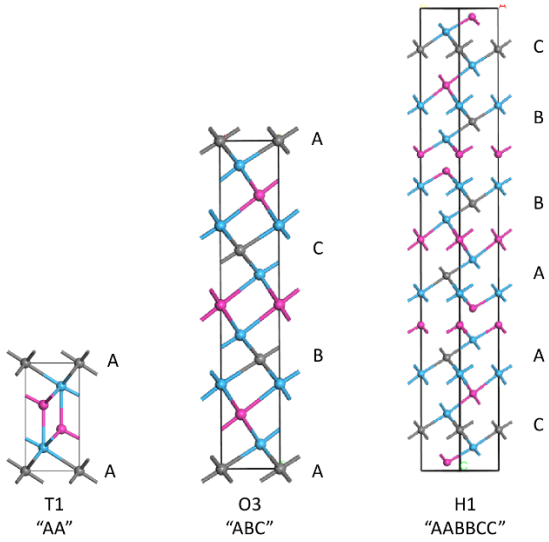


Figure A5 - 1: Crystal structures of the T1, O3, and H1-3 phases considered in our cluster expansion.

All 3 stacking sequences are shown in Figure A3-2. The H1-3 phase is a hypothetical structure of hybridized stacking sequences of the T1 and O3 phases that has an overall stacking sequence of AABBCC. We used an a lattice constant of 3.53 Å and c lattice constant of 17.12 Å, though the parameters and atomic positions of all cells used in the cluster expansion were fully optimized before calculating the energy.

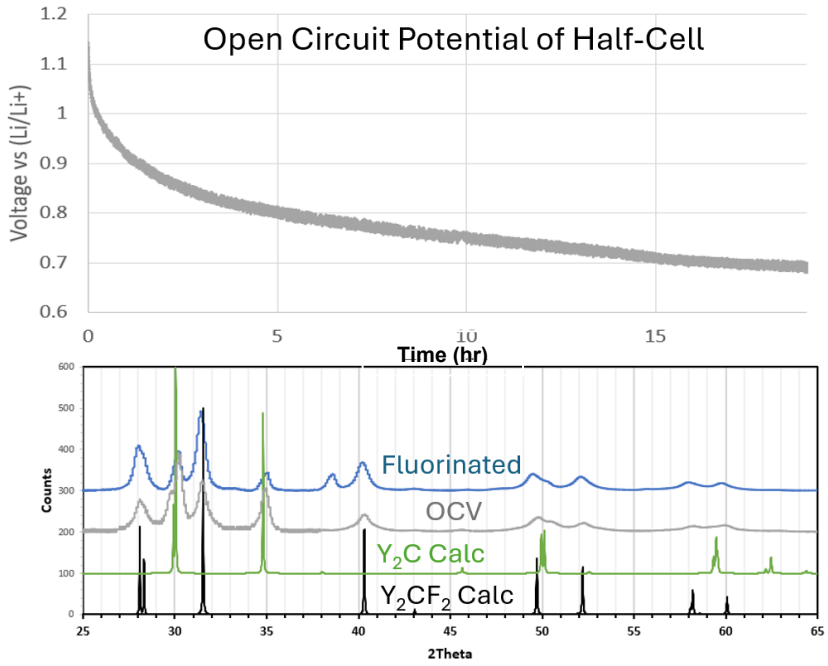


Figure A5 - 2: (Top) Open circuit potential of Y_2C composite electrodes submerged in Np1F/BTFE electroltye. (Bottom) Corresponding XRD of structure decomposition observed after contact with Np1F/BTFE.

Figure A5-2 shows the change in potential of a Y_2C composite anode exposed to Np1F/BTFE without any applied bias. The potential quickly sweeps down as the electrode and electrolyte react with each other, passing current via redox reactions at the surface. During exposure, Np1F is reduced by Y_2C, liberating a fluoride that then intercalates into Y_2CF_2 due to the electric field caused by the redox. This reaction continues over the course of 15 hours. The degradation reaction results in a 48% conversion to Y_2CF_2 as calculated by Rietveld Refinement.

APPENDIX: SUPPORTING INFORMATION FOR CHAPTER 6

A6.1 TMA Coating vs Sulfur Coating Solution based deposition

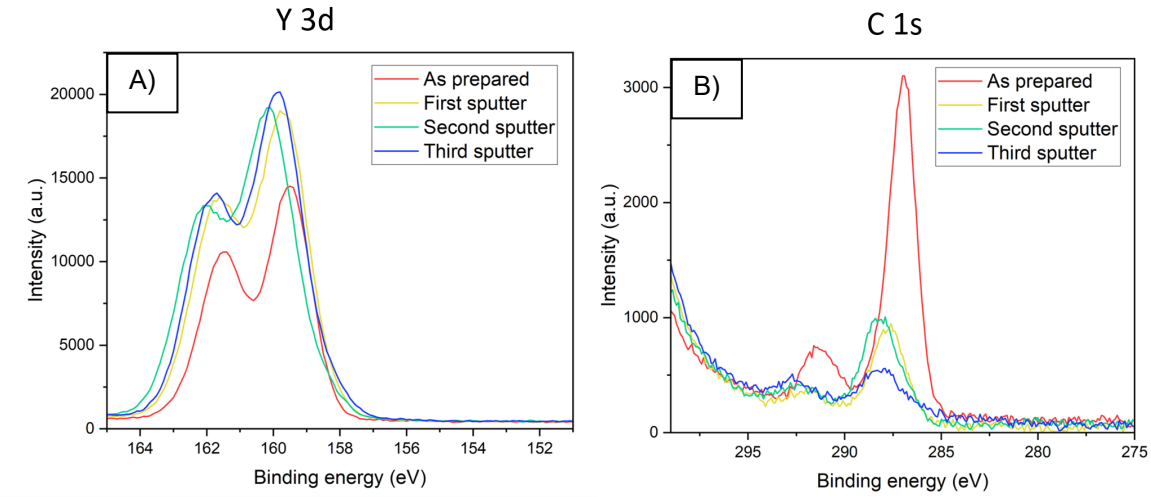


Figure A6 - 1: XPS of Y_2C cleaved in a TMA:Toluene solution. A) Y 3d signal revealing Y^{3+} oxidation states (159eV) after Ar+ sputtering experiments and B) C 1s signal revealing adventicious carbon states (~285eV) after Ar+ sputtering experiments

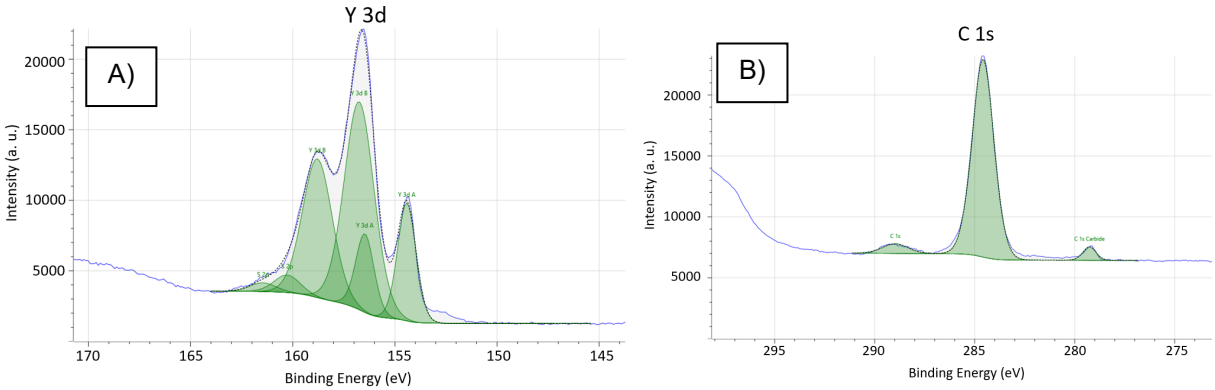


Figure A6 - 2: XPS of Y_2C cleaved in a Sulfur:Toluene solution. A) Y 3d signal revealing Y^{3+} (157.0 eV) and Y^{2+} oxidation states (154.6 eV) on the as-made cleaved surface and B) C 1s signal revealing adventicious carbon (284.6 eV) and carbide (279.6 eV) states after Ar+ sputtering experiments

A6.2 Cubic vs Layered Sulfur Coating Dynamics

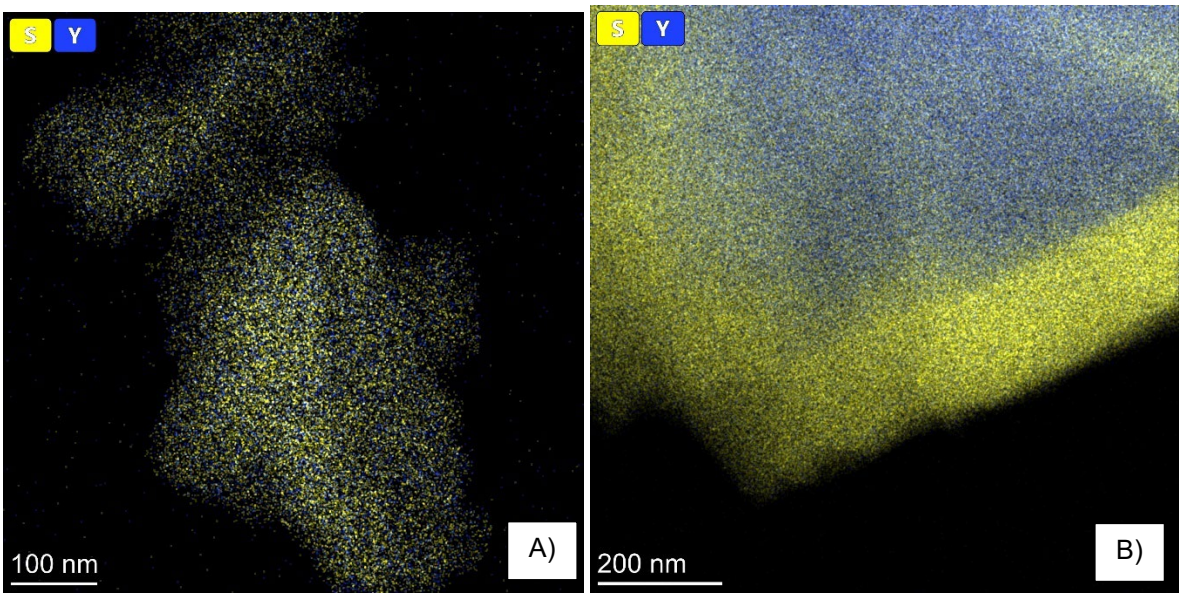


Figure A6 - 3: A) TEM-EDS mapping of a sulfur coated cubic-Y_2C particle synthesized at 350 °C for 6 hours, revealing no formation of core-shell morphology compared to B) TEM-EDS mapping of sulfur coated layered-Y_2C particle synthesized at 350 °C for 6 hours, revealing formation of core-shell morphology.

A6.3 Exposure to Oxygen for 1 week

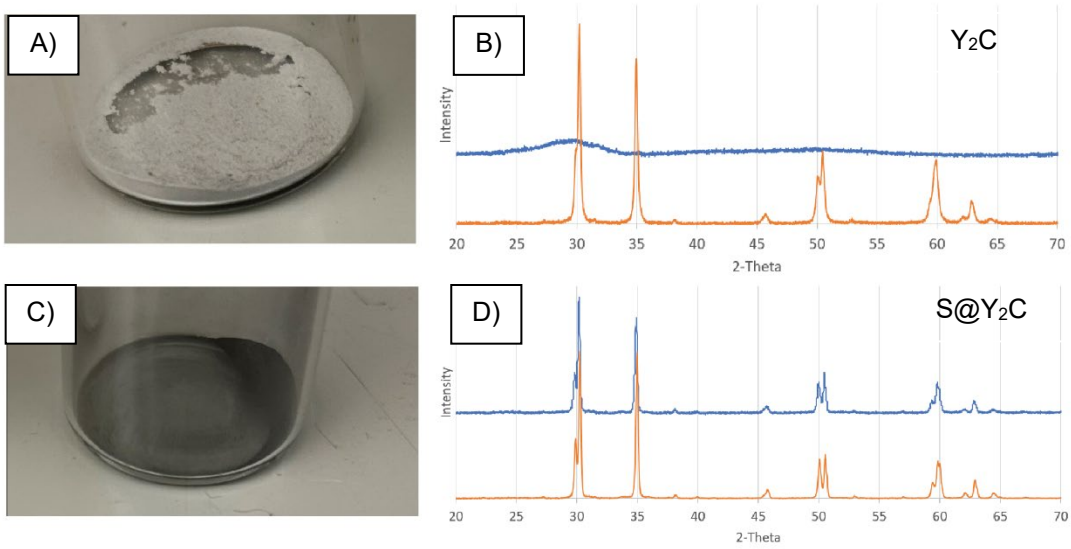


Figure A6 - 4: A) Y_2C powder exposed to air for 6 days and B) corresponding XRD revealing amorphization. C) S@Y_2C powder exposed to air for 6 days and D) corresponding XRD revealing no degradation of the electride crystal.

APPENDIX: SUPPORTING INFORMATION FOR CHAPTER 7

A7.1 Electrochemical and Physical Characterization

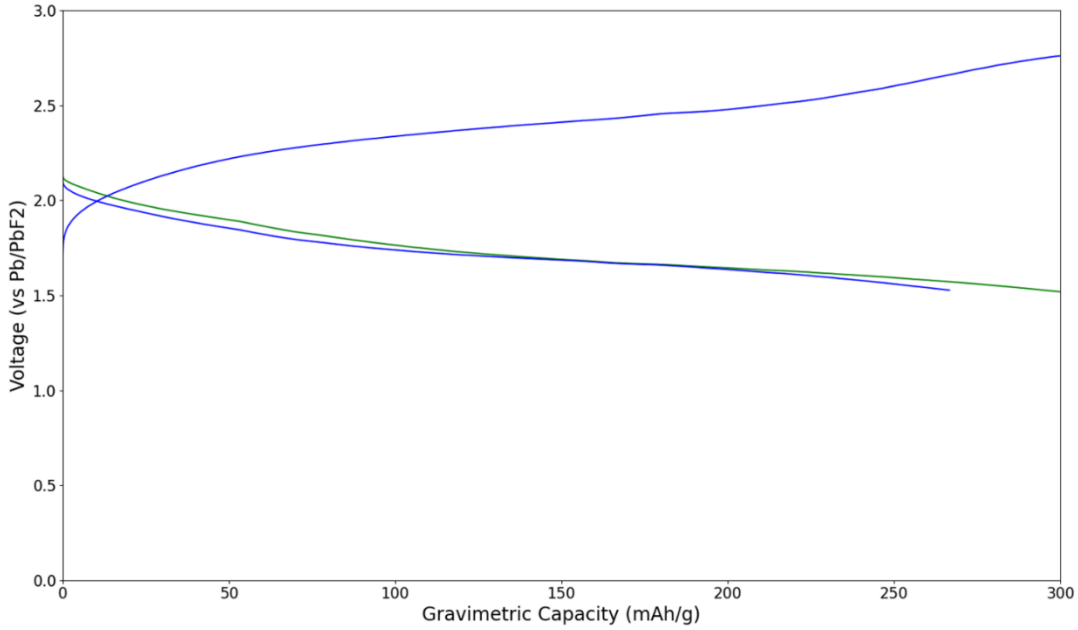


Figure A7 - 1: First discharge (green) and discharge/charge (blue) cycle of Y_2C/Cu/CBF composite.

A7.2 Atom Quantification with TEM-EDS

Table A7 - 1: Average Values across amorphous Y_2CF_2 particles obtained via TEM-EDS

Element	Family	Atomic Fraction (%)	Atomic Error (%)	Mass Fraction (%)	Mass Error (%)	Fit error (%)
C	K	6.0	1.2	1.5	0.2	5.6
O	K	6.3	1.7	2.1	0.5	3.6
F	K	45.7	12.5	18.5	4.2	0.7
Y	K	41.9	9.5	77.9	13.0	0.5

A7.3 XPS Standards

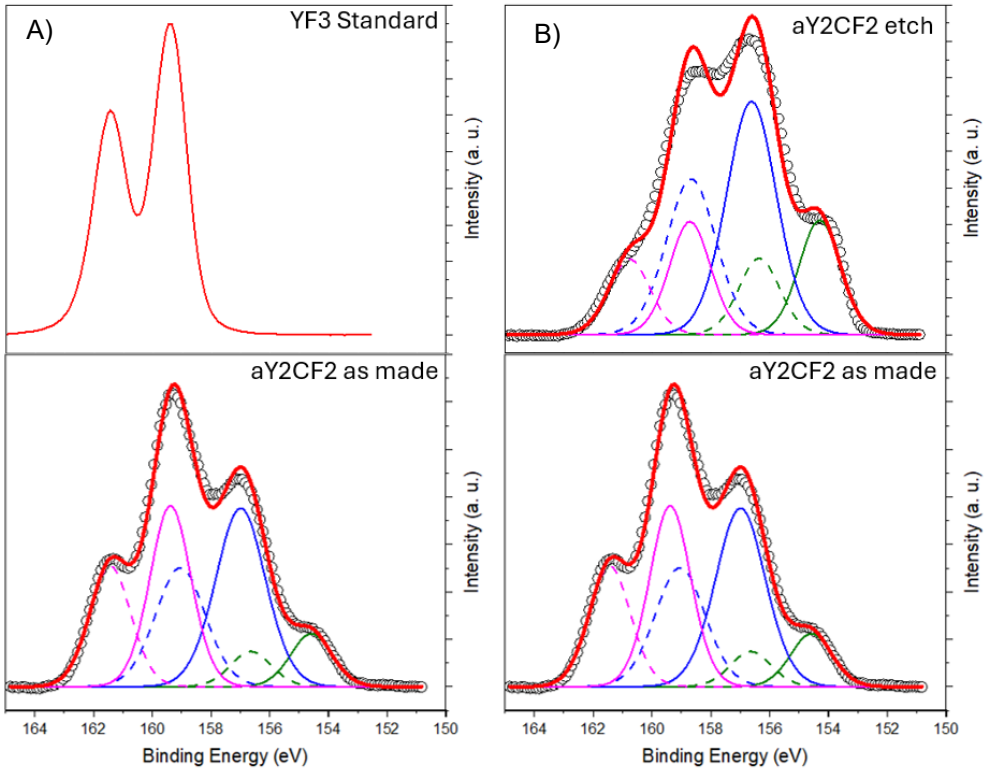


Figure A7 - 2: YF_3 measured with XPS reveals formation of YF_3 across each amorphous Y_2CF_2 sample on its surface. A) YF_3 standard directly compared to aY_2CF_2 as made sample. B) aY_2CF_2 etched with Ar+ directly compared to aY_2CF_2 reveals significant change in intensity of YF_3, revealing the impurity is confined to the sample's surface.

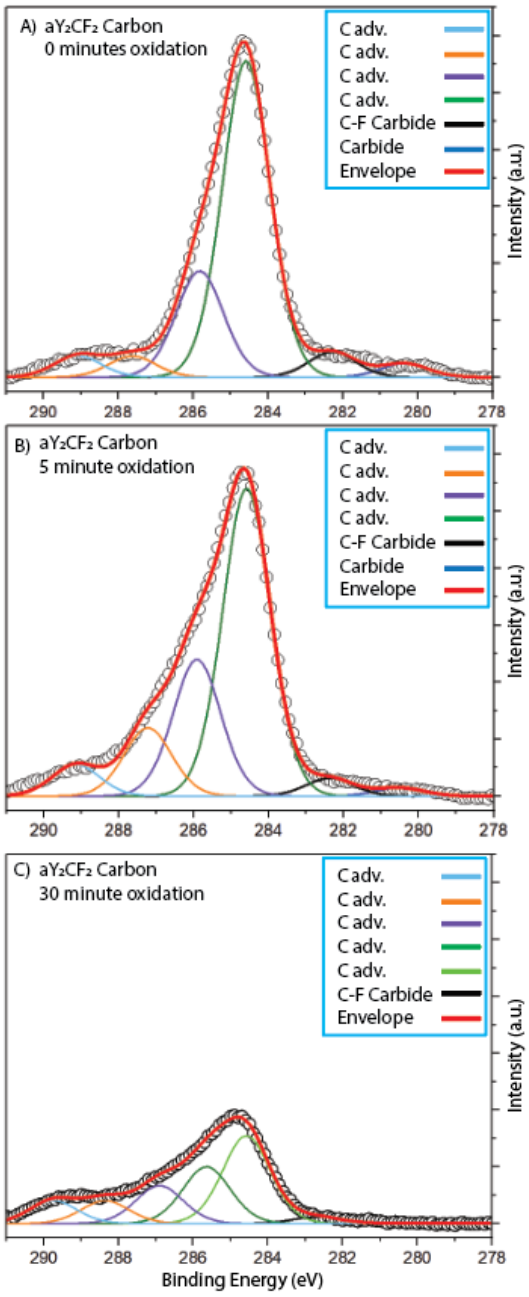


Figure A7 - 3: Amorphous Y_2CF_2 exposed to oxygen. As the peak, assigned to an oxidized carbide species at 282 eV, does not increase in intensity, the peak can be assigned to a C-F bond rather than a C-O bond.

A7.4 Amorphization Mechanism

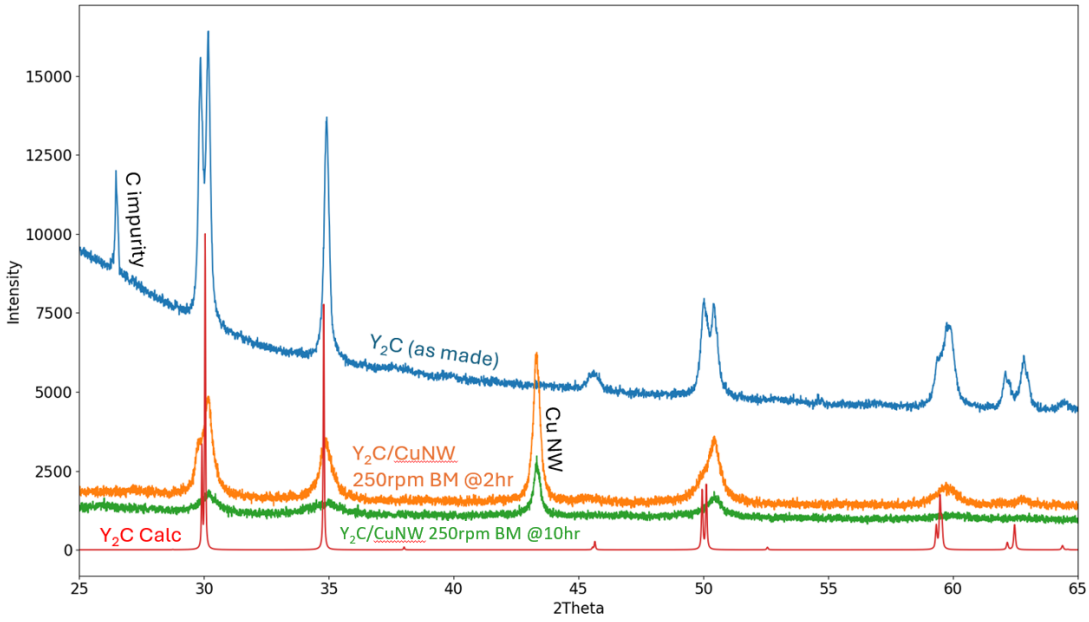


Figure A7 - 4: XRDs of Y_2C composite as ball mill time increase. As time increases, peak intensity decrease and broaden as particle size decreases.

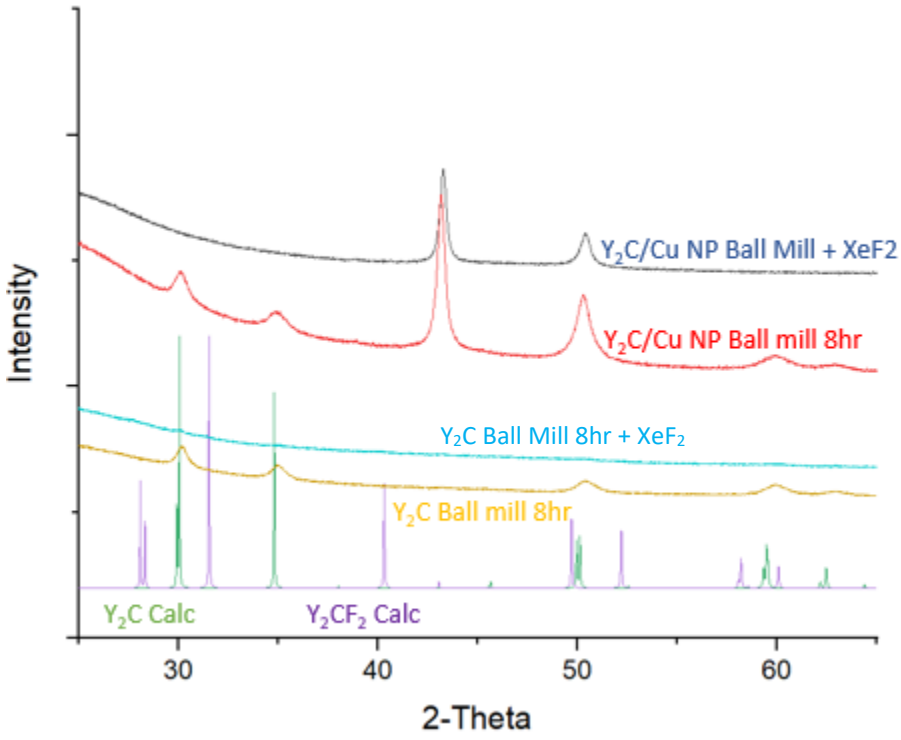


Figure A7 - 5: XRDs of Y_2C electrode composite chemically fluorinated with XeF_2 with Cu nanoparticle electron conducting additive (red) and without Cu nanoparticles (yellow).

A7.1.1Thermodynamic Model of Amorphous Transition

Previous studies into the thermodynamics of amorphization provide insight into physiochemical driving forces of metastable phase transitions. According to Machon and Melinon[19], crystalline-to-amorphous (CtA) phase transitions are dependent on the energy of the crystalline phase and the height of the energy barrier between the crystalline phase and the amorphous phase(s). Under ball milling conditions, two processes occur leading to increased energy of the crystalline system: 1) as particle size decreases, the surface energy increases, and 2) ball milling introduces strain and dislocations into the lattice, increasing the defect concentration within the crystal. When defects are introduced into the crystalline system at a high enough concentration, the energy of crystalline-to-crystalline phase transitions, requiring bond breaking and stacking reorganization, can be higher than that of the CtA transition.

Machon and Melinon describe these amorphizations in reference to isothermal compression:

$$\partial G = V\,\partial \mathrm{P} + \gamma \mathrm{dA}$$

Where the change in free energy, ∂G, is dependent on the change in pressure, ∂P and surface area in bulk and nano conditions, γdA. Given a system undergoing topochemical insertion with no compression, we can adapt the equation as:

$$\partial G = \mu_{ion}\, \partial n_{ion} + C_{44} b^2 \delta d$$

Where $\partial G$is the Gibbs Free Energy, $\mu_{ion}\, \partial n_{ion}$ is the chemical potential multiplied by the ratio of inserted ions to the total available sites within the crystal lattice, C_{44} is shear modulus, and b^2 is the Burgers Vector. The defect energy[25], thus, is a function of the dislocation concentration.

This qualitative description allows us to define a model for the amorphous phase transition in Y_2CF_2 electrodes. As defect concentration increases, the molar free energy of the particle is large enough to preferentially form the metastable amorphous phase. This process is instantiated by the intercalation of ions, providing the driving force for a transition.

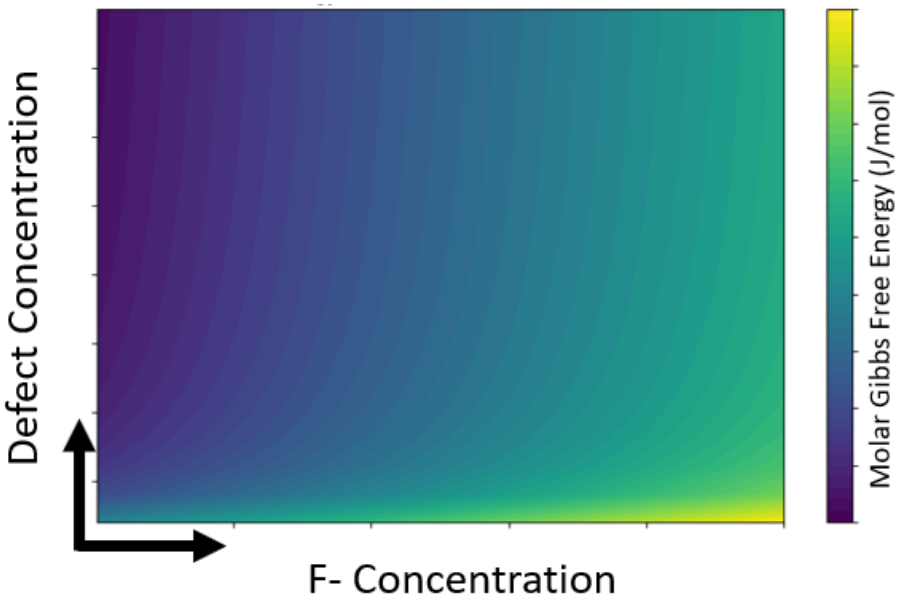


Figure A7 - 6: Qualitative model of the effect of ion insertion on structural energy. This model shows that as ions insert into Y_2C particles with small radii, high defect concentrations could drive the phase transition into an amorphous structure.

These results provide insight into the mechanism for improved performance. When first discharged, the ball milled yttrium subcarbide expands to such a degree that all the crystallinity is lost. This expansion

facilitates ion diffusion into the electrode, leading to high capacities and low overpotentials. Upon recharge, a novel phase with an approximate stoichiometry of Y_2C (yttrium subcarbide) forms with substantially larger lattice parameters than the as-made $R\bar{3}m$ Y_2C phase.

A7.5 Coordination Environment of structure optimized aY_2CF_2

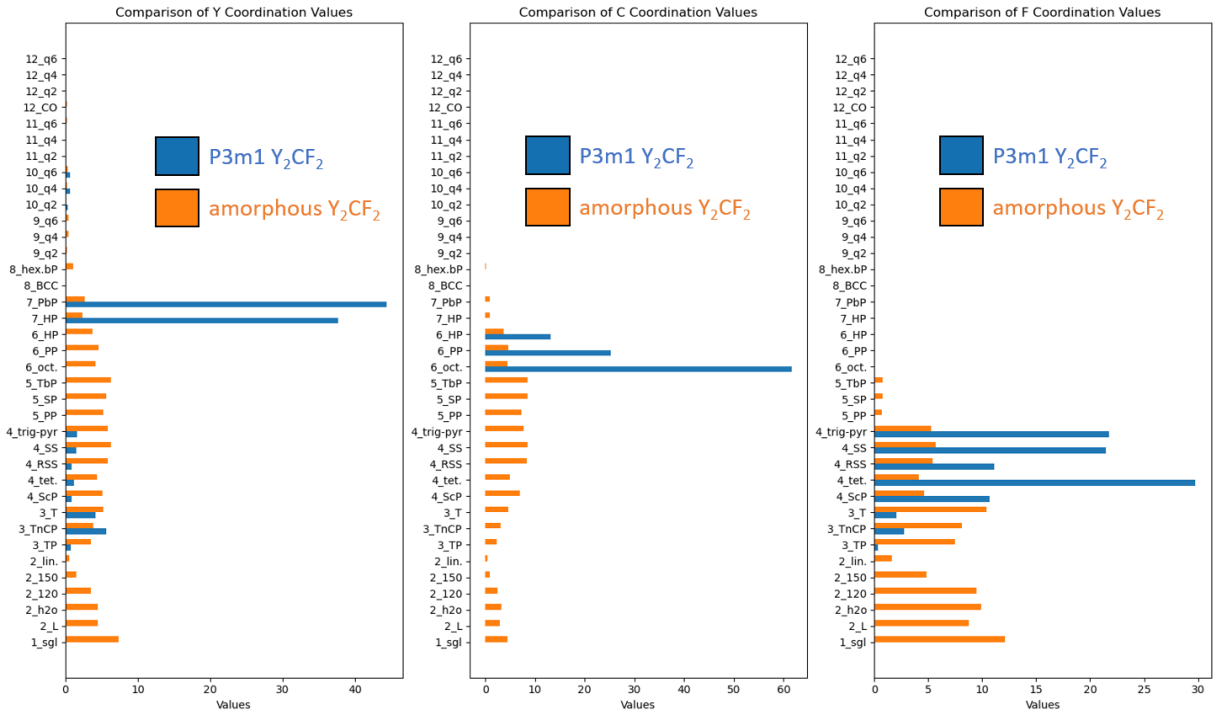


Figure A7 - 7: Coordination analysis of crystalline (blue) vs amorphous (orange) Y_2CF_2 structure, fabricated using hybrid reverse Monte Carlo simulations. Significant deviation from the crystalline bonding environment indicate a structural reorganization in experimental synthesized amorphous material.